(12) INTERNATIONAL APPLICATION PUBLISHED UNDER THE PATENT COOPERATION TREATY (PCT)

(19) World Intellectual Property Organization
International Bureau

(43) International Publication Date
21 March 2024 (21.03.2024)

WIPO | PCT

(10) International Publication Number
WO 2024/057299 A1

(51) International Patent Classification:
G01Q 60/16 (2010.01) *G01Q 70/10* (2010.01)
G01Q 60/40 (2010.01) *G01Q 70/14* (2010.01)

(21) International Application Number:
PCT/IL2023/050201

(22) International Filing Date:
27 February 2023 (27.02.2023)

(25) Filing Language: English

(26) Publication Language: English

(30) Priority Data:
63/375,916 16 September 2022 (16.09.2022) US

(71) Applicant: **YEDA RESEARCH AND DEVELOPMENT CO. LTD.** [IL/IL]; At the Weizmann Institute of Science, P.O.Box 95, 7610002 Rehovot (IL).

(72) Inventors: **ILANI, Shahal**; Berman 8 St., 7621314 Rehovot (IL). **INBAR, Alon**; c/o Yeda Research and Development Co. Ltd., at the Weizmann Institute of Science, P.O. Box 95, 7610002 Rehovot (IL). **BIRKBECK, John**; c/o Yeda Research and Development Co. Ltd., at the Weizmann Institute of Science, P.O. Box 95, 7610002 Rehovot (IL). **XIAO, Jiewen**; c/o Yeda Research and Development Co. Ltd., at the Weizmann Institute of Science, P.O. Box 95, 7610002 Rehovot (IL).

(74) Agent: **STADLER, Svetlana**; c/o Cohn De Vries Stadler & Co., P.O.B 10278, 6110103 Tel Aviv (IL).

(81) Designated States *(unless otherwise indicated, for every kind of national protection available)*: AE, AG, AL, AM, AO, AT, AU, AZ, BA, BB, BG, BH, BN, BR, BW, BY, BZ, CA, CH, CL, CN, CO, CR, CU, CV, CZ, DE, DJ, DK, DM, DO, DZ, EC, EE, EG, ES, FI, GB, GD, GE, GH, GM, GT, HN, HR, HU, ID, IL, IN, IQ, IR, IS, IT, JM, JO, JP, KE, KG, KH, KN, KP, KR, KW, KZ, LA, LC, LK, LR, LS, LU, LY, MA, MD, MG, MK, MN, MW, MX, MY, MZ, NA, NG, NI, NO, NZ, OM, PA, PE, PG, PH, PL, PT, QA, RO, RS, RU, RW, SA, SC, SD, SE, SG, SK, SL, ST, SV, SY, TH, TJ, TM, TN, TR, TT, TZ, UA, UG, US, UZ, VC, VN, WS, ZA, ZM, ZW.

(84) Designated States *(unless otherwise indicated, for every kind of regional protection available)*: ARIPO (BW, CV, GH, GM, KE, LR, LS, MW, MZ, NA, RW, SC, SD, SL, ST,

(54) Title: PROBES, APPARATUSES AND METHODS FOR USE IN SCANNING PROBE MICROSCOPY

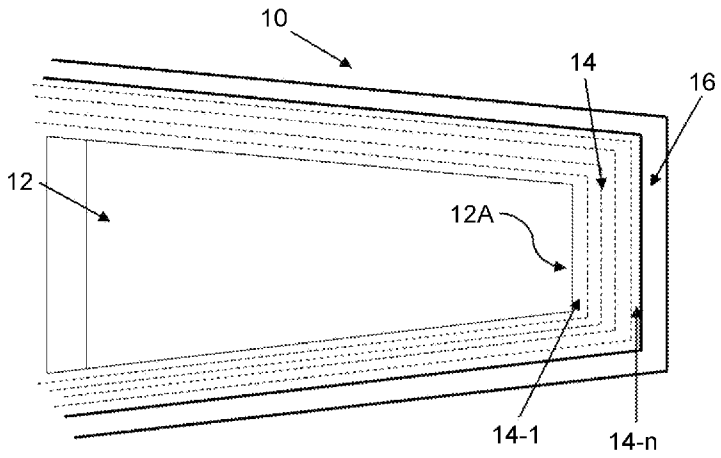

FIG. 1A

(57) Abstract: A probe is presented for mechanically contacting a sample and for use in conducting electrical measurements on the sample. The probe comprises a tip having a core with an apex is covered by a layer arrangement comprising at least a support layer of a vdW material and an active layer presenting a 2D material of not more than 10 monolayers coupled by vdW forces. The active layer is placed on the support layer at said apex and is thereby further away from the core than the support layer at said apex. An outer layer of the layer arrangement is an exposed layer. The layer arrangement is configured to form, under a pressure against a planar surface, a mechanical contact of a contact area comprising a square with a side of 10 nm or more, and is configured to conduct an electric current substantially in a lateral dimension and through the active layer.

WO 2024/057299 A1

[Continued on next page]

SZ, TZ, UG, ZM, ZW), Eurasian (AM, AZ, BY, KG, KZ, RU, TJ, TM), European (AL, AT, BE, BG, CH, CY, CZ, DE, DK, EE, ES, FI, FR, GB, GR, HR, HU, IE, IS, IT, LT, LU, LV, MC, ME, MK, MT, NL, NO, PL, PT, RO, RS, SE, SI, SK, SM, TR), OAPI (BF, BJ, CF, CG, CI, CM, GA, GN, GQ, GW, KM, ML, MR, NE, SN, TD, TG).

Declarations under Rule 4.17:

— *of inventorship (Rule 4.17(iv))*

Published:

— *with international search report (Art. 21(3))*

PROBES, APPARATUSES AND METHODS FOR USE IN SCANNING PROBE MICROSCOPY

TECHNOLOGICAL FIELD

This disclosure relates to the field of scanning probe microscopy (SPM).

BACKGROUND

Scanning probe microscopy (SPM) is a branch of microscopy that forms images of the mechanical and electronic properties of surfaces using a physical probe that scans across the sample. It includes such types as atomic force microscopy (AFM), scanning tunneling microscopy (STM), and others. AFM includes such a sub-type as conductive AFM (CAFM, C-AFM) or current sensing AFM (CS-AFM). Other names for such techniques, or related techniques, are local-conductivity AFM (LC-AFM), conductive probe AFM (CP-AFM), conductive scanning probe microscopy (C-SPM) or conductive scanning force microscopy (C-SFM).

According to Ref. 2, CAFM uses a sharp conductive probe to map local variations in a sample's conductivity with nanoscale resolution. It is used to study a sample's conductivity and image electrical properties such as charge transport and charge distribution on the nanoscale. CAFM is applied in the nanoelectronics field, solar cell and semiconductor industries for a wide variety of high resolution measurements including semiconductor dopant profiling and quality control for dielectric films and oxide layers.

The conducting probe in CAFM typically has a thin conducting coating. Common electrically conducting coatings are platinum, gold, tungsten, and conductive diamond.

CAFM is usually operated in contact mode: a bias voltage is applied between AFM tip and sample when they are in contact, and the current flow is measured between them as the probe raster scans across the surface. The contact area between tip and sample typically has a diameter in the 10 nm range.

At the same time, the topography of the surface is measured by detecting the deflection of the cantilever where the tip resides using an optical system (for example, a laser combined with a photodiode) or using a piezoresistive technique. Additionally, localized single-point measurements of current-voltage (I-V) curves can be collected with CAFM without moving the probe over the sample: when the probe is placed upon the desired point on the sample, a bias voltage may be, for example, tuned to increase in steps; and current may be measured at each step.

GENERAL DESCRIPTION

In CAFM, the scanning contact mode of operation can lead to an aggressive tip-sample interaction that can wear down the tip quickly. At the same time, surface contamination and a water film between tip and sample, commonly present at ambient conditions, can reduce the reliability and repeatability of CAFM. Only a few nanometers of debris on the tip can block the flow of electrical current. Consequently, as mentioned in Ref. 2, higher forces are often needed, requiring harder tip materials or coatings like conductive diamond-like coatings or platinum silicide since these higher forces will degrade the tip faster.

In such circumstances, the inventors have addressed a general need for sensitive SPM techniques for the characterization of the electronic structure of the sample.

The inventors have found techniques which can be used in contact mode to obtain the current measurements. The technique of the present disclosure is not limited to be implemented in CAFM; but rather can be used in systems which differ from CAFM in the structures of the probe; and/or in the type of the measured current or specifics of the characterization which it brings about; and/or in samples at which these techniques are primarily aimed; and/or in the setup and method realizing the scanning in the contact mode. The inventors have termed the relevant techniques/systems as Quantum Twisting Microscopy.

The probes suitable for use in the scanning techniques of the present disclosure are characterized by such features as a tip having a core with an apex, where this apex is covered by an active layer presenting a two-dimensional (2D) material of not more than 10 monolayers coupled by van der Waals (vdW) forces, and the active layer is placed on a support layer of a vdW material: the active layer at that apex is thereby further away

from the core than the support layer at that apex (and the active and support layers form a vdW heterostructure at the apex).

Also, the probes utilized in the technique of the present disclosure share the feature of a layer arrangement, covering the apex and the core of the tip and including at the apex at least the support layer and the active layer, which is configured to form, under a pressure against a planar surface, a contact area containing a square with a side of 10 nm or more. The contact area may take various geometrical shapes, but it contains a square with a side of 10 nm or more. The flat or flattened contact area may be larger or smaller than the apex area.

An outer layer of the layer arrangement (by which it faces the sample) is an exposed layer.

Furthermore, the probes utilized in the technique of the present disclosure share the feature that the layer arrangement is configured to conduct an electric current to the active layer from outside (i.e. from an exposed layer if this is not the active layer, but a more externally placed layer) and then, at the apex, in a lateral dimension (substantially or even only) and through the active layer (substantially or only).

In a first group of examples of the probe of the present disclosure (embodiments of the probe), the active layer at the apex is the exposed layer.

In a second group of examples, the tip at the apex is further covered by a tunnel barrier layer placed on the active layer; and it is the tunnel barrier layer which is the exposed layer. This tunnel barrier layer is thereby configured to present a flow path for a tunneling current between the sample and the 2D material of the active layer. The layer arrangement, which at the apex additionally includes the tunnel barrier layer, conducts the electric current by the tunneling through this layer (and then in a lateral dimension and through the active layer).

In a third group of examples, the tip at the apex is covered instead by a defect-assisted tunneling layer on the active layer (i.e., instead of the tunnel barrier layer). The defect-assisted tunneling layer is the exposed layer and includes at least one atomic defect which presents a tunneling path for tunneling between the sample and the active layer. Each such atomic defect may provide a peak of tunneling conductance at a certain unique voltage between (a) a region proximate to the defect on the active layer and (b) a region proximate to the defect and located beyond the exposed defect-assisted tunneling layer.

The sample is to be placed into the latter region. Here, the term "unique voltage" is used meaning that voltages are expected to differ for different defects). The layer arrangement, which at the apex additionally includes the defect-assisted tunneling layer, conducts the electric current by at least the tunneling via the at least one atomic defect in this layer when the applied voltage allows it (and then in a lateral dimension and through the active layer).

In all the above groups, the core presents the bulk of the tip and it may be made of a conductive material, such as a metal or a semiconductor or an alloy (e.g., Tungsten, Platinum, Platinum-Iridium, doped silicon, etc.); or of a dielectric (e.g., silicon, quartz, sapphire, diamond, etc.). For practical purposes, hereinafter by the dielectric material, a material with the bandgap larger than 2 eV is meant; and by the semiconductor, a material with non-zero bandgap smaller than 2 eV is meant.

The core may have a length larger than 1 micron (μm); and/or smaller than 10 mm (lengths closer to this value may correspond to cores which are similar to STM tips). In some of the experiments conducted by the inventors, the length was in a range 1.2-1.6 μm.

In general, 2D materials are substances with a thickness of a few nanometers, which are characterized by a layered crystal structure with strong bonds – covalent or ionic – within each layer, and where layers are coupled together by relatively weak vdW forces. Currently, hundreds of 2D materials are known. Many are natural semiconductors, along with metals, semimetals, superconductors, and various kinds of insulators (band insulators, topological insulators, and Mott insulators).

In the active layer made of the 2D material the carriers, for example, electrons, are free to move in the 2D plane at the apex, but their motion is restricted in the third direction outside of the active layer (with the quantum mechanical tunneling being the mechanism limiting the restriction). The 2D material may have not more than any smaller number of monolayers instead of 10: for example, the upper limit for the number of monolayers may be 7, or 4, 3, 2, or 1). The monolayers may differ in chemical composition, and the 2D material forming the active layer may be itself formed from monolayers of different 2D materials when they couple by vdW forces.

Examples of the suitable 2D material for the active layer include the semimetal graphene, transition metal dichalcogenides (TMDs) semiconductors including but not

limited to WSe_2, WS_2, $MoSe_2$, MoS_2, $TaSe_2$, TaS_2, $NbSe_2$, WTe_2 and so forth, $RuCl_3$ or similar 2D magnetic layers, BiSCCO or similar layered high-superconducting-temperature materials.

The support layer carrying at the apex the active layer is made of a vdW material. The support layer allows for the active layer to have the proper functionality: the active layer has to be sufficiently thin to be 2D, but if it was placed directly on the apex of the tip's core of some conventional material, it would bend and strain and thus loose its desired mechanical and/or electrical properties, since the apex could be too rugged. Thus, the support layer is selected to mitigate or prevent the chance that the vdW material of the active layer would not form the appropriately conducting and mechanically suitable for use in the probe 2D vdW material.

The support layer does not have to be a 2D material. It will have more than 10 monolayers. It can be a dielectric, or a semiconductor, or even a conductor, such as semimetal or a metal if an interface between the active layer and the support layer has a very small probability for a carrier to get transmitted therethrough upon one impinging on the interface. The latter can happen, for example, in case of a mismatch between lattices of the active layer and the support layer, or different orientations if they are made of the same material, resulting for example in a contact resistance greatly suppressing the current. In any case, the contact resistance higher than 10 times Sharvin resistance between the active layer and the support layer is suitable (a skilled person would readily find this resistance; but in any case, the formula for the ballistic case, which can serve as a reference, for different contact interfaces was originally presented in Sharvin, Yu. V. "*A possible method for studying Fermi surfaces*". Sov. Phys. JETP 21, 655 (1965), which is incorporated herein by reference).

In some sense, such a layer arrangement allows the 2D vdW material forming the active layer to behave differently from the same material in its bulk form, and vice versa: due to the active layer being a 2D vdW material conducting the current laterally, the support layer substantially does not receive the current to conduct therethrough due to the nature of the interface between the active and support layers, or practically does not conduct it itself. For example, the layer arrangement may be configured in such a way that the current through the active layer can be three, or five, or ten, or fifty times higher a residual current, if any, through the support layer.

Examples of the suitable vdW materials for the support layer include, but are not limited to, insulating hexagonal boron nitride (hBN), conductors like graphite, semiconductors including but not limited to WSe_2, WS_2, $MoSe_2$, MoS_2 and 2D magnets such as RuCl3 and similar materials.

As for the feature that the layer arrangement forms under a pressure against a planar surface a mechanical contact with this surface where the contact area contains (i.e. encompasses) a square with a side of 10 nm or more, this size is expected to be sufficient to allow the 2D material of the active layer to operate with two dimensions during current measurements, while stay restricted in the third. Also, this size helps to screen the sample surface from the fringing fields and fields originating not from the active layer, especially since the probe may be operated in the contact mode, and the active layer is either exposed or separated from the sample possibly by some layer thin enough or configured to allow tunneling. At the same time, when the contact area has a diameter, for example, of at least: 20 nm, or 50 nm, or 100 nm, or 150 nm, or 1 μm, the probe may be used to provide less local, but more momentum-resolved imaging in at least one lateral direction. Hence, the contact area does not need to be symmetric like a square or a circle: it is sufficient if it includes the square therein as explained above, while a different functionality can be added by making it more elongated in one direction, depending on the specific aim of the measurements. The inventors have considered that on the practical level the contact would lead to a somewhat different functionality if the contact area has dimensions being combinations of a diameter of at least: 20 nm, or 50 nm, or 100 nm, or 150 nm, or 1 μm in one direction, and any diameter from the following list: 20 nm or more, 50 nm or more, or 100 nm or more, 150 nm or more, and 1 μm or more in the perpendicular direction. For example, the larger diameter may be effectively used for the momentum-resolved imaging at cryogenic temperatures (or at room temperature if the coherence length of the carriers is large). At the same time, the diameter of the contact area may be selected not to exceed 1 μm, or 5 μm.

Also, in some examples, the layer arrangement at the apex of the tip may be elongated in a certain lateral direction or configured to become so elongated under the pressure, with a diameter of the contact area selected to allow momentum-resolved imaging of a certain resolution; and configured for a relatively localized measurement in a perpendicular direction. For example, the contact area may have at least: 20 nm, or 50

nm, or 100 nm, or 150 nm, or 1 μm diameter in one direction, and the diameter not exceeding 20 nm or 30 nm in the perpendicular direction. Both measurements may be performed in the contact mode, with scanning the 2D momentum space by rotating the probe with respect to the sample (this is so for all three types of probes, since the probe of the third type may be used for momentum-resolved imaging if the defect-assisted tunneling layer behaves like the tunnel barrier layer at voltages different from the unique voltage(s) of the at least one atomic defect).

The planar surface for testing the probes may be made of graphite, hBN, WSe_2, WS_2, $MoSe_2$, MoS_2, some any other vdW material, or a clean silicon, or another semiconductor (e.g. GaAs). However, in some examples, the exposed layer (be it the active layer, the tunnel barrier, the defect-assisted tunneling layer) has a plateau at the apex with dimensions being combinations of a diameter of at least: 20 nm, or 50 nm, or 100 nm, or 150 nm, or , or 1 μm or more in one direction, and any diameter from the following list: 20 nm or more, 50 nm or more, or 100 nm or more, 150 nm or more, and , or 1 μm or more in the perpendicular direction. In such cases, testing the probe against the planar surface is not needed. The plateau may be, but does not have to be, atomically flat: it will flatten when pressed against the sample. Still, if the exposed layer does not have the plateau before the contact mode is used, possibly due to a too curved form of the apex, it may acquire the plateau shape when operated in the contact mode. To check this, the respective testing may be performed. Testing the probe against the planar surface may not result in a tip crash, i.e. it may be performable without breaking the probe and therefore is non-destructive: the layer arrangement may be sufficiently elastic thanks to vdW layers. Also, the pressure for testing the probes may limited to 1 GPa, or 10 GPa, or 30 GPa in magnitude: such pressures are not expected to lead to the tip crash or to inelastically modify the layer arrangement at the apex.

Additionally, there are examples where the layer arrangement has at least three folds directed from the apex, e.g. from the plateau at the apex; there is even a smaller chance of tip crash for such probes: instead of tearing some layer at the apex, the folds may re-arrange. The same holds for the examples where there is a space between the layer arrangement and the core of the probe, and this space is filled with vacuum, or a fluidic matter, for example, a gas, a liquid, or a gel: with a part of layer arrangement bordering

such a space, it may flex into it and/or out of it and thus allow obtaining the plateau of the desired dimensions at the apex.

In the second group of examples, the tunnel barrier layer may be made of a vdW semiconductor or a vdW dielectric or insulator (e.g. TMDs or hBN). It may have a thickness of up to 9 monolayers.

In the third group of examples, the defect-assisted tunneling layer as well may be made of vdW materials, such as TMDs or hBN. Also, it may be made, for example, of vdW semiconductors including but not limited to WSe_2, WS_2, $MoSe_2$, MoS_2, $TaSe_2$, TaS_2, $NbSe_2$, WTe_2. It may have a thickness of up to 9 layers. The atomic defect may be a vacancy of a single atom or of a complex or a cluster of atoms, a substitutional atom or a complex or a cluster of substitutional atoms, or an interstitial atom or a complex or a cluster of such atoms; or a complex or cluster of defects of two or three of these types.

Since probes from the third group of examples may be used for very localized measurements, in some cases such probes may be adapted to have a diameter of the contact area limited to 40 nm, or 30 nm, or 25 nm, or 20 nm (in all directions; this may be useful, for example, for simultaneous use in conductivity and topography imaging of less smooth samples similarly to CAFM).

The inventors have used some of their invented probes with vdW samples and with a customized AFM setup adapted to allow controlled rotation of a stage holding the sample around the probe besides the common shifting of the sample along two orthogonal linear directions. The sample were rather smooth and while the probe was operated in the AFM contact mode, the primary reason was to apply the necessary force to create the contact for measuring the current rather than measure the particularities of the topography of the sample. The diameter of the probe was larger than of typical CAFM; however, in the third group of examples the resolution of the obtained current map corresponds to the size of the atomic defect(s) (if there is more than one atomic defect as described above in the defect-assisted tunneling layer, then the used defect can be switched by changing the voltage between the active layer and the sample to match to the unique voltage corresponding to the peak of the desired defect). At the same time, in the first and second group of examples measurements have been performed with twisting the probe and thereby scanning the relative momenta of the states in the probe with respect to those in the sample; and thus obtaining momentum-resolved tunneling data (where for probes in

the first group of examples carriers tunnel directly between the sample and the active layer of the probe, and in the second group they tunnel via the tunnel barrier layer).

At the same, the measurements can be conducted with all three types of probes because, quire remarkably, debris and probe wear have not presented an obstacle for such measurements as for CAFM, despite the larger diameter of the probe than in typical CAFM and consequently a higher probability of existence of debris. Apparently, debris is pushed out from the interface between the invented probes and samples, for example, due to adhesion between vdW layers in the sample and the probe and elasticity of the layer arrangement of the probe (and possibly elasticity of the sample): the state with a dirt between the sample and the probe has to be energetically unfavorable. This has to be even more common case for the probes where the layer arrangement has at least three folds directed from the apex; and/or in cases where the layer arrangement where there is a space between the layer arrangement and the core of the probe, as mentioned above. Both of these features are realized, for example, in a tent structure as discussed below.

BRIEF DESCRIPTION OF THE DRAWINGS

In order to better understand the subject matter that is disclosed herein and to exemplify how it may be carried out in practice, embodiments will now be described, by way of non-limiting examples only, with reference to the accompanying drawings:

Figs. 1A-C present, respectively, schematic illustration of the probe with the exposed active layer according to the present disclosure (side view); schematic illustration of the probe with the exposed tunnel barrier layer according to the present disclosure (side view); and schematic illustration of the probe with the exposed defect-assisted tunneling layer according to the present disclosure (side view).

Fig. 2 schematically shows an example of a probe contact area (a front view) according to the present disclosure.

Fig. 3A and 3B schematically show examples of a connection of the active layer of the probe with its contact electrode and the support layer of the probe, according to the present disclosure.

Fig. 4 schematically illustrates an example of a probe with a gate electrode layer according to the present disclosure.

Figs. 5A and 5B schematically illustrate that a probe according to the present disclosure may have a proto-plateau.

Fig. 6 schematically shows an example of an SPM/AFM apparatus, according to the present disclosure, allowing to rotate a stage for carrying a sample with respect to a head holding an AFM cantilever.

Figs. 7a-j to 10a-e (see the descriptions in the section "Additional Description" below) exemplify the operational principles of Quantum Twisting Microscope (QTM), wherein **Figs. 7a-j** shows the QTM setup and in-situ twistronics experiments; **Figs. 8a-h** shows momentum resolved tunneling between two twisted graphene monolayers; **Figs. 9a-i** shows QTM imaging of the energy bands of twisted bilayer graphene (TBG); and **Figs. 10a-e** shows imaging the effects of applied pressure on the TBG energy bands.

Figs. 11a-f - 28 (see the descriptions in the section "Supplementary Information" below) illustrate specific non-limiting examples of the probe fabrication and operation techniques; wherein **Figs. 11a-f** shows the QTM tip characterization; **Figs. 12a-d** shows QTM flat side substrate and devices; **Figs. 13a-c** shows room-temperature QTM measurement setup; **Fig. 14** shows the bias dependence of top/bottom chemical potential $\mu_{T/B}$ and electrostatic potential ϕ for MLG-MLG tunneling junction; **Fig. 15** is a schematic of the charge-neutral MLG-MLG tunneling experiment (of Figs. 8a-h above); **Figs. 16a-b** shows (a) measured $\frac{d^2I}{dV^2}$ from Fig. 8c above, with the local maximum (minimum) being traced at positive (negative) bias, along the 'onset' features (black dots), and (b) plot of the black dots from panel together with bare Dirac dispersion (Eq. S5.5) with $v_F = 1.05 \cdot 10^6 m/s$ (blue) and Dirac dispersion that is renormalized by interactions; **Figs. 17a-b** shows rescaling rotation angle θ to the electrostatic potential ϕ; **Figs. 18a-f to 20a-f** show for the same measurement, respectively, back-gate voltage dependence of momentum-resolved tunneling current in a MLG - MLG junction, Back-Gate voltage dependence of dI/dV, and Back-Gate voltage dependence of d^2I/dV^2; **Fig. 21** is a schematic of the MLG-MLG tunneling junction for experiments with a finite back gate voltage; **Figs. 22a-b** show measured and calculated d^2I/dV^2 vs. θ and V_b, at $V_{BG} = -10V$ (similar to Figs. 20c,f); **Fig. 23** shows determination of the electron lifetime at low bias; **Figs. 24a-c** shows a second toy model, explaining the momentum resolved features; **Fig. 25** shows how the 'onset' and 'Dirac matching' features evolve between low temperature ($k_BT = 1meV$,

blue) and room temperature ($k_BT = 25meV$, dashed red); **Figs. 26a-g** shows comparison of the second toy model with the measurements; **Figs. 27a-e** illustrate how the main features obtained in the experiments using toy models appear in the full calculation; **Fig. 28** shows the energy band shift, ϕ, as a function of V_b, (red dots) extracted from the feature that follows the MLG bands in the MLG-TBG measurement in Fig. 9d.

Fig. 29 (see the description in the section "Experiments with a probe of a smaller lateral size" below) shows an image of the whole area of sample detected by a probe fabricated by the inventors while being moved along the surface of the sample and imaged multiple times by the defects.

DETAILED DESCRIPTION OF THE ASPECTS AND EMBODIMENTS

Reference is made to **Figs. 1A-C** schematically exemplifying probes according to the three groups as mentioned above, respectively. Figs. 1A-C show side views of the probes.

A probe **10** of **Fig. 1A** is an exemplary probe which may be used for mechanically contacting a sample and conducting electrical measurements on the sample. It includes a tip presented in this example by a core **12** with an apex **12A**. Also, probe **10** includes an active layer **16** presenting a 2D material of not more than 10 monolayers coupled by vdW forces, and a support layer **14** of a vdW material including layers **14-1** to **14-n**. The active layer **16** is placed on the support layer **14** at the apex **12A**; and it is further away at the apex **12A** from the core **12** than the support layer **14**. In other words, the active layer **16** and the support layer **14** form a vdW heterostructure covering the apex **12A**, and the vdW heterostructure is turned with the support layer **14** towards the apex **12A**. The active layer **16** at the apex **12A** is exposed for contacting a sample.

In probe **10**, a layer arrangement, covering apex **12A** and including the support layer **14** and the active layer **16**, i.e. their vdW heterostructure, has a plateau at the exposed layer. This plateau contains a square with a side of 10 nm or more. Hence, the contact area is expected to contain the square with a side of 10 nm or more under pressure against a planar surface.

The layer arrangement at the apex **12A** in probe **10** conducts an electric current substantially, or even only, in a lateral dimension and substantially, or only, through the active layer **16**.

In **Fig. 1A** the active layer **16** extends away from the apex **12A**, but along core **12** of the tip, and it stays exposed on the side of the tip, to which it is attached via the extension of the support layer **14**. The extension of the active layer thus may be used for connecting to a contact electrode, which could lie on be pressed to the exposed extension of the active layer. In different examples, the active layer may extend away from apex **12A** towards the contact electrode without being mechanically connected to the core **12**. The contact electrode may be bulk and may be included into the probe, or it may be separate from the probe. For example, the contact electrode may be made on a side of the core **12** and be included into the tip as it's another part, additional to core **12**; or if the core **12** is grown on or attached to a substrate, the contact electrode may be made on a substrate. The active layer **16** may be on top of or beneath the contact electrode where they intersect.

In **Fig. 1B** a probe **20** is shown. In this example, the probe includes an active layer **26** instead of **16**; and it includes a tunnel barrier layer **28**. Other elements are the same as in Fig. 1A. The active layer **26** may differ from the active layer **16** in some respects: on the one hand, active layer **26** does not have engage in a direct contact with the sample, but on the other hand it has to be compatible with tunnel barrier layer **28**, for example, possibly to attach this layer to probe **20** if it is not attached to this probe in some other way (for example, to a substrate if it is included into the probe).

Fig. 1C shows an example of a probe **30** in which the active layer **26** is covered by a defect-assisted tunneling layer **38A**, which is exposed. This defect-assisted tunneling layer **38A** includes an at least one atomic defect **38B** presenting a flow path for a tunneling current between the sample and the active layer **26**. The layer arrangement, which at the apex **12A** includes the defect-assisted tunneling layer **38A** in addition to the heterostructure of the support layer **14** and the active layer **26**, is allowed to conduct the electric current at least by tunneling through this defect-assisted tunneling layer **38A** via the atomic defect **38B** when the applied voltage coincides with the peak of the tunnel conductance of the defect, and then in a lateral dimension and through the active layer **26**. By the "atomic defect" is meant either one or a complex (or cluster) of few missing atoms, one or a complex of few substitutional atoms, one or a complex of few interstitial atoms; or a complex combining defects from two or three of these types. Hence, the

current will depend on the free carrier density of state and the local electrostatic potential in the sample in a vicinity of the defect and the energy distribution of the carriers.

Fig. 2 schematically shows an example of a front view of a contact area CA of each of the probes **10**, **20** and **30** against a planar surface. For probe **10**, the exposed layer is the active layer **16**; for probe **20**, the exposed layer is the tunnel barrier layer **28**; and for probe **30**, the exposed layer is the defect-assisted tunneling layer **38A**. In each case, the contact area contains a square **S1** with a side of 10 nm or more.

Fig. 3A provides an example how a contact electrode may be added to the probe, in accordance with one of the options mentioned above. In this example, probe **10A** is similar to probe **10**, but its active layer **16** extends along the core **12** further away from apex **12A** than the support layer **14**. The tip of the probe **10A** is equipped with a contact electrode **18** grown, placed, or deposited on the core **12**, and the active layer **16** extends to this contact electrode **18**. Still, in all cases, according to another option the contact electrode may additionally or alternatively be deposited on top of the active layer.

Fig. 3B provides an alternative example with respect to how the active layer 16, the support layer **14** and the core **12** may be positioned with respect to each other on the side of the core **12**. In this example, probe **10B** is similar to probes **10** and **10A**, but it has an active layer extension **16E** of a shape with folds, and a support layer extension **14E** of another shape with folds. This may happen, for example, due to a different combination of an angle of between the core side wall and the apex **12A** and flexibilities of the active and support layers. In this example, the active layer extension **16E** does not adhere to the support layer extension **14E** at some segments of its length even though it covers the support layer extension as the most proximate layer from one side; i.e. in the present example there is a gap between the active layer **16** and the support layer **14** (even two such gaps in Fig. 3B). Similarly, support layer extension **14E** does not adhere to the core **12** in its certain segment (however, it has to be remembered that the support layer extension and the active layer extension may adhere to each other in a differently oriented cross-section; and similarly for the support layer extension and the core).

Such gaps or spaces may be used to reduce a risk of tip crash: with a part of the layer arrangement bordering such a gap, this part (i.e. one or more of respective segments in Fig. 3B) may flex into it and/or out of it. Depending on the measurements (for example, cryogenic or not), such spaces may be filled with vacuum, or a fluidic matter, for example,

a gas, a liquid, or a gel, and thus allow the plateau of the desired dimensions at the apex to be formed upon the contact with the planar surface.

Fig. 4 schematically illustrates that a gate electrode layer **13** may be added to the probe. In this specific example probe **10C** is based on probe **10**, with the gate electrode layer lying between apex **12A** and the support layer **14**. However, a gate electrode layer such as the layer **13** also can be used in all other probes of the present disclosure. By applying a voltage bias between the gate electrode layer and the active layer, the properties of the active layer can be continuously modified, thereby allowing to change the properties measured in the experiment. Specifically, the changes may involve tuning the carrier density in the active layer, the density of states, and/or the workfunction of the active layer. Each of these parameters is useful for controlling the current measurement. For example, in the third embodiment (with the defect-assisted tunneling layer) a voltage bias between the gate electrode layer and the active layer influences the workfunction of the latter, which in turn gates the defect and shifts its energy level. The gate can thus be used to continuously tune the energy level of the defect.

Figs. 5A and 5B schematically illustrate that a probe may lack a plateau containing the square of 10 nm size on the exposed layer when it is not used, but in such a case its layer arrangement **LA** may have a convex surface region **PP** (a proto-plateau) flexing under pressure or mechanical contact with a sample into a plateau **P** containing such a square. This possibility is relevant to all probes according to the present disclosure (including the illustrated exemplary probes **10**, **20**, **30**, **10A** and **10B** in those their modifications which without pressure lack the plateau covering the square of 10 nm).

Fig. 6 schematically shows an example of an SPM apparatus **100** according to the present disclosure. In the present example, the SPM apparatus is implemented as an AFM apparatus, but a skilled person would readily understand from Fig. 6 also how an STM apparatus may be configured according to the present disclosure: the AFM apparatus would be replaced with an STM apparatus, and an STM probe would be used instead of the AFM cantilever. This STM probe may be implemented as any of the probes in the present disclosure.

Hence, the AFM apparatus **100** includes a stage **102** to carry a sample, a head **104** to hold an AFM cantilever above the stage **102**, an electric motor **106** for laterally rotating the stage **102** with respect to the head **104**, and a control unit **108** for controlling the lateral

rotation of the stage **102** with respect to the head **104** with an accuracy better than 5 degrees, or 1 degree, or 0.1 degree, or 0.01 degree, or 0.001 degree to provide a desired orientation alignment between them. The arrow in Fig. 6 indicates the control. Fig. 6 represents both an AFM that works at room temperature and also an AFM that works at cryogenic temperatures.

Such a modification of the AFM according to the present disclosure is useful for conducting momentum-resolved measurements, to scan along the momentum space without disengaging the probe in the contact mode from the sample. Also, it is useful for forming a hybrid interface with a tunable twist angle and probing its physical properties at different twist angles. These properties as well may be local, for example, the local conductivity or carrier density.

The following section called "Additional Description", and then related to it "Supplementary Information", includes a description which, along with figures referred therein, provides some further details of the inventors' considerations and specific experiments, as well as more examples of probes corresponding to the disclosure above, including information on some fabrication techniques and results which such probes have already brought about:

Additional Description

The Quantum Twisting Microscope:

The scanning probe microscopy has revolutionized the way electronic phenomena are visualized. While present-day probes can access a variety of electronic properties at a single location in space, a scanning microscope that can directly probe the quantum mechanical existence of an electron at multiple locations would provide direct access to key quantum properties of electronic systems. Here, a conceptually new type of scanning probe microscope is demonstrated – the Quantum Twisting Microscope (QTM) – capable of performing local interference experiments at its tip. The QTM is based on a unique van-der-Waals tip, allowing the creation of pristine 2D junctions, which provide a multitude of coherently-interfering paths for an electron to tunnel into a sample. With the addition of a continuously scanned twist angle between the tip and sample, this microscope probes electrons in momentum space similar to the way a scanning tunneling microscope probes electrons in real space. Through a series of experiments, the inventors have demonstrated room temperature quantum coherence at the tip, studied the twist

angle evolution of twisted bilayer graphene, directly imaged the energy bands of monolayer and twisted bilayer graphene, and finally, applied large local pressures while visualizing the evolution of the flat energy band of the latter. The QTM opens the way for novel classes of measurements and experiments on quantum materials.

An electron in a solid is a quantum mechanical object best described by an extended wave function, reflecting its existence in a superposition of spatial locations. The STM dramatically changed how electrons in real space can be visualized. It was followed by a large array of other scanning probe techniques that now allow local measurements of various electronic properties. To date, existing scanning microscopes can only probe electronic properties apparently at one location at a time. Therefore they are unable to probe the interference of several tunneling trajectories, which would map the evolution of the quantum mechanical phase in space. To do so requires a scanning interferometer that probes an electron at several locations simultaneously and quantum coherently.

Thus, the inventors demonstrate a conceptually new type of scanning probe microscope – the Quantum Twisting Microscope (QTM) – capable of performing local interference experiments at its tip. The invented technique is based on a unique van-der-Waals (vdW) tip, which is brought into contact with a vdW sample, forming a 2D interface that can be twisted and spatially scanned with high angular and positional precision. The QTM enables at least two orthogonal and complementary classes of experiments: 1) "In-situ twistronics" – measuring a continuously twistable interface between a pair of vdW materials (e.g. twisted bilayer graphene). Here, the active vdW layers are placed in the tip and sample in direct contact, such that their wavefunctions strongly couple, and then the transport properties of the hybridized interface are probed. 2) Momentum-resolved tunneling – Here, a tunnel barrier (e.g. a few layers of a transition metal dichalcogenide) is inserted between the active vdW layers in the tip and sample. This barrier decouples their wavefunctions, allowing the tip to act as a momentum-resolved probe (non-invasive) for the sample's energy bands. Since an electron can coherently tunnel into a sample at many locations along the 2D interface, this junction acts as an interferometer on a tip. Specifically, this implies that in the absence of electron-phonon, electron-electron and impurity scattering, an electron would tunnel only between states of equal momenta. In this modality, the microscope's twisting degree of freedom

is used for scanning an arc in the momentum space of the sample, and imaging along it the sample's energy bands.

The QTM's Operating Principle

To date, existing approaches for in-situ twisting experiments are based on electrical devices fabricated with a rotatable part and an external mechanical device, such as an atomic force microscope (AFM) tip, which pushes this part. The QTM of the inventors, in contrast, elevates the AFM tip to become an integral part of the twisted device, which is now split into two parts: the first is a standard vdW device formed on a flat substrate (**Fig. 7a**, Supp. Info. S2). The second is a vdW device formed on a specially-designed pyramid at the edge of an AFM cantilever (**Fig. 7b**, Supp. Info. S1). Both sides have independent electrical contacts. The inventors have used a commercial AFM to bring the two parts into contact and to maintain a constant force across the interface throughout the entire experiment (**Fig. 7c**). On the AFM stage, they have mounted a piezoelectric rotator with X and Y nanopositioners on top (Supp. Info. S3). This setup allows rotating the bottom sample with an angular resolution of $0.001°$ and positioning the point of interest in the sample at the center of rotation. In addition, the standard scanning capability of the AFM (in X and Y directions) enables lateral scanning of the tip across the sample.

A useful ingredient of the QTM is its tip design, facilitating the formation of a flat vdW at its apex. To achieve this in some non-limiting experiments, the inventors started with focused-ion-beam deposition of a platinum pyramid ($\sim 1.2 - 1.6 \mu m$ tall) on a tipless AFM cantilever (**Fig. 7e**). This is followed by sequentially transferring graphite, hBN and the active vdW layer (e.g., monolayer graphene) on the pyramid using a polymer membrane. The graphite screens the substrate's disorder potential, and the hBN acts as a spacer. **Fig. 7f** shows an AFM image of the resulting tip: visibly, the vdW stack forms a "tent" over the pyramid with three or more folds climbing up to the pyramid's apex. At the apex, a flat plateau spontaneously forms in the vdW stack, whose corners are determined by the folds (**Fig. 7g**). The typical bending angles of the vdW tent ($\sim 10 - 30°$) are smaller than the pyramid's angle ($\sim 45°$). Thus, apart from a small touching point at the apex, the tent is mostly suspended (Supp. Info. S1). Due to the flexural rigidity of the graphite/hBN layers, the formed vdW plateau is wider than the pyramid apex, resting on it as a pivoting point. Therefore, when this tip is brought into

contact with the sample, the plateau self-aligns its tilt to become parallel to the sample. By varying the pyramid geometry and graphite/hBN flake thicknesses (typically tens of nanometers), the inventors have achieved plateaus of varying linear dimensions between 50nm and 1μm. These dimensions are small enough to make their QTM tip a local scanning probe, yet large enough (~1000 atoms across or more) for wavefunctions on the plateau to have a well-defined momentum ($\Delta P \sim 1/1000$ of the Brillouin zone size). Contrary to etched boundaries in lithographic devices, the active vdW layer on the plateau is continuously extended to the rest of the pyramid, avoiding dangling bonds or buckles. This setting makes the wavefunctions smoothly connect to the rest of the vdW layer on the pyramid. **Fig. 7d** overlays the measurement circuit on a schematic cross-section of the junction: a bias voltage, V_b, is applied between the two active layers (vdW crystals 1 and 2), and the corresponding current, I, is measured. Buried bottom and top graphite layers can serve additionally as bottom and top gates for the junction.

In-Situ Twistronics.

The inventors have started with a "twistronic" measurement of a twistable interface between two graphene monolayers (MLG) in direct contact. This interface has remained elusive for existing in-situ twistronics techniques since MLG easily crumbles upon twisting. **Fig. 7h** shows the MLG-MLG interface conductance, dI/dV, measured vs. twist angle, θ, at T = 300K. Throughout the entire measurement, the sample and tip are kept in continuous contact. The layers do not show any sign of locking at $\theta = 0°$, and the conductance traces are highly reproducible, highlighting the unique mechanical robustness of the QTM junction. The conductance is mirror symmetric around $\theta = 30°$, $(\theta \rightarrow 60° - \theta)$, where its value is minimal. It rises continuously toward $\theta = 0°$ but plateaus at small angles ($|\theta| \lesssim 4°$) where it becomes limited by the resistance away from the tip ("contact resistance"). Similar to the measurements in graphite-graphite and graphite-MLG interfaces by other groups, the inventors have seen extremely sharp conductance peaks at $\theta = 21.8°$ and 38.2°. At these angles, the two layers form commensurate stackings in real-space with a $\sqrt{7} \times \sqrt{7}$ supercell (**Fig. 7i**).

On the origin of the large conductance enhancement at commensurate angles, the inventors contemplated the following. One possibility is a better real-space registry of the atoms in the two layers. However, by definition, whenever unit cells are commensurate

in real-space, their corresponding Brillouin zones (BZ) are also commensurate in k-space, implying that at commensurate angles, momentum states are also matched. Specifically, at $\theta = 0°$ the Dirac cones of the two layers overlap at the corners of the 1st BZ, and at $\theta = 21.8°$ they overlap at the corners of the 3rd BZ (**Fig. 7i**). The relevance of real vs. momentum space matching is directly connected to the quantum coherence of the 2D tunnel junction: in an incoherent junction, the tunneling events of electrons at different locations are independent, and sum up classically to yield the total current (Fig. 7j, top). In such a case only the real-space matching is relevant. Conversely, in a coherent junction, tunneling events at different locations interfere, yielding a tunneling current that is sensitive also to the local phases of the wavefunctions (**Fig. 7j**, bottom). In particular, tunneling is possible only between wavefunctions with matching energy and momentum.

Local Momentum Resolved Tunneling

To observe also the momentum conserving nature of the QTM the inventors have added a tunneling barrier between the two MLG layers (trilayer WSe_2, **Fig. 8a**, top inset). This barrier suppresses the hybridization between tip and sample, enabling the tip to act as a probe for the unperturbed energy bands of the sample. The barrier also significantly increases the tunnel junction resistance, assuring that an applied bias falls predominantly across this junction and that the measurement is not affected by contact resistance even near $\theta = 0°$. **Fig. 8a** shows the measured tunneling current, I, vs. the interlayer bias, V_b, and θ at T = 300K. Around $\theta = 0°$, I increases slowly with V_b at low bias, and then sharply increases along a curved-X feature in the $\theta - V_b$ plane. Interestingly, this increase is followed by a sharp drop at slightly higher V_b. At much higher biases ($\sim 0.8V$), I rises again, this time exponentially with V_b, and rather homogenously for all θ. **Fig. 8b** shows the measured conductance, dI/dV. Here, the sharp drop of I manifests as a strong negative differential resistance (NDR), as was seen previously in lithographic devices. Finer details are revealed when the inventors have plotted the second derivative, d^2I/dV^2 (**Fig. 8c**): in addition to the strong curved-X (dashed white lines), the inventors have observed a straight-X feature (dashed black lines), along which d^2I/dV^2 shows peaks (/dips) on the positive (/negative) bias side.

To understand the observed curved-X feature three points in the $\theta - V_b$ plane (**Fig. 8d**) can be considered: at point 1 ($\theta = 0°$, small V_b) the atoms of the two layers

are registered in real-space and their energy surfaces are matched in momentum-space (**Fig. 8g**, panel 1). Increasing V_b while keeping $\theta = 0°$ (point 2) maintains the real-space registry but offsets the relative energies of the Dirac cones. Consequently, for almost all energy slices within the bias window, the equal energy states have mismatched momenta (one such slice is shown in panel 2 of **Fig. 8g**). Thus, the observed drop of I is concomitant with the loss of energy-momentum-matched eigenstates in the two layers. By twisting the layers to a finite θ, while maintaining V_b (point 3), the layers lose the registry in real space but regain overlap of states in momentum space, enabling momentum-conserving tunnelling processes (**Fig. 8g** panel 3). Indeed, at this point the measured I becomes large again, demonstrating its momentum conserving nature. The inventors have estimated the level of momentum conservation from a plot of I vs. θ at small $V_b = 40mV$ (**Fig. 8a**, right inset). The extremely narrow peak ($\Delta\theta \approx 0.2°$) implies an excellent momentum resolution, ~0.004 of the BZ size, comparable to state-of-the-art ARPES detectors. In the experiment in **Figs. 8a-h**, the back gate voltage is zero and the measurement shows a good symmetry between positive and negative bias directions, suggesting an overall charge-neutral system. Additional experiments with finite back gate voltages (Supp. Info. S6) further show a rich evolution of the features with the total charge in the system.

The inventors have compared their measurements to theory of momentum-resolved tunneling between twisted layers presented in Bistritzer, R. & MacDonald, A. H. Transport between twisted graphene layers. *Physical Review B* **81**, 245412 (2010). See **Figs. 8d-f**. Since the quantum and geometrical capacitances of the junction are generally comparable, the applied bias divides into shifts of the chemical potential of the top and bottom layers, μ_T and μ_B, and an electrostatic potential shift between them, ϕ, namely, $V_b = \phi + \mu_B - \mu_T$ (**Fig. 8h**). To calculate the tunneling current at any point in the $\theta - V_b$ plane, the inventor have first determined μ_T, μ_B and ϕ by solving the above equation self-consistently with the equations-of-state of the individual layers, $\mu_T(n_T)$ and $\mu_B(n_B)$, (Supp. Info. S4). They then have summed the tunneling rates for all energy-momentum conserving tunneling processes within the bias window. We further add a Nordheim-Fowler contribution due to the breakdown of the WSe_2 barrier. All expressions include the effects of finite temperature and lifetime. Overall, the agreement with the experiments has been excellent, both in terms of the locations of the various features, and

in terms of their relative magnitude. The theory further has allowed the inventors to identify the experimentally observed features: the straight-X corresponds to the onset of momentum resolved tunneling, happening when the Fermi surface of one layer touches the empty bands of the other layer ('k-resolved onset' condition, **Fig. 8f**). The curved-X feature corresponds to nesting of the energy bands ('nesting' condition, **Fig. 8f**). Here, a macroscopically large number of energy-momentum conserving states become available to tunnel, explaining the large increase of I along this feature. With a further increase of V_b or a further decrease of θ most of the states cease to be energy-momentum conserving, explaining the consequent large drop in I.

The simplicity of graphene's dispersion has allowed the inventors to obtain analytic expressions for the k-resolved onset and nesting conditions. Specifically, for a non-interacting charge-neutral system, the onset condition becomes (Supp. Info S5) $V_b = \hbar v_F K_D \theta$, where K_D is the Dirac point momentum. Namely, V_b and θ substitute the energy and momentum in the standard Dirac equation. Overlaying this expression on the measurement (dashed black lines, **Fig. 8c**) yields an excellent fit with $v_F = 1.05 \pm 0.02 \cdot 10^6 m/s$, consistent with a measured Fermi velocity of graphene. Additionally, the nesting line provides the energy shift between the bands, ϕ, at any value of V_b, from which the electronic compressibility of the system can be straightforwardly determined (Supp. Info. S5). This measurement thus provides simultaneous information about the excitation spectrum of the system and its thermodynamic properties.

Momentum-resolved Imaging of Twisted Bilayer Graphene Energy Bands

Having probed the energy bands of MLG, the inventors have turned to a system with more intricate energy bands – twisted bilayer graphene (TBG). The experiment comprises of a MLG probe, a bilayer Wse_2 barrier, and TBG with a 2.7° twist (**Fig. 9a**). In momentum space, the TBG mini-BZ hosts at its corners the Dirac cones of the underlying top and bottom graphene sheets (red and blue circles at K_{top} and K_{bot}, (Fig. 9b). In the experiment, the MLG is rotated with respect to the TBG, and correspondingly its Dirac cone (purple circle, **Fig. 9b**) scans the energy bands of the TBG along a constant radius arc in momentum space (dashed purple arc, Fig. 9b), cutting precisely through K_{top} and K_{bottom} and passing very close to the Γ_M points of adjacent mini-BZ's. Along this k-space linecut, the TBG is theoretically predicted to

exhibit the "flat bands" around zero energy and remote bands at higher energies (blue and black in **Fig. 9c**). **Fig. 9d** shows the dI^2/dV^2 measured vs. V_b and θ. The second derivative diminishes the smoothly evolving background, allowing to clearly resolve the key features. The measurement shows a wealth of features, the most prominent of which are traced in **Fig. 9f**. Interestingly, it exhibits a superposition of the 'system' and 'probe' energy bands, including the TBG's flat bands (blue), remote bands (black), as well as two copies of the MLG Dirac bands (purple).

A theoretical calculation of the MLG–TBG momentum-resolved tunneling (**Fig. 9e**) shows excellent agreement with the experiment, down to small details. Specifically, the theory reproduces the features due to the flat and remote TBG bands, as well as the two displaced copies of the MLG Dirac bands. Furthermore, from the theory the inventors have been able to conclude that the band imaging is performed effectively by Dirac points: for example, when the MLG Dirac point matches in energy and momentum a state on the TBG flat bands (left inset, Fig. 9e), the d^2I/dV^2 exhibits a peak. This peak of d^2I/dV^2 corresponds to a minimum in I, reflecting the minimal tunnelling density of states at the Dirac point. Similarly, when one of the two TBG's Dirac points matches the MLG bands (right inset, **Fig. 9e**) a strong feature appears in dI^2/dV^2 (this time with an opposite sign, see toy model in Supp. Info S8). Consequently, the two TBG Dirac points trace out two copies of the MLG bands, displaced by $\Delta\theta = 2.7°$. In addition to these 'Dirac matching' conditions that are insensitive to band filling, there are also 'onset' features, which appear whenever the Fermi level of one side (tip/sample) crosses the bands of the other side (for details see Supp. Info. S8).

The inventors have obtained the flat-band energy dispersion directly from the measurements by using the simultaneously measured MLG Dirac bands to calibrate the energy shift at each V_b (Supp. Info. S8). **Fig. 9h** compares the extracted $\epsilon(k)$ of the flat bands (red and grey dots) with the prediction of the BM model (blue). The overall agreement is rather good, although the experiment shows an electron-hole asymmetry (~12% along the $K_{bot} - M - K_{top}$ branch and ~20% along the $K_{top} - \Gamma_M$ branch), contrasting the nearly-perfect e-h symmetry of in the BM model. The inventors' measurements also reveal a quantity that is inaccessible to other probes – the layer polarization of individual wavefunctions at different momenta: visibly, when the MLG lattice is rotationally aligned with the top TBG layer ($\theta = +1.35°$) the measured

dI^2/dV^2 amplitudes are strong. In contrast, when the MLG is rotationally aligned with the bottom TBG layer ($\theta = -1.35°$) they are substantially weaker. This highlights the fact that the experiment probes the weight of the wavefunction on the top layer. In **Fig. 9i** the inventors have plotted the magnitude of I along the traced flat band features (blue, **Fig. 9f**) between K_{top} and K_{bot} (dots), and compared it with the layer polarization as a function of k from the BM model. The inventors have been able to see that this quantity is indeed a good proxy for the layer polarization.

Imaging Twisted Bilayer Graphene Energy Bands Under Pressure

The inventors have proceeded also to showing another unique capability of the QTM – its ability to apply a large local pressure while simultaneously imaging the way it affects the energy bands. Pressure provides a key tuning parameter for vdW materials, as it directly controls the interlayer tunneling. In TBG, this was predicted and shown to tune the flat bands in and out of the magic-angle condition. However, the challenges in cryogenic pressure cell transport experiments have limited such experiments to very few measurements. Here, instead, the inventors have used the ability of the AFM to apply μN-scale forces across the small QTM junction to achieve GPa-scale pressures at the interface (**Fig. 10a**, inset).

Figs. 10a-c plots the measured dI^2/dV^2 vs. θ and V_b, for the junction of **Figs. 9a-i**, but now under pressures of $P = 0.01, 0.4$, and $0.68\ GPa$. Each frame is taken with a constant pressure during twisting, and the results are reversible upon repeatable increase and decrease of pressure between frames. Visibly, with increasing P the flat bands gradually shrink toward zero V_b, whereas the remote bands get further away from zero V_b. To show this more quantitatively, in **Fig. 10d** the inventors have traced the flat and remote bands over a larger sequence of pressures. The inventors have been able to clearly see the opposite motion of the flat and remote bands with pressure (arrows). This contrasting response reflects a band anti-crossing that increases with P, as expected from increased interlayer tunneling. Converting V_b to the energy shift using the simultaneously measured MLG bands, the inventors have plotted the energetic width of the flat bands vs. P (**Fig. 10e**). Notably, the width shrinks linearly with P, reaching a 17% reduction at $P = 0.68\ GPa$. This compares reasonably to the 6-14% reduction predicted theoretically. A naïve linear extrapolation of the measurements conducted by

the inventors would suggest that the bands of 2.7° TBG could become fully flat at $P \approx 4GPa$, well within the pressures achievable by AFM without damaging graphene. This could lead to fully flat bands with a moiré periodicity that is much shorter than in magic-angle TBG, and correspondingly to proportionally larger Coulomb interactions, potentially taking this system into uncharted regimes of strong interactions.

The QTM demonstrated here and based on the probes and techniques according to the present disclosure may be employed in industrial and scientific setting for characterization of various devices. Additionally, it may be used for creating highly controllable novel interfaces between a large variety of quantum materials. Specifically, it enables continuous control with 0.001° resolution of one of the critical parameters of these interfaces – their twist angle. In the Additional Description with Supplementary Information, the inventors have explored systems based on graphene and WSe_2, but the technique should be applicable quite generally to a plethora of layered conductors, and superconductors.

In any case, in view of the above, it is clear that the inventors have enabled a novel scanning microscope that has direct access to the energy-momentum dispersion of electronic systems. As such, it may probe the dispersion of any excitation, charged or neutral, as long as it can be excited by a tunneling electron. The measurements can be performed at large magnetic fields, with variable carrier density and electrical displacement fields controlled by local gates, and with a continuously tunable pressure. As for the lateral scanning degrees of freedom of the QTM, they result naturally from its SPM (AFM or STM) platform. These degrees of freedom allow preforming spatially-scanned momentum resolved measurements within electronic devices with a high spatial resolution (~100nm). Lateral scanning also provides control over the lateral displacements between vdW materials, most likely down to atomic dimensions, capturing another key tuning parameter of the energy dispersions at these interfaces.

The following presents more details on **Figs. 7a-j to 10a-e**:

Figs. 7a-j: The Quantum Twisting Microscope setup and in-situ twistronics experiments. **a**, **b** and **c**, Illustrations of the components of the QTM. **a**. van-der-Waals (vdW) heterostructure assembled on a flat substrate with electrical contacts. **b.** vdW heterostructure assembled on a pyramid positioned near the edge of an atomic force microscope (AFM) cantilever, with electrical contacts. At the apex of the pyramid, the

vdW-device-on-tip has a flat plateau. **c.** These devices are brought into contact using a commercial AFM, fitted with a piezoelectric rotator that allows to control the relative angle between tip and sample, θ, continuously with a 0.001° resolution, in addition to the usual lateral (X/Y) scanning capabilities of the AFM. **d**. Measurement circuit plotted over a schematic cross-section of the QTM junction. A voltage bias, V_b, is applied between the two active vdW layers (vdW crystals 1 and 2), and the corresponding current, I, is measured. Buried top and bottom graphite gate voltages, V_{BG} and V_{TG}, can modify the local carrier density and electric field in the junction (in this Additional Description with Supplementary Information, the top gate is physically shorted to the top graphene layer such that V_{TG} is identically zero**)** **e**. SEM image of an AFM cantilever with a custom-made platinum pyramid deposited by a focused-ion-beam. **f.** The topography of a vdW-device-on-tip (graphite/hBN/monolayer graphene (MLG)), imaged by AFM. The vdW layers form a tent over the Pt pyramid, with folds (dashed white) leading to a flat plateau. **g.** Zoomed-in AFM image around the pyramid's apex (peak-force-error signal), showing the spontaneously formed flat plateau. **h.** Measured conductance, dI/dV, vs. rotation angle, θ, between two graphene monolayers (MLG, top inset) in direct contact, $V_b = 50mV, V_{BG} = 0, T = 300K$. The two vdW devices are kept in continuous contact throughout the measurement. **i**, Real-space and momentum-space registry for the commensurate angles of 0° and 21.8°. **j**, Illustrations of the incoherent and coherent tunneling across the 2D junction: in the former, electrons tunneling at various locations are incoherent, and the tunneling is proportional only to the local wavefunction squared. In the latter, tunneling trajectories within the coherence length interfere, and the tunneling is sensitive also to the variation of the phases of the top and bottom wavefunctions along the junction.

Figs. 8a-h: Momentum resolved tunneling between two twisted graphene monolayers. **a.** Top inset: Schematic cross-section of the experiment, comprising of an MLG/trilayer WSe_2/MLG tunnel junction. The WSe_2 tunnel barrier suppresses the hybridization between the MLG layers allowing one to probe the unperturbed energy bands of the other. Main panel: Tunneling current, I, measured as a function of rotation angle, θ, and interlayer bias, V_b, at $T = 300K$. Right inset: a plot of I vs. θ at $V_b = 40mV$ (along the black dashed line in the main panel). The peak's full-width-half-max (FWHM) is 0.2°. **b.** A lock-in measurement of the differential conductance, dI/dV, as a function

of θ and V_b, showing strong negative differential resistance (NDR, blue) along a curved-X feature. The measurement shows a good symmetry between the positive and negative bias directions. **c.** The second derivative, d^2I/dV^2, vs. θ and V_b, obtained by a numerical derivative of the data in panel b. The black and white dashed lines correspond to two specific alignment conditions between the bands, 'k-resolved onset' and 'nesting', shown in panel f and described in the main text and Supp. Info. S5 . **d-f.** Theoretically calculated momentum conserving tunneling I, dI/dV, and d^2I/dV^2 between two MLG layers spaced by a tunneling barrier, as a function of θ and V_b, based on the Bistrizer-MacDonald expression for momentum conserving tunneling between rotated vdW layers. The calculation includes finite temperature, $k_BT = 25meV$, and a finite inverse electron lifetime, $\gamma = \gamma_0 + \gamma_1|\epsilon - \mu|$, where ϵ is the electron energy and μ is the chemical potential. $\gamma_0 = 4meV$, $\gamma_1 = 0.035$ are the experimentally fitted values. The lifetime at low energies corresponds to a coherence length of $l_\phi \approx 150nm$, comparable to the size of some of the inventors' tips, setting a lower bound on the decoherence by electron-phonon and electron-electron interactions at room temperature. The illustrations show the relative alignment of the two Dirac cones at the 'k-resolved onset' and 'nesting' conditions, along the corresponding dashed black and dashed white lines. **g.** panels 1-3 illustrate the relative alignment of the two MLG layers in real space and momentum space, corresponding to points 1-3 in panel d. **h**. Schematic band alignment of the two layers under finite V_b and θ. V_b divides between shifts to the chemical potentials of bottom and top layers, μ_B and μ_T, and the energy band shift (=electrostatic potential shift), ϕ. The Dirac points are shifted in momentum by $k = K_D\theta$, where K_D is the momentum of the Dirac point.

Figs. 9a-i. QTM imaging of the energy bands of twisted bilayer graphene (TBG) **a.** Schematics of the experiment, comprised of an MLG/ bilayer WSe_2/ 2.7° TBG tunnel junction **b.** The mini-Brillouin zone (BZ) of the TBG, with the Dirac cones of the underlying top and bottom layers (represented by blue and red circles) located at two K-points (K_{bot} and K_{top}). Also shown are the Γ_M points of adjacent mini-BZs. When the MLG probe layer is rotated with respect to the TBG, its Dirac cone (purple circle) traces the TBG energy bands along an arc in momentum space (dashed purple), crossing through the K_{bot} and K_{top} points, and very close to the Γ_M points. **c**. Theoretical energy bands of 2.7° TBG along the dashed purple arc in panel b, calculated using the Bistrizer-

MacDonald model. The "flat" and remote bands are shown in blue and black, respectively. **d**. The second derivative, d^2I/dV^2, measured as a function of θ and V_b at $T = 300K$. **e.** Theoretically-calculated d^2I/dV^2 for this junction, as a function of θ and V_b. The theory is based on the Bistrizer-Macdonald expression for momentum conserving tunneling and includes finite temperature, $k_BT = 25meV$, and finite electron lifetime , $\gamma = \gamma_0 + \gamma_1|\epsilon - \mu|$ with $\gamma_0 = 4meV, \gamma_1 = 0.02$. The insets show the relative alignment of the MLG and TBG energy bands at two points in the θ-V_b plane. Left inset: the MLG Dirac point matches in energy and momentum a point on the flat TBG bands. Right inset: the TBG Dirac point matches in energy and momentum a point on the MLG Dirac band. **f**, Tracing of the main features of the measurement in panel d, including features related to the TBG flat (blue) and remote (black) bands, as well as two copies of the MLG Dirac bands (purple). **h**. The TBG energy vs. momentum dispersion (red and grey dots) determined from the measurement in panel d after converting V_b to the energy axis (see text), together with the bands of the BM model (blue). **i**. The magnitude of the tunneling current, I, traced along the features that corresponds to the flat bands (blue curves, panel f) between K_{bot} and K_{top} (gray/red points for the positive/negative bias side). The inventors have normalized the current values by a constant to compare with the theory. Blue line: the theoretically calculated layer polarization of the wavefunction vs. momentum.

Figs. 10a-e. Imaging the effects of applied pressure on the TBG energy bands: **a.** inset: Illustration of the experiment – applying a fixed AFM force across the junction results in GPa-scale pressures at the interface. In the experiment the inventors have kept the pressure on while twisting. **a-c.** Measured d^2I/dV^2 vs. θ and V_b for the junction in Figs. 9a-i, but under applied pressures of P=0.01, P=0.4 and P=0.68 GPa. $T = 300K$. **d**. Evolution of the TBG energy bands with P. In this figure the inventors have traced features that reflect the flat and remote bands as a function of pressure (see key). For every pressure, the inventors have plotted points that were obtained from tracing the relevant feature ('onset' feature for the flat bands, zero dI^2/dV^2 contour for the remote bands). Visibly, with increasing P, the flat bands gradually shrink toward zero V_b while the remote bands shift to higher V_b (arrows), consistent with a pressure controlled anti-crossing. **e**. The bandwidth at the M point of the TBG "flat" energy bands vs. P (red dots), determined from linecuts at $\theta = 0°$. The inventors have converted V_b to the energy from

the simultaneously measured MLG Dirac bands (curved-X on the right side in panels a-c, see Supp. Info S8). Dashed line is a linear fit to the data. At the highest applied pressure (0.68 GPa), the bandwidth shrinks by ~17%.

Supplementary Information (also called "Supp. Info" before):

S1. Fabrication of vdW-device-on-tip

S2. Fabrication of the flat devices

S3. Configuring a commercial AFM for QTM experiments

S4. Calculation of momentum resolved tunneling in a QTM junction.

S4.1. Solving the electrostatics of the QTM junction self-consistently

S4.2 Momentum-resolved tunneling current calculation

S4.3 Band structure of TBG based on Bistrizer-MacDonald model

S4.4 Nordheim-Fowler Contribution and WSe2 barrier breakdown

S5. Understanding MLG-MLG momentum resolved tunneling experiments

S5.1 Momentum-resolved onset condition

S5.2 Nesting condition

S6. Additional experiments: back-gate dependence of MLG-MLG k-resolved tunneling

S7. Electron lifetime in MLG-MLG k-resolved tunneling experiment

S8. Understanding MLG-TBG momentum resolved tunneling experiments

S8.1 First Toy Model – tracing energy bands with a Dirac cone.

S8.2 Second toy model - explaining the k-resolved 'onset' features

S8.3 Temperature dependence of 'onset' and 'Dirac matching' features

S8.4 Comparing the second toy model with the experiment

S8.5 The full calculation – origin of the features in the MLG-TBG k-resolved tunneling

S1. Fabrication of vdW-device-on-tip

To fabricate the vdW-device-on-tips, the inventors have started with commercial tipless AFM cantilevers with a nominal spring constant of K=40 [N/m], length L=232 [μm], width W=37[μm] and thickness T =7[μm]. The inventors have coated the bottom side of the cantilevers with 4/100 nm Cr/Au using an e-beam evaporator. This coating serves as the electrical connection for the active vdW layer and the buried graphite, such that they are at the same electrical potential. Next, the inventors have deposited

a ~ 1.2-1.6 um tall platinum (Pt) pyramid with a ~ 2 um square base using focused ion beam (FIB) deposition (Figs. 11a-c). The nominal size of the pyramids' apex is ~ 50nm.

To assemble the vdW-device-on-tip, the inventors have used the polymer membrane transfer technique1. Briefly, the inventors have spin-coated polypropylene carbonate (PPC) onto a Si/(90nm) SiO2 wafer, followed by exfoliating graphene/hBN crystals. The inventors then have cut a window into a piece of adhesive tape and use it to pick up the PPC film with the target crystal. The crystal is then aligned and transferred on top of the platinum pyramid, followed by melting (~ 120 °C) and washing-off (acetone) of the PPC film to leave behind the vdW crystal. The inventors have assembled the vdW heterostructure by successive transferring and cleaning of each layer. For example, for the experiments done in this Additional Description and Supplementary Information where the active vdW layer on the tip is monolayer graphene, the inventors have started by transferring a graphite flake, ~ 20-40 nm thick, on top of the Pt pyramid, followed by an insulating hBN flake, ~ 20-40 nm. These two layers act as an atomically flat mechanical support for the active vdW layer (monolayer graphene), which is transferred at the last step. The thicker underlayers also define the shape of the plateau obtained at the tip apex. By varying the thickness of these layers, it is possible to obtain plateaus of variable sizes in the range of 50 nm to 1μm.

Figures 11a-f: QTM tip characterization. **a**. SEM image of FIB deposited Pt pyramid on a tipless AFM cantilever **b**. Top view of Pt pyramid **c**. Cross-section of a Pt pyramid cut using local FIB cutting **d**. Optical image of an MLG/hBN/graphite vdW heterostructure on top of a pyramid **e**. AFM topography of vdW heterostructure in panel d. **f**. A linecut from the AFM topography of the vdW tent (red, taken along the dashed red line in panel e) overlayed with a schematic drawing of the Pt pyramid to scale. The top part of the pyramid is smaller than the plateau formed at the top part of the vdW tent.

S2. Fabrication of the flat devices

In this Additional Description with Supplementary Information, the inventors have performed two types of experiments: In-situ twistronics experiments, in which two MLG layers are brought into direct contact (without an insulating barrier in between) and the conductance of the combined system is measured as a function of the twist angle (Fig. 7h), and momentum resolved tunneling, in which the inventors have put a WSe_2 barrier between the MLG probe and the system (MLG or TBG). Here, rotation is used to

scan the momentum axis. For the former, the devices consist of MLG placed on top of an hBN substrate and a graphite gate (Fig. 12b). For the latter, the inventors have used MLG or TBG on top of hBN and graphite, but now have capped it from the top with 2-3 layer WSe_2 (Figs. 12c, d). All inventors' devices have been assembled using the standard dry transfer technique. Briefly, a polypropylene carbonate (PPC) coated polydimethylsiloxane (PDMS) is used to pick up the hBN, MLG (or TBG created using laser cut and stack method), and WSe_2 layers. The inventors have then flipped the stacks by depositing them onto a PMMA-coated PDMS, followed by placing them on the bottom graphite gate. The final heterostructure has been transferred on a ~100um wide and ~80um tall Si/SiO_2 pillar, with pre-pattered gold contacts reaching close to its edge (Fig. 12a). The reason for placing the stack on a pillar rather than on a flat Si/SiO_2 wafer is that this provides mechanical and geometrical flexibility for the tip rotation with respect to the sample, preventing them from touching each other at any point other than at the tip's apex. Next, the inventors have created the electrical contacts by transferring thin (~10nm) flakes of graphite to bridge the pre-patterned contacts and the MLG or TBG. Figs. 12b,c,d show the three variants of heterostructures used in the main text (MLG without tunnel barrier, MLG with tunnel barrier, TBG with tunnel barrier). After assembly, the heterostructures are cleaned by scanning them with an AFM in contact mode to remove polymer residues.

Figures 12a-d: QTM flat side substrate and devices. **a.** SEM image of a Si/SiO_2 pillar with pre-patterned gold contacts. **b.** Optical image of an MLG/hBN/graphite sample used for in-situ twistronics experiments (Fig. 7h). **c.** Optical image of a WSe_2/MLG/hBN/graphite sample used for momentum resolved MLG-MLG tunneling experiments (Figs. 8a-h). **d.** Optical image of a WSe_2/TBG/hBN sample used for momentum resolved MLG-TBG tunneling experiments (Figs. 9a-i and 10a-e).

S3. Configuring a commercial AFM for QTM experiments

The inventors' QTM setup used in some experiments following the example of Figs. 13a-13c above has included two parts (1) A custom-built rotating stage housing the bottom devices (2) A commercial atomic force microscope (Bruker Icon) for performing the AFM operations (Force feedback and lateral positioning). Hence, this section further exemplifies various options for configuration of the AFM (some of which are mentioned also in the claims below).

The custom-built rotating stage comprises (from bottom to top): a goniometer, piezoelectric rotator (attocube), X and Y piezoelectric nanopositioners (attocube) and a sample holder with multiple electrical contacts (Fig. 13c). The goniometer compensates for the built-in angular tilt mismatch between the tip and sample sides in commercial AFMs (~12 degrees in our AFM) and reduces it to ~1 degree. The piezoelectric rotator has an optical encoder allowing for closed-loop angular control with ~1 milli-degree precision. The two linear nanopositioners, mounted on top of the piezoelectric rotator, position the device's point-of-interest in the center of rotation. This custom stage is attached using a rigid frame to an existing AFM stage (because of height limitations, the inventors had to connect it on a side facet of the AFM stage). This adapter has allowed the inventors to use the integrated optics and all standard AFM operations. The AFM has enabled inventors to bring the two vdW surfaces (in the tip and the sample) into contact. Additionally, inventors have used the active force feedback to maintain a constant force during rotation and measurement with a sub-nano-Newton precision. With this QTM setup, the inventors have employed two modalities for the rotation measurements. (1) Continuous contact: Here, the inventors have brought the tip and sample together and rotated whilst maintaining the two surfaces in contact throughout the entire experiment. (2) "Woodpecker": Here, for every point in the measurement as a function of rotation angle, the inventors have brought the tip into contact with the sample, performed the measurement, disengaged, then rotated by a small angle, and then repeated this sequence to get the full measurement. It should be noted that the inventors have obtained almost identical results from both modalities, and both have been highly reproducible.

Figures 13a-c: Room-temperature QTM measurement setup **a.** Custom-built rotator stage integrated into the side of a commercial AFM stage. **b**. Side view of the rotator stage facing the AFM scanner and optics. **c**. The components of the custom-built rotating stage.

S4. Calculation of momentum resolved tunneling in a QTM junction.

In this section the model is presented used by inventors for calculating the theory panels in Figs. 8a-h and 9a-i. In addition to the parameters that are scanned in the experiment that are shown in the main text – the twist angle, θ, and bias, V_b, the inventors also have included in the model the effect of back gate voltage, V_{BG}, such that it also describes the experiments at finite gate voltages shown in section S6 below. The tunneling

current is calculated separately for each combination of the parameters θ, V_b, V_{BG}. The inventors first have determined the chemical potential of top and bottom layers and the electrostatic potential shift between them (μ_T, μ_B and ϕ) by solving the electrostatic equations (S4.1, S4.2) self-consistently with the equations-of-state of the individual layers: $\mu_T(n_T)$ and $\mu_B(n_B)$. This is described in section S4.1 below. The inventors then have summed up the momentum-conserving tunneling rates for all states within the energy window opened by the bias, between μ_T and μ_B. This is described in subsection S4.2 below. The equation of state for the TBG is obtained from the Bistrizer-Macdonald continuum model, detailed in section S4.3. Finally, the inventors have added a Norhdeim-Fowler term due to the breakdown of the WSe_2 barrier, described in section S4.4. All expressions include the effects of finite temperature and finite lifetime.

S4.1. Solving the electrostatics of the QTM junction self-consistently

The inventors have described the electrostatics of the QTM tunnel junction by a three-plate-capacitor model. The first two plates are the top and bottom active vdW layers (in the tip and sample), which are separated by a tunnel barrier (2 or 3 layers of WSe_2). The third layer is the graphite back-gate, separated by an hBN spacer from the bottom vdW system. The inventors have derived the two following equations:

$$eV_b = \mu_B - \mu_T - \frac{e^2 n_T}{C_g}, \tag{S4.1}$$

$$eV_{BG} = \mu_B + \frac{e^2(n_B + n_T)}{C_{BG}}, \tag{S4.2}$$

where V_b is the applied bias between the top and bottom layer, V_{BG} is the back gate voltage with respect to the bottom layer, and μ_B, n_B, μ_T and n_T are the chemical potential and carrier densities of the bottom and top layer respectively. The geometric capacitance per unit area between top and bottom layers, C_g, and between the back-gate and bottom layer, C_{BG}, are given by:

$$C_g = \frac{\varepsilon_{WSe_2}\varepsilon_0}{d_{WSe_2}} \tag{S4.3}$$

$$C_{BG} = \frac{\varepsilon_{BN}\varepsilon_0}{d_{BN}} \tag{S4.4}$$

where d_{WS_2} is the barrier thickness (taken to be $0.58nm$ per monolayer of WSe_2), d_{BN} is the hBN thickness ($70nm$ in the MLG-MLG experiment) in Figs. 8a-h, and $\varepsilon_{WS_2} \approx 4.63, \varepsilon_{BN} \approx 3.2$ are taken to be the corresponding dielectric constants. For

MLG, the dependence of carrier density on chemical potential is given by $n_{Gr} = sign(\mu_{Gr})\frac{\mu_{Gr}^2}{\pi\hbar^2 v_F^2}$, where v_F is the Fermi velocity. For TBG, $n_{TBG}(\mu_{TBG})$ is calculated numerically from the Bistritzer-MacDonald continuum model (section S4 below). We solve together the above equations for μ_B, μ_T and ϕ, self-consistently. Due to the low carrier density of graphene, the quantum capacitance of the QTM junction is generally of a similar order of magnitude as its geometric capacitance. Consequently, the applied bias changes the chemical potentials of the layers as well as the electrostatic potential between them, $\phi = V_b - (\mu_B - \mu_T)$. In Fig. 14 the inventors have plotted the dependence of ϕ, μ_B and μ_T vs. V_b calculated for the parameters of the MLG-MLG experiment in Figs. 8a-8h in the main text. The inventors have been able to see that in this experiment, a change of V_b indeed leads to a same order of magnitude of change in all these quantities. It can also be seen that $\mu_B = -\mu_T$ due to the assumption of overall charge neutrality, which describes well the experiment in Figs. 8a-8h with $V_{BG} = 0$. As explained in section S5, experimentally, it is possible to directly determine the dependence $\phi(V_b)$ from the nesting line in Fig. 8c. Specifically, the inventors have seen that the nesting feature in Figs. 8c, f fits well the experiment if we take $C_g = 2.35\mu F/cm^2$, consistent with thickness and dielectric constant values mentioned above.

Figure 14. The bias dependence of top/bottom chemical potential $\mu_{T/B}$ and electrostatic potential ϕ for MLG-MLG tunneling junction.

S4.2 Momentum-resolved tunneling current calculation

After solving the electrostatics and obtaining the chemical potential and band alignment between top and bottom layers, the inventors have proceeded to calculate the tunneling current. The theoretical model is based on the Bistritzer-MacDonald expression for momentum resolved tunneling between two layers. The model assumes that the tunneling is well described by Fermi's golden rule, namely, that a carrier tunnels coherently only once across the junction and not multiple times back and forth. This assumption is valid for all the experiments in the Additional Description with Supplementary Information that involve a tunneling barrier between the two vdW layers and is implied from the fact that the resistance of the tunnel junction is much larger that the resistance along the vdW layers themselves. With these approximations, the tunneling current is given by:

$$I = \frac{e g_s}{2\pi} \int dE \left(f_B(E) - f_T(E+\phi) \right) \times \sum_{\boldsymbol{k_T}, \boldsymbol{k_B}} \left| T^{\alpha\beta}_{\boldsymbol{k_T} \boldsymbol{k'_B}} \right|^2 A_B(\boldsymbol{k'_B}, E) A_T(\boldsymbol{k_T}, E+\phi) \quad \text{(S4.5)}$$

Here $g_s = 2$ accounts for the spin degeneracy. The functions $f_B(E)$ and $f_T(E+\phi)$ are the Fermi-Dirac distribution functions of the bottom and top layers, while ϕ is the electrostatic potential that shifts the relative position of energy bands. $T^{\alpha\beta}_{\boldsymbol{k_T} \boldsymbol{k'_B}}$ is the tunneling matrix element between a state with momentum $\boldsymbol{k_T}$ on the top layer to one with momentum $\boldsymbol{k'_B}$ in the rotated Brillouin zone of bottom layer. The functions A_B and A_T are the spectral functions for the bottom and top layers: $A_T(E, \boldsymbol{k_T}) = \frac{2\gamma_T}{(E - \epsilon_T(\boldsymbol{k}))^2 + \gamma_T^2}$ where $\epsilon_T(\boldsymbol{k})$ is the energy bands of the top layer. γ_T is the corresponding inverse electron lifetime (the inventors elaborate on this lifetime in section S7). Similar formula applies to the bottom layer.

Eq. (S4.5) requires three conditions to be met for a tunneling event to be allowed. The Pauli principle require the tunneling electron to originate from a full state and arrive to an empty state. This is imposed by the difference between the two Fermi functions. Energy conservation requires the energy difference between the state of origin and the state of destination to differ by ϕ. This is encoded in the energy arguments of the Fermi functions and the spectral functions. And momentum conservation requires the states of origin and destination to have the same momentum. These three requirements are typically met by a curve in momentum space, whose characteristics are determined by μ_b, μ_t, ϕ and, most importantly, by the energy spectra of the two layers. The contribution of the states along that curve is determined by the density of states and by the value of the tunneling matrix element at that momentum.

Following Bistritzer-MacDonald, the tunneling matrix element is given by:

$$T^{\alpha\beta}_{\boldsymbol{k_T} \boldsymbol{k'_B}} = \frac{1}{\Omega_0} \sum_{s,s'} \sum_{\boldsymbol{G_T}, \boldsymbol{G_B}} t_{\boldsymbol{k'_B} + \boldsymbol{G_B}} \left\langle u_{\boldsymbol{k_T}, s} \middle| T_{\boldsymbol{G_T}, \boldsymbol{G_B}} \middle| u_{\boldsymbol{k'_B}, s'} \right\rangle \delta_{\boldsymbol{k_T} + \boldsymbol{G_T}, \boldsymbol{k'_B} + \boldsymbol{G_B}} \quad \text{(S4.6)}$$

where $|u_{\boldsymbol{k_T}, s}\rangle$ and $\left| u_{\boldsymbol{k'_B}, s'} \right\rangle$ are the wavefunctions on the top and bottom layers, s and s' are the band indices, primed wave vectors are rotated with the twist angle, $\boldsymbol{G_T}, \boldsymbol{G_B}$ are reciprocal lattice vectors of the top and bottom layers, α, β are sublattice indices, and $t_{\boldsymbol{k'_B} + \boldsymbol{G_B}}$ is the Fourier transform of the finite-range interlayer hopping amplitude (discussed below). In a matrix form in the sublattice basis the tunneling matrix element is given by:

$$T_{G_1,G_2} = \begin{pmatrix} e^{iG_T\tau_t^A - iG_B\tau_b^A} & e^{iG_T\tau_t^A - iG_B\tau_b^B} \\ e^{iG_T\tau_t^B - iG_B\tau_b^A} & e^{iG_T\tau_t^B - iG_B\tau_b^B} \end{pmatrix} e^{iG_T\cdot d_T - iG_B\cdot d_B} \quad \text{(S4.7)}$$

Here $\boldsymbol{\tau}_t^A$ and $\boldsymbol{\tau}_t^B$ are the sublattice positions of atoms A and B within the unit cell of the top layer; $\boldsymbol{d_T}$ is the lateral displacement vectors for these two layers. The BM model assumes that the tunneling amplitude $t_{\boldsymbol{k}_B'+\boldsymbol{G}_B}$ decays exponentially with the absolute value of momentum measured with respect to the origin in momentum space. Thus, the inventors have considered tunneling events within the first Brillouin zone and approximate $t_{\boldsymbol{k}_B'+\boldsymbol{G}_B} \approx t_0$, which is independent of momentum. Consequently, in the summation of $\boldsymbol{G_T}$ and $\boldsymbol{G_B}$ reciprocal lattice vectors to obtain $T_{\boldsymbol{G_T},\boldsymbol{G_B}}$ only three processes are relevant:

$$T_1 = \begin{pmatrix} 1 & 1 \\ 1 & 1 \end{pmatrix} e^{iG_T\cdot d_T - iG_B\cdot d_B} \quad \text{(S4.8)}$$

$$T_2 = \begin{pmatrix} 1 & e^{+i\frac{2\pi}{3}} \\ e^{-i\frac{2\pi}{3}} & 1 \end{pmatrix} e^{iG_T\cdot d_T - iG_B\cdot d_B} \quad \text{(S4.9)}$$

$$T_3 = \begin{pmatrix} 1 & e^{-i\frac{2\pi}{3}} \\ e^{+i\frac{2\pi}{3}} & 1 \end{pmatrix} e^{iG_1\cdot d_T - iG_2\cdot d_B} \quad \text{(S4.10)}$$

In addition, the tunneling amplitude t_0 is affected by the energy of tunneling electrons and the tunneling barrier shape $V(z)$. This is described by the WKB approximation:

$$V(z) = \Delta_c - \frac{|\phi|}{d} z \quad \text{(S4.11)}$$

$$t_0 = \exp\left\{-\frac{1}{\hbar}\int_0^d \left(2m^*(V(z)-E)\right)^{\frac{1}{2}} dz\right\}$$
$$= \exp\left\{-\frac{1}{\hbar}\frac{2d}{3|\phi|}(2m^*)^{\frac{1}{2}}\left((\Delta_c - E)^{\frac{3}{2}} - (\Delta_c - E - |\phi|)^{\frac{3}{2}}\right)\right\} \quad \text{(S4.12)}$$

Δ_c is the distance from the Dirac point to the conductance band edge of WSe_2 relative to the graphene. E is the energy of the tunneling electron. d is the barrier width and m^* is the effective mass in the z direction of WSe_2, where the inventors have assumed a parabolic dispersion. The inventors have considered here only the conduction and not the valence band edge since it is significantly closer in energy to the Dirac point. The inventors have also ignored the in-plane momentum dependence of Δ_c.

S4.3 Band structure of TBG based on Bistrizer-MacDonald model

The inventors have used the continuum model to calculate the band structure of TBG. For each graphene layer, the lattice vectors are $\boldsymbol{a_1} = \sqrt{3}a_0\left(\frac{1}{2},\frac{\sqrt{3}}{2}\right), \boldsymbol{a_2} = \sqrt{3}a_0\left(-\frac{1}{2},\frac{\sqrt{3}}{2}\right)$. $a_0 = 0.142nm$ is the carbon-carbon bond length and the sublattice vectors A, B are $\boldsymbol{\delta_A} = a_0(0,0), \boldsymbol{\delta_B} = a_0(0,1)$. The Hamiltonian is given by

$$H = H_b + H_t + H_{inter} \tag{S4.13}$$

$$H_b = \sum_{q,\xi,\mathrm{s}} a^{\dagger}_{b,s,\xi}(\boldsymbol{q})\xi\hbar v_f \boldsymbol{R}_{+}\boldsymbol{q}\cdot\boldsymbol{\sigma}a_{b,s,\xi}(\boldsymbol{q}) \tag{S4.14}$$

$$H_t = \sum_{q,\xi,\mathrm{s}} a^{\dagger}_{t,s,\xi}(\boldsymbol{q})\xi\hbar v_f \boldsymbol{R}_{-}\boldsymbol{q}\cdot\boldsymbol{\sigma}a_{t,s,\xi}(\boldsymbol{q}) \tag{S4.15}$$

$$H_{inter} = \sum_{\boldsymbol{q},\boldsymbol{q'},\xi,\mathrm{s}} a^{\dagger}_{t,s,\xi}(\boldsymbol{q})(T_{q_b,\xi}(\boldsymbol{q},\boldsymbol{q'}) + T_{q_{tr},\xi}(\boldsymbol{q},\boldsymbol{q'}) + T_{q_{tl},\xi}(\boldsymbol{q},\boldsymbol{q'}))a_{b,s,\xi}(\boldsymbol{q'}) \tag{S4.16}$$

$a^{\dagger}_{b,s,\xi}$ is the electron creation operator for electrons on the bottom layer with sublattice index s and valley index ξ. $\boldsymbol{R}_{\pm}$ is the rotation matrix of top and bottom layer by twist angle $\pm\frac{\theta}{2}$: $\cos\left(\frac{\theta}{2}\right) + i\sigma_y\sin\left(\frac{\theta}{2}\right)$. The interlayer coupling matrix is given by:

$$T_{\boldsymbol{q_b},\xi}(\boldsymbol{q},\boldsymbol{q'}) = \begin{pmatrix} w_{AA} & w_{AB} \\ w_{AB} & w_{AA} \end{pmatrix}\delta_{\boldsymbol{q}-\boldsymbol{q'},\boldsymbol{q_b}} \tag{S4.17}$$

$$T_{\boldsymbol{q_{tl}},\xi}(\boldsymbol{q},\boldsymbol{q'}) = \begin{pmatrix} w_{AA} & w_{AB}e^{-i\xi\frac{2\pi}{3}} \\ w_{AB}e^{+i\xi\frac{2\pi}{3}} & w_{AA} \end{pmatrix}\delta_{\boldsymbol{q}-\boldsymbol{q'},\boldsymbol{q_{tl}}} \tag{S4.18}$$

$$T_{\boldsymbol{q_{tr}},\xi}(\boldsymbol{q},\boldsymbol{q'}) = \begin{pmatrix} w_{AA} & w_{AB}e^{+i\xi\frac{2\pi}{3}} \\ w_{AB}e^{-i\xi\frac{2\pi}{3}} & w_{AA} \end{pmatrix}\delta_{\boldsymbol{q}-\boldsymbol{q'},\boldsymbol{q_{tr}}} \tag{S4.19}$$

where $\boldsymbol{q_b} = \frac{8\pi sin\left(\frac{\theta}{2}\right)}{3\sqrt{3}d}(-1,0), \boldsymbol{q_{tl}} = \frac{8\pi sin\left(\frac{\theta}{2}\right)}{3\sqrt{3}d}\left(-\frac{\sqrt{3}}{2},\frac{1}{2}\right), \boldsymbol{q_{tr}} = \frac{8\pi sin\left(\frac{\theta}{2}\right)}{3\sqrt{3}d}\left(\frac{\sqrt{3}}{2},\frac{1}{2}\right)$, $\boldsymbol{d}$ is the interlayer distance. w_{AA} is smaller than w_{AB} due to the lattice reconstruction in the AA region, and we adopt the value: $w_{AA} = 88meV, w_{AB} = 110meV$.

S4.4 Nordheim-Fowler Contribution and WSe2 barrier breakdown

In the MLG-MLG junction, the tunneling spectrum shows a breakdown of the WSe_2 tunneling barrier. This is modeled within the WKB approximation. At large bias, the bending of the WSe_2 bands is large enough such that electrons can directly tunnel from the graphene into the conduction band states of WSe_2. This is the Nordheim-Fowler field emission regime, described by:

$$t_{WSe_2} = \exp\left\{-\frac{1}{\hbar}\int_0^{d_0}\left(2m^*(V(z)-E)\right)^{\frac{1}{2}}dz\right\} = \exp\left\{-\frac{1}{\hbar}\frac{2d}{3|\phi|}(2m^*)^{\frac{1}{2}}(\Delta_c - E)^{\frac{3}{2}}\right\} \tag{S4.20}$$

$$d_0 = (\Delta_c - E) * \frac{d}{|\phi|} \quad \text{(S4.21)}$$

Assuming that Δ_c is momentum independent, then the tunneling current is also momentum independent, and is given by:

$$I_{WSe_2} = \frac{e g_s}{2\pi} \int_{\Delta_c - |\phi|}^{\infty} dE \; t_{WSe_2}^2 f_{MLG}(E) DOS_{MLG} DOS_{WSe_2} \quad \text{(S4.22)}$$

The inventors have found the values $m^* = 1.07 m_e$ and $\Delta_c = 0.55eV$ fit the experiments, consistent with the values reported in the literature.

S5. Understanding MLG-MLG momentum resolved tunneling experiments

In the MLG-MLG momentum-resolved tunneling experiment the inventors have identified two main features in the measured d^2I/dV^2 vs. V_b, and θ (Fig. 8c): lines of momentum resolved 'onset' condition, appearing along a straight-X feature, and 'nesting' lines, appearing along a curved-X feature. In this section, the inventors have derived the equations that describe these conditions for the case of a charge-neutral system. The experiments in the Additional Description, performed with $V_{BG} = 0V$, are to a very good approximation a charge-neutral system. By comparing these experiments to the formulas derived here, the inventors have extracted the density dependence of the Fermi velocity and electronic compressibility in this system. In the next section the inventors will show additional measurements done with non-zero V_{BG}, and derive the corresponding equations for the general case of a non-charge-neutral system.

In the charge-neutral case, the carrier density of the bottom layer is equal in magnitude and opposite in sign to that in the top layer:

$$n_T = -n_B \quad \text{(S5.1)}$$

Since MLG is electron-hole symmetric to a good approximation in the energy range probed in our experiments, Eq. S5.1 translates to:

$$\mu_T = -\mu_B \equiv \mu \quad \text{(S5.2)}$$

The electrostatic equation that connects the applied bias, chemical potentials in the two layers, and their relative energy band shift (=electrostatic potential, ϕ) reads (illustrated in top panel, Fig. 15):

$$V_b = \phi + 2\mu \quad \text{(S5.3)}$$

Figure 15. Schematic of the charge-neutral MLG-MLG tunneling experiment (Figs. 8a-8h in main text). The main panel shows the analytically derived lines in the $\theta - V_b$

plane, which correspond to the momentum-resolved 'onset' and 'nesting' conditions. Right and left insets show the theoretically calculated energy band alignments at select points along these lines. Top inset shows how the bias divides between the chemical potential of the two layers, $\mu = -\mu_T = \mu_B$, and the relative electrostatic energy shift of the bands, ϕ.

S5.1 Momentum-resolved onset condition

At a given bias voltage, momentum conserving tunneling onsets when the Fermi surface of one layer touches the empty bands of the other layer. For the charge-neutral case, this condition happens simultaneously for the Fermi surfaces of the top and bottom layers (right and left insets, Fig. 15), when:

$$\phi + 2\mu = \pm\hbar v_F K_D \theta \qquad \text{(S5.4)}$$

Combining equations S5.4 and S5.3, the inventors have got a simple relation for the onset condition,

$$V_b = \pm\hbar v_F K_D \theta \qquad \text{(S5.5)}$$

Effectively, this relation is the Dirac equation of graphene, but with energy E and momentum k replaced by V_b and $K_D\theta$, respectively.

This simple relation appears only in the charge neutral case (the general case is discussed below), which is a good approximation for the experiments performed at $V_{BG} = 0V$, allowing the inventors to directly compare them with equation S5.5. In Fig. 16a the inventors have plotted the measured d^2I/dV^2 in the MLG-MLG (reproduced from Fig. 8c) and trace the peaks (dips) that occur at positive (negative) bias at the onset conditions. The points obtained from this tracing, shown by black dots in Fig. 16b, fit well a linear Dirac dispersion (blue) with a Fermi velocity of $v_F = (1.05 \pm 0.02) * 10^6 m/s$, consistent with previous measurements in graphene. In principle, the Fermi velocity in graphene is known to be renormalized by interactions and becomes logarithmically faster as the energy of the electrons approaches the Dirac point. This renormalization depends on the fine structure constant in graphene $\alpha = e^2/\epsilon\hbar v_F$. Since α depends on the dielectric coefficient of the surrounding environment, when graphene is encapsulated in a dielectric material (in our case WSe_2 and hBN at its opposite sides), the value of the fine structure constant is close to one, and the velocity renormalization is rather small, about 10% change in velocity per one decade in energy. The inventors' experiments have had two MLG layers, which screen better than the single MLG. On length scales larger than the separation of the two MLG layers ($\sim 1nm$ in our experiment),

they act as a single layer with double the density of states, effectively dividing the relevant fine structure constant, and the velocity renormalization by another factor of 2. The red curve in Fig. 16b shows the renormalized velocity calculated for our case. Visibly, the effect of renormalization is small, and within the errors in the determination of the onset peaks, both renormalized and un-renormalized expressions for the Fermi velocity fit well.

Figures 16a-b. **a**. Measured $\frac{d^2I}{dV^2}$ from Fig. 8c, where the inventors traced the local maximum (minimum) at positive (negative) bias, along the 'onset' features (black dots). **b**. Plot of the black dots from panel a together with bare Dirac dispersion (Eq. S5.5) with $v_F = 1.05 \cdot 10^6 m/s$ (blue) and Dirac dispersion that is renormalized by interactions.

S5.2 Nesting condition

Nesting between the Dirac bands of the top and bottom layers happens when these bands overlap along a line of the Dirac dispersion. In this situation, a large number of energy-momentum conserving states become available to tunnel between the layers. Unlike the onset condition, the nesting condition is independent of the band filling, and therefore it directly probes the energy dispersion. At a given twist angle θ, the Dirac dispersion of one of the MLG is shifted in momentum by $k = K_D\theta$ relative to the other. Shifting the Dirac bands in energy by

$$\phi = \pm\hbar v_F K_D \theta \tag{S5.6}$$

will bring the two MLG Dirac dispersions into nesting. This condition is similar to the onset condition in equation S5.5, except that here ϕ replaces V_b.

The nesting line in the measurement allows us to read out directly the energy shift between the bands for every V_b. Figure 17a plots the measurement after rescaling the rotation angle axis using equation S5.6. In these new axes the nesting line gives directly $\phi(V_b)$.

Once the dependence $\phi(V_b)$ is determined from the measurement, it is straightforward to obtain from it the geometric capacitance, C_g, and quantum capacitance, C_q, of the system. By differentiating Eq. S5.3 with respect to ϕ, the inventors have obtained,

$$\frac{dV_b}{d\phi} = 1 + 2\frac{d\mu}{dn}\frac{dn}{d\phi} = 1 + 2\frac{C_g}{C_q} \tag{S5.7}$$

which provides a direct relation between the local slope of the nesting line and the ratio of geometric to quantum capacitances. Hence, for system with different geometric

capacitances the nesting line will have a different shape. This is demonstrated in Fig. 17b, which shows the theoretically calculated graphs with increasing value of C_g between the different panels. For the case of a smaller geometric capacitance (left panel, Fig. 17b), the slope of the nesting line approaches 1, as required by Eq. S5.7. In this limit, which corresponds to the case of a thick tunneling barrier, most of the applied bias goes into shifting the bands, and only a small fraction of it goes to increasing the chemical potentials. In the opposite limit (right panel), where the geometric capacitance is large (corresponding to a thin barrier), the bias hardly shifts the energy bands but mostly changes their occupation. The center panel in Fig. 17b has a nesting line that matches closely the dependence observed in the experiment (Fig. 17a). This has allowed the inventors to determine the geometric capacitance in this experiment to be $C_g = 2.35\mu F/cm^2$. The inventors could see that for a typical width of tunneling barriers (2-4 monolayers) and with the typical density of states of MLG, the experiments are generally in an intermediate regime in which the geometric and quantum capacitances are of comparable magnitude. Eq. S5.7 also shows that once C_g is determined, the local slope of the nesting line provides the quantum capacitance of the system. Eq. S5.7 was derived for the symmetric (charge-neutral) case of two MLG layers. In the general case when two systems are different, or they are the same but have different carrier densities, then $2/C_q$ in Eq. S5.7 should be replaced by the in-series sum of the quantum capacitances of the two systems, $1/C_q^T + 1/C_q^B$.

Figures 17a-b. Rescaling rotation angle θ to the electrostatic potential ϕ. **a**. $\frac{d^2I}{dV^2}$ measurement from Fig. 8c with θ axis converted to ϕ using the relation $\phi = \hbar v_F K_D \theta$. After rescaling, the nesting line (yellow extracted from peak fitting) gives directly $\phi(V_b)$. **b**. Calculated $\frac{d^2I}{dV^2}$ spectrum for geometric capacitances $C_g = 0.50, 2.35\ and\ 4.00\ \mu F/cm^2$.

S6. Additional experiments: back-gate dependence of MLG-MLG k-resolved tunneling

In Figs. 8a-h the inventors have showed momentum resolved tunneling experiments between two MLG layers. Here the inventors have presented additional data, showing how these measurements evolve with back gate voltage. **Figures 18a-f-20a-f** show measurements of I, dI/dV and d^2I/dV^2, respectively, vs. θ and V_b, now as a function

of back gate voltage. The top row in each figure shows measurements done at three values of the back-gate voltage, $V_{BG} = -10V, 0V, +10V$. The bottom row shows the corresponding theoretical calculations, based on the BM expression for momentum resolved tunneling between two parallel layers. Whereas the measurement at $V_{BG} = 0V$ is symmetric between positive and negative bias, the measurements at $V_{BG} = -10V, +10V$ are asymmetric in bias. Focusing on the measurements of d^2I/dV^2 (Figs. 20a-f), in which the features are the sharpest, we can see that while for $V_{BG} = 0V$ the crossing point of the curved-X is at zero bias, for finite V_{BG} it shifts to finite bias (positive bias for $V_{BG} = +10V$ and negative bias for $V_{BG} = -10V$). In addition, the symmetric X shape at $V_{BG} = 0V$ evolves into a "bell-shape" that is asymmetric with respect to bias. However, if the inventors flip the bias axis and the sign of the current in the $V_{BG} = -10V$ measurement it becomes almost identical to the measurement at $V_{BG} = +10V$. Namely, the data obeys the following symmetry: $I(\theta, V_b, V_{BG}) = -I(\theta, -V_b, -V_{BG})$ and similarly $d^2I/dV^2(\theta, V_b, V_{BG}) = -d^2I/dV^2(\theta, -V_b, -V_{BG})$.

To interpret the experiments with finite back-gate voltages, the inventors have allowed for the chemical potentials of the two layers to be different and have generalized the analysis to include a finite V_{BG}, following equations S4.1-S4.4. The resulting 'onset' and 'nesting' lines in this more general case are shown in Fig. 21. The inventors have seen that the theory recovers the asymmetric bell-shaped 'nesting' line, observed experimentally. This shape generalizes the functional dependence of ϕ vs. V_b (Eq. S5.7) to now include two unequal inverse quantum capacitances in the layers, which add in series. In addition, the inventors have seen that now each 'onset' line splits in two, since the Fermi surfaces in both layers have a different size and they touch the empty bands in the other layer at different twist angles.

Figs. 22a-b overlays the calculated 'onset' lines on the measured d^2I/dV^2 at $V_{BG} = -10V$, as well as on the corresponding theoretical calculation. Although room temperature smearing has almost eliminated all the detailed structure related to the 'onset' conditions, the inventors still have been able to resolve in the experiment faint peaks that follow the predicted 'onset' lines. Another feature that is clearly visible both in theory and experiment are the horizontal lines (dashed black) along which the d^2I/dV^2 flips sign. Each such line corresponds to one of the MLG layers going across charge neutrality,

namely either $\mu_T = 0$ or $\mu_B = 0$. Overall, the inventors have been able to see that the theory captures most of the details in the experiment rather accurately.

Figures 18a-f: Back-gate voltage dependence of momentum-resolved tunneling current in a MLG - MLG junction **a-c.** Tunneling current, I, measured in the junction in Figs. 8a-8h (MLG/ trilayer WSe_2/MLG) as a function of θ and V_b, for three values of the back-gate voltage $V_{BG} = +10V, 0V, -10V$ respectively. **d-f.** Corresponding theoretical calculations

Figures 19a-f: Back-Gate voltage dependence of dI/dV. The same measurement as in Figs. 18a-f but now showing the (simultaneously measured) conductance, dI/dV. **a-c.** Experiment. **d-f.** Theory.

Figures 20a-f: Back-Gate voltage dependence of d^2I/dV^2. The same measurement as in Figs. 18a-f,19a-f but now showing the second derivative, d^2I/dV^2, obtained by numerically deriving the data in Fig. 19. **a-c.** Experiment. **d-f.** Theory.

Figure 21: Schematic of the MLG-MLG tunneling junction for experiments with a finite back gate voltage. The main panel shows the theoretically derived lines in the $\theta - V_b$ plane, which correspond to the momentum-resolved 'onset' and 'nesting' conditions. Compared to the charge-neutral case, the 'nesting' line becomes "bell-shaped" and asymmetric in bias, and the 'onset' lines splits to four lines. Right and left insets show the theoretically calculated energy band alignments at select points along these lines. Top inset shows how the bias divides between the chemical potential of the two layers, μ_T and μ_B, and the relative electrostatic energy shift of the bands, ϕ.

Figures 22a-b. **a.** Measured and **b.** Calculated d^2I/dV^2 vs. θ and V_b, at $V_{BG} = -10V$ (similar to Figs. 20c,f). The overlaid black dotted lines correspond to the theoretically calculated k-resolved 'onset' conditions, as shown in Fig. 21. Horizontal dashed lines indicate the two biases at which each one of the MLG crosses through charge neutrality ($\mu_B = 0$ or $\mu_T = 0$).

S7. Electron lifetime in MLG-MLG k-resolved tunneling experiment

The dominant mechanism setting the width of the features in the inventors' measurement is thermal smearing. All measurements so far have been performed at room temperature, leading to $k_BT \sim 25meV$ smearing entering via the Fermi-Dirac functions in Eq. S4.5. To quantitatively explain our data, we find that we should also include smaller smearing due to finite electron lifetime. The electron lifetime is encoded in the spectral

functions of the bottom and top layers, $A_B(\epsilon, \boldsymbol{k}) = \frac{2\gamma_B}{(\epsilon - \epsilon_B(\boldsymbol{k}))^2 + \gamma_B^2}$ and $A_T(\epsilon, \boldsymbol{k}) = \frac{2\gamma_T}{(\epsilon - \epsilon_T(\boldsymbol{k}))^2 + \gamma_T^2}$, where $\epsilon_B(\boldsymbol{k})$ and $\epsilon_T(\boldsymbol{k})$ are the energy bands of these layers, and γ_B, γ_T are their corresponding inverse electron lifetimes. Finite lifetime leads to a Lorentzian broadening of the spectral functions, which could be directly observed in the width of the features in the measurements.

Fig. 23 plots the measured I vs. θ at small bias, $V_b = 40mV$, (black line, same as the inset in Fig. 8a in the Additional Description). Compared with theoretical curves broadened by $k_B T = 25meV$ and with various inverse lifetime values, γ_0, we see that the value that best fits the measurement is $\gamma_0 \approx 4meV$. At higher biases (of the order of the Fermi energy) the inventors generally have observed shorter lifetimes. The dependence of the lifetime on energy is expected to be complicated in this energy range. The inventors have found a reasonably good fit to the phenomenological expression used previously, where $\gamma = \gamma_0 + \gamma_1 |\epsilon - \mu|$, with the γ_0 above and $\gamma_1 \approx 0.035$.

The data shown in **Fig. 23** allows for determining the electron lifetime at low bias. Black curve corresponds to the measured tunneling current, I vs. rotation angle θ, at small bias $V_b = 40mV$, for the junction in Figs. 8a-8h (same as he right inset in Fig. 8a). Colored curves in the figure correspond to the theoretically calculated k-resolved tunneling current (see text) with room temperature broadening $k_B T = 25meV$ and various values of inverse electron lifetime, γ_0 (see key).

S8. Understanding MLG-TBG momentum resolved tunneling experiments

In this section, the inventors explain the various features observed in the momentum resolved tunneling experiments between MLG and TBG, shown in Figs. 9a-9b. The inventors first have used a simple toy model to explain the main mechanism leading to the quantitative energy band mapping in their experiment – tracing the bands of the sample with a Dirac point of the probe. As the inventors show, this mechanism directly probes the dispersion of the bands and is insensitive to their filling. The inventors then expand the discussion to include additional momentum-resolved tunneling 'onset' features that appear when the Fermi level of one side (tip/sample) crosses the energy bands of the other side. The inventors end by showing how these features appear in the full momentum resolved calculation, which includes the multitude of energy bands obtained within the BM model of TBG as well as finite temperature effects.

S8.1 First Toy Model – tracing energy bands with a Dirac cone.

Here the inventors show the ability of using a Dirac cone to trace the energy bands of a sample, i.e., a method to read off the samples band structure. The inventors conceive a toy model of a probe layer with a Dirac dispersion scanning a system with arbitrary energy bands. For simplicity, we set the tunneling matrix element to be a momentum-independent constant. The results of the toy model depend on the relative Fermi velocity of the probe and system: $v_{F_{probe}}$ and $v_{F_{syst}}$. Close to the intersection point with the probe's dispersion, the system's band can be linearized with Fermi velocity $v_{F_{syst}}$. The energy offset between the Dirac point of the probe and the system's band is denoted by $\Delta\varepsilon$. This offset can be tuned by changing the bias voltage between the probe and the system. The inventors have considered three situations: 1. $v_{F_{probe}} > v_{F_{syst}}$; 2. $v_{F_{probe}} = v_{F_{syst}}$; 3. $v_{F_{probe}} < v_{F_{syst}}$. The tunneling occurs in an energy window set by the bias voltage, where the states in the system are empty and the states in the probe are full (or vice versa). The inventors denote this energy window by $\varepsilon_1 \leq \varepsilon \leq \varepsilon_2$. For simplicity, the inventors set $T = 0$ and neglect the electron lifetimes (i.e., the inventors treat the electrons as free).

In the case where $v_{F_{probe}} > v_{F_{syst}}$, the intersection between the energy surfaces of the probe and the system is an ellipse. The inventors assume that the entire ellipse is contained within the energy window $[\varepsilon_1, \varepsilon_2]$ where the tunneling takes place. Then, using Eq. (S4.5), we obtain:

$$I \propto |T_{TB}|^2 \frac{|\Delta\varepsilon|}{4\pi v_{F_{probe}}^2} \frac{\left(v_{F_{probe}}/v_{F_{syst}}\right)^3}{\left[\left(v_{F_{probe}}/v_{F_{syst}}\right)^2 - 1\right]^{3/2}}, \qquad (v_{F_{probe}} > v_{F_{syst}}) \qquad \text{(S10.1)}$$

where T_{TB} is the tunneling matrix element. Hence, the current is minimal when the Dirac point coincides the system's dispersion ($|\Delta\varepsilon| \to 0$). At this point, d^2I/dV^2 is strongly peaked. Thus, in this situation, the peak in d^2I/dV^2 can be used to directly read off the system's band structure (see **Figs. 24a, b**). In the limit $v_{F_{probe}} \to v_{F_{sys}}$, the size of the elliptical intersection between the two dispersion diverges, and it extends outside the window $[\varepsilon_1, \varepsilon_2]$. Hence, Eq. (S10.1) is not applicable in this limit.

If $v_{f_{probe}} = v_{f_{syst}}$, the intersection between the energy surfaces is a parabola. The tunneling current is

$$I \propto |T_{TB}|^2 \frac{\sqrt{2}|\Theta(\Delta\varepsilon)\varepsilon_2+\Theta(-\Delta\varepsilon)\varepsilon_1|^{3/2}}{3(2\pi)^2 v_{F_{probe}}^2 |\Delta\varepsilon|^{1/2}}, \ (v_{F_{probe}} = v_{F_{syst}}) \qquad \text{(S10.2)}$$

Interestingly, the current diverges as $|\Delta\varepsilon| \to 0$. This divergence corresponds to the nesting condition in the MLG-MLG tunneling junction. The divergence is regularized by introducing a curvature to the bands, or a finite lifetime of the electrons in the system and the probe.

Finally, for $v_{F_{probe}} < v_{F_{syst}}$, the intersection is a hyperbola. In this case, the singular part of the current at small $|\Delta\varepsilon|$ is

$$I \propto -|T_{TB}|^2 \frac{|\Delta\varepsilon| \ln\left|\frac{\Theta(\Delta\varepsilon)\varepsilon_2+\Theta(-\Delta\varepsilon)\varepsilon_1}{\Delta\varepsilon}\right|}{4\pi v_{f_{probe}}^2} \frac{\left(v_{F_{probe}}/v_{F_{syst}}\right)^3}{\left[1-\left(v_{F_{probe}}/v_{F_{syst}}\right)^2\right]^{3/2}}. \ (v_{F_{probe}} < v_{F_{syst}}) \qquad \text{(S10.3)}$$

I.e., in this case, the current has a maximum at $\Delta\varepsilon = 0$. At this point, d^2I/dV^2 shows a minimum. This is the case for the Dirac point of TBG - with slower Fermi velocity - tracing the MLG dispersion.

S8.2 Second toy model - explaining the k-resolved 'onset' features

In the previous section the inventors have explained the main features in their experiment that visualize the energy bands as resulting from tracing with a Dirac point. In addition to these, the inventors have seen features in the measurement (Figs. 9a-i) that correspond to 'onset' conditions of the momentum resolved tunneling. These occur whenever the Fermi surface of one side (tip/sample) crosses the energy bands of the other side. In this section, the inventors use a more elaborate model that captures these 'onset' features and identifies their origin. The inventors will further show that these 'onset' features are strongly smeared by temperature, whereas the 'Dirac matching' features discussed in the previous subsection are largely insensitive to temperature.

To capture the essential physics, the inventors have used a second toy model that includes Dirac bands that represent the MLG and two parabolic bands, $\epsilon_{k\pm} = \pm(Ak^2 + W/2)$, which mimic the conduction and valence flat TBG bands along the $K_{bot} - M - K_{top}$ trajectory in momentum space. In addition, the model also keeps track of the chemical potentials in both systems. The Dirac and Parabolic bands are shown explicitly in **Fig. 24a**. For simplicity, the inventors have focused only on a relative rotation angle of $\theta = 0°$ between the MLG and TBG and calculate the current and its derivatives as a function of bias. **Figure 24b**, shows I vs. V_b calculated within this model, assuming a low temperature ($k_BT = 1meV$). The corresponding d^2I/dV^2 is

shown in **Fig. 24c**. For the electrostatics, the inventors have assumed a simple linear relation between the chemical potential of the layers and the applied bias, $\mu_T = -0.4V_b$ and $\mu_B = 0.2V_b$, which approximates rather well the full electrostatics of the real MLG-TBG junction.

At small V_b, the current is zero since there are no energy-momentum conserving states in the tunneling energy window (represented by a white window in Fig.24a and insets to Fig. 24b) between the chemical potentials of the two layers (red and blue dashed lines). Then, at a finite V_b ($\sim 0.18V$ for the parameters of Fig. 24b), the current exhibits a sharp step increase, that occurs when the Fermi level of the Dirac band (red dashed) crosses the occupied parabolic energy bands (left inset, Fig. 24b, crossing indicated by the black arrows). This is the 'onset' point where momentum conserving current first becomes available. At this bias, at zero temperature, the current discontinuously jumps to a finite value because a full circle of energy-momentum conserving states shared by the Dirac and parabolic bands becomes abruptly available. In the second derivative, d^2I/dV^2, the step of I shows up as a plus-minus dipole (Fig. 24c). With a further increase of V_b, the Dirac cone shifts down with respect to the parabolic bands and the circle of energy-momentum matched states (now deep below the Fermi energy) shrinks. Consequently, the current decreases linearly with V_b. It reaches a minimum when the Dirac point exactly crosses the parabolic band and the circle shrinks to a single point (center inset, Fig. 24b). In the second derivative, this minimum translates to a peak. This is the 'Dirac matching' condition, discussed in the previous section. Upon a further increase of V_b, the energy-momentum conserving circle of states grows back again, leading to a linear increase of I, until a second onset condition occurs, where the Fermi level in the parabolic bands (dashed blue) crosses the empty Dirac bands (right inset, Fig. 24b). This second onset leads to another step in I and to a second diploe in d^2I/dV^2.

The calculation in **Figs. 24a-c** was performed with a low temperature, such that it would be easy to identify the various features. Before relating the predicted features with the inventors' experiment, the smearing of different features at elevated temperatures is discussed.

Figs. 24a-c: A second toy model, explaining the momentum resolved features. **a.** Schematic band alignment of a toy model comprising of Dirac (red) and parabolic (blue) bands. The Fermi levels in the Dirac and parabolic bands are marked by dashed red and

blue lines, correspondingly. The bias, V_b, gives the distance between these two Fermi energies. Also indicated are the chemical potentials of the top and bottom layers, μ_T and μ_B, and the energy band shift (= the electrostatic potential), ϕ. Darker regions around the Fermi energies represent the thermal smearing due to room temperature. **b**. and **c**. are the calculated I and $\frac{d^2I}{dV^2}$ as a function of V_b at $\theta = 0°$. Three distinct features are marked by dashed lines. Top insets show the calculated relative band alignment between the Dirac and parabolic bands, that correspond to these features. Black arrows represent the energy-momentum matching states at every condition.

S8.3 Temperature dependence of 'onset' and 'Dirac matching' features

Figure 25 shows temperature dependence of tunneling vs. bias in the second toy model; the figures plot the current and its second derivative at θ = 0∘ at two temperatures. The figure shows how the 'onset' and 'Dirac matching' features evolve between low temperature ($k_BT = 1meV$, blue) and room temperature ($k_BT = 25meV$, dashed red). Clearly, the steps in I that correspond to the 'onset' conditions gets smeared with temperature (panel a). The corresponding dipoles in d^2I/dV^2 (panel b) are also smeared. Thus, their amplitude is significantly reduced. In contrast, the d^2I/dV^2 peak that correspond to the 'Dirac matching' condition is hardly affected by the temperature. This highlights the different mechanisms at play – the 'onset' conditions occur when a Fermi energy crosses an available band. Temperature broadens the Fermi-Dirac distribution around the Fermi energy, which leads to smearing of these features. In contrast, the 'Dirac matching' feature occurs deep inside the bias window. If the temperature is smaller than the distance between the Dirac point and the edges of the bias window, then these features would be unaffected by the thermal smearing. Instead, their width represents the intrinsic electronic lifetime.

S8.4 Comparing the second toy model with the experiment

The inventors have compared the second toy model with the measurements. **Fig. 26a** shows a zoom-in of the central part of one of the flat bands in the measurement in Fig. 9d, where it exhibits a parabolic shape. The inventors could see that a single band generates three curved features in d^2I/dV^2, marked A, B, and C in the figure, corresponding to a maximum/minimum/maximum (red/blue/red) of d^2I/dV^2. The toy model, calculated with $k_BT = 25meV$ (**Fig. 26b**) qualitatively reproduces all three features. **Figs. 26c, d** show I vs. V_b along a line cut at $\theta = 0°$ (black dashed line in

panels a, b) in the measurement and model, respectively. **Figs. 26e,f** plot the corresponding d^2I/dV^2 traces. By comparing this cut to **Fig. 25** the inventors could see that the pair of A/B (maximum/minimum) features correspond to the d^2I/dV^2 dipole that results from the first 'onset', and that feature C (maximum) is the peak that corresponds to the 'Dirac matching'. To see this more directly, the inventors have plotted in **Fig. 26g** the band alignment in the model for the transition point between the A and B features, and for the peak of the C feature. Indeed, the inventors could see that the assignment fits well these two conditions, even in this higher temperature calculation. In the experiment (**Fig. 26e**), the inventors see the same features, at similar biases, although the relative amplitudes are somewhat different. The inventors also note that in the experiment these features are sitting on top of a background current that increases with V_b. This background corresponds to thermally activated current above the WSe_2 barrier, which is present in the experiment and not in the simple toy model.

Figures 26a-g. **a**. Measured d^2I/dV^2 vs θ and V_b from Fig. 9d, zoomed-in around features originating from the TBG flat bands. Three features are marked by A, B and C (red, blue, red). **b**. Corresponding calculation based on the toy model in section S8.2 with $k_BT = 25meV$. **c**. I vs. V_b along a line cut at $\theta = 0°$ in the measurement (dashed black line in panel a). **d.** Similar linecut through the model calculation in panel b. **e**. and **f**. corresponding second derivative, d^2I/dV^2, vs. V_b traces. **g**. The band alignments that correspond to the V_b points marked in panel f. Red/blue bands correspond to the Dirac and parabolic bands. Red/blue dashed lines are the Fermi energies in these two systems. The gray area marks the energies outside the bias window.

S8.5 The full calculation – origin of the features in the MLG-TBG k-resolved tunneling

Having identified the main features in our experiments using toy models, the inventors have arrived to showing how these features appear in the full calculation (Fig. 9e), which includes the multiple TBG bands (flat and remote) of the BM continuum model.

In **Fig. 27a** the inventors have reproduced the theory plot of Fig. 9e, showing d^2I/dV^2 as a function of θ and V_b, and highlight special points at which we show the calculated band alignment. **Fig. 27b** plots the same points over a traced-out version of the measurements. In the rest of the panels, the inventors have presented the calculated

band alignments along each of the traced features. In panel c the inventors have shown five points along the flat band feature (blue). The theory-derived band alignments at these points are shown in the right panels. The inventors have clearly seen that along this feature the Dirac point of the MLG traces the TBG flat band. In panel d, the inventors have followed the band alignment along the traced-out purple feature. Notably, here the right Dirac cone of the TBG flat bands is tracing the bands of the MLG. In panel e, the inventors have shown points along the 'remote bands' features. The band alignment diagrams show that this feature appears when the MLG Dirac point is tracing these bands, similar to the mechanism through which the flat bands are traced.

The inventors have concluded that the MLG Dirac feature that appears prominently in their measurement (indicated by purple lines in **Fig. 27b**) allows to convert the applied V_b to the actual energy shift between the bands. The procedure is similar to that in the MLG-MLG experiment: given that the v_F in their MLG probe is known, they have been able to relate the angle along which the feature appears to the energy shift between the bands by $\phi = \hbar v_F K_D \theta$ (inventors have used here one of the two Dirac features observed in the measurement, and measure θ from its crossing point). The $\phi(V_b)$ extracted in this way is shown in **Fig. 28** (red dots) and compared to the theoretically calculated curve based on the inverse compressibility of TBG and MLG, which add up in series in the electrostatic solution. The inventors have found that these agree well. This method of using the MLG probe dispersion, which inherently appears in the inventors' measurements, allows to convert the V_b axis into an energy shift and plot directly the $E(k)$ relation of the imaged bands. The inventors have used this in Figs. 9a-i and 10a-e to directly compare the bands with the theoretical predictions.

Figures 27a-e. **a**. Calculated d^2I/dV^2 vs. θ and V_b similar to Fig. 9e, but with overlayed points for which we present the band alignment. **b**. tracing of the major features in panel a, which include the TBG flat bands (blue), MLG Dirac bands (purple) and TBG remote bands (black) **c.** band alignment for five points along the TBG flat bands features. **d.** Same, for five points along the MLG Dirac features **e**. Same, for three points along the remote band feature. In the individual panes the MLG and TBG bands are plotted by red and blue, their Fermi energies are plotted by correspondingly colored dashed line, and the greyed-out area shows the region that is outside the bias window.

Figure 28. The energy band shift, ϕ, as a function of V_b, (red dots) extracted from the feature that follows the MLG bands in the MLG-TBG measurement in Fig. 9d. The black line is the theoretically calculated $\phi(V_b)$ using the inverse compressibilities of MLG and TBG and a geometric capacitance $C_g = 1.90\mu F/cm^2$.

Experiments With a Probe of a Smaller Lateral Size

Additionally, the inventors have checked that their experimental techniques are useful also for providing probes with a vdW heterostructure of support and active layers and forming a plateau of at least one size being about 10 nm at the apex. While such a size would not lead to a momentum resolution achievable with probes with plateaus of more than 50 nm size, they are useful for measuring local parameters of the electronic structure, and have a higher chance not to suffer from debris than those CAFM tips which have to be coated with harder tip materials or coatings like conductive diamond-like coatings or platinum silicide mentio.

The inventors have fabricated such a probe and measured a current through it to a conductive sample coated with a defect-assisted tunnel layer having multiple atomic defects. Thus, the probe was moved along the surface of the sample and was imaged multiple times by these defects. Such an image of the whole area of sample is presented in **Fig. 29**: it includes multiple images of the elongated tip of about 10 nm size in one direction and 100 nm a perpendicular direction.

The drawings and the examples of the present disclosure present just some examples of the invented systems and methods. Many variations are possible within the scope of the disclosure, and they can provide ground to further claims than listed below.

CLAIMS:

1. A probe for mechanically contacting a sample and for use in conducting electrical measurements on the sample, the probe comprising:

a tip having a core with an apex, where the apex is covered by a layer arrangement comprising at least a support layer of a vdW material and an active layer presenting a 2D material of not more than 10 monolayers coupled by vdW forces, the active layer being placed on the support layer at said apex and being thereby further away from the core than the support layer at said apex, wherein

an outer layer of said layer arrangement is an exposed layer,

the layer arrangement is configured to form, under a pressure against a planar surface, a mechanical contact of a contact area comprising a square with a side of 10 nm or more,

the layer arrangement is configured to conduct an electric current substantially in a lateral dimension and through the active layer.

2. The probe of claim 1, wherein said exposed layer of the layer arrangement is the active layer.

3. The probe of claim 1, wherein:

the layer arrangement further comprises a tunnel barrier layer which is placed on the active layer and is said exposed layer and is thereby configured to present a flow path for a tunneling current between the sample and the 2D material,

the layer arrangement is configured to conduct the electric current, besides via said tunneling, substantially in the lateral dimension and through the active layer.

4. The probe of claim 1, wherein:

the layer arrangement on said apex further comprises a defect-assisted tunneling layer which is placed on the active layer and is said exposed layer and comprises at least one atomic defect which presents a flow path for a tunneling current between the sample and the 2D material,

the layer arrangement is configured to conduct the electric current, besides via tunneling via the at least one atomic defect in the defect-assisted tunneling layer, substantially in the lateral dimension and through the active layer.

5. The probe of claim 4, wherein the defect-assisted tunneling layer comprises at least two said atomic defects, and wherein each of these atomic defects has a peak of tunneling conductance at a certain unique voltage between a point on the active layer closest to this defect and a point on the exposed surface of the defect-assisted tunneling layer closest to this defect.

6. The probe of any of preceding claims, wherein said contact area has a diameter of at least: 20 nm, or 50 nm, or 100 nm, or 150 nm, or 1 μm in one direction, and any diameter of at least: 20 nm, or 50 nm, or 100 nm, or 150 nm, or 1 μm in a perpendicular direction.

7. The probe of any of claims 1 to 5, wherein the contact area has at least: 20 nm, or 50 nm, or 100 nm, or 150 nm, or 1 μm diameter in one direction, and a diameter not exceeding: 30 nm or 20 nm in a perpendicular direction.

8. The probe of any of claims 4 or 5, wherein the contact area has a diameter of the contact area limited to: 40 nm, or 30 nm, or 25 nm, or 20 nm.

9. The probe of any of preceding claims, wherein the layer arrangement further comprises a gate electrode layer covering the apex and being closer to the core than the support layer.

10. The probe of any of preceding claims, wherein the exposed layer has a plateau comprising said square at the apex.

11. The probe of any of claims 1 to 9, wherein the exposed layer has at the apex a convex surface region configured to flex under the pressure into a plateau comprising said square.

12. The probe of any of preceding claims comprising an at least one contact electrode connected to the active layer.

13. The probe of any of preceding claims, comprising a substrate from which the core protrudes.

14. The probe of claim 13, wherein the substrate is an AFM or STM cantilever.

15. The probe of claim 13 or 14, wherein an edge of the layer arrangement, where at least the support layer and the active layer remain beyond the apex, extends to the substrate.

16. The probe of claim 15, wherein the layer arrangement has at least three folds with directions from the apex towards the substrate.

17. The probe of any of preceding claims, wherein there is a space filled with vacuum, or a gas, or a fluidic matter between a section of the layer arrangement and the core.

18. The probe of any of preceding claims, wherein a length of the core is larger than 1 μm and/or smaller than 10 mm.

19. The probe of any of preceding claims, wherein the pressure does not exceed 30 GPa, or 10 GPa, or 1 GPa.

20. A Scanning Probe Microscopy (SPM) apparatus, comprising the probe of any of preceding claims, and being configured and operable as one of the following: an Atomic Force Microscope (AFM), a Conductive AFM (CAFM), or a Scanning Tunneling Microscopy (STM).

21. The SPM apparatus of claim 20, being configured as the AFM or STM and comprising:

a stage configured to carry a sample,

a head configured to hold an AFM cantilever or an STM probe to probe a sample carried by the stage,

a motor configured and operable to perform lateral rotation of the stage with respect to the head, and

a control unit configured and operable to control the lateral rotation of the stage with respect to the head to provide a desired orientation alignment between them.

22. The SPM apparatus of claim 21, wherein the motor and the control unit are configured and operable to provide the lateral rotation of the stage with respect to the head with an accuracy better than 5 degrees, or 1 degree, or 0.1 degree, or 0.01 degree.

23. The SPM apparatus of claim 21 or 22, wherein the control unit comprises an output unit configured to send an at least one control signal, being an electronic or electromagnetic signal, to the motor.

24. The SPM apparatus of any one of claims 21 to 23, further comprising:

a rotation angle measurement unit configured to measure a rotation angle by which the stage has been laterally rotated with respect to the head, and send a signal indicative thereof to the control unit;

wherein the control unit is configured to control the lateral rotation based on said signal to implement the desired orientation alignment.

25. The SPM apparatus of any one of claims 21 to 24 further comprising at least one tilting unit configured to change a tilt of at least one of the stage and the head to provide alignment between an exposed surface of the sample and one of the AFM cantilever and the STM probe.

26. The SPM apparatus of any one of claims 20 to 25, further comprising:

a first contact electrode configured to connect to the sample,

a second contact electrode configured to connect to a contact electrode of the AFM cantilever or the STM probe,

27. The SPM apparatus of claim 26, further comprising:

a voltage source configured to apply an electrical voltage between the first electrode and the second electrode, and

a current measurement unit configured to measure a resulting electrical current.

28. The SPM apparatus of claim 27 wherein the voltage source is tunable, and the SPM apparatus further comprises a voltage source control unit configured to vary electrical voltage to scan an electronic structure of the sample.

29. The SPM apparatus of any of claims 21 to 28, having one of the following configurations: (i) the stage configured to carry the sample is mounted on an AFM stage or an STM stage; (ii) the stage configured to carry the sample is configured for mounting into an AFM stage or an STM stage, (iii) the stage configured to carry the sample is configured for mounting to a side of an AFM stage or an STM stage, and (iv) the stage configured to carry the sample is formed integrally with an AFM stage or an STM stage.

30. The SPM apparatus of any one of claims 21 to 29, further comprising a positioning unit comprising at least one nanopositioner configured to shift the stage along a straight line.

31. A method of measurement of an electronic structure of a sample, comprising

pressing the probe of any one of claims 1 to 19 to the sample;

applying a voltage between the sample and the probe and measuring a current through the active layer of the probe.

32. The method of claim 31, comprising rotating the sample with respect to the probe which is pressed to the sample for measuring the current in a different desired orientation alignment between the probe and the sample.

33. The method of claim 31 or 32, comprising sliding the probe with respect to the sample while the probe is pressed to the sample for measuring the current from a different location at the sample.

34. The method of any of claims 31 to 33, where pressing the probe is performed by the SPM apparatus of any one of claims 21 to 30 for the sample carried by said stage.

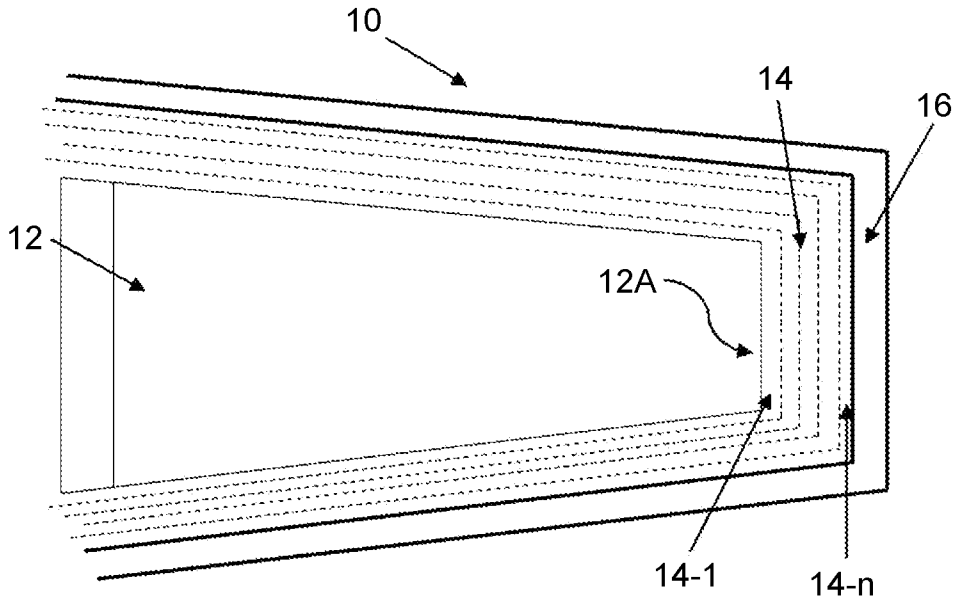

FIG. 1A

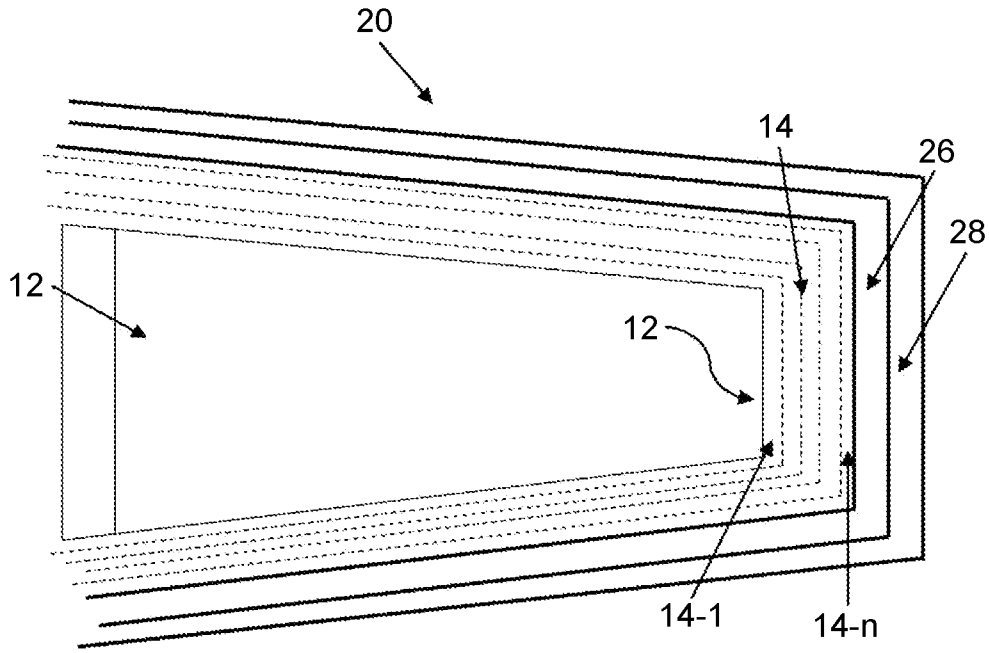

FIG. 1B

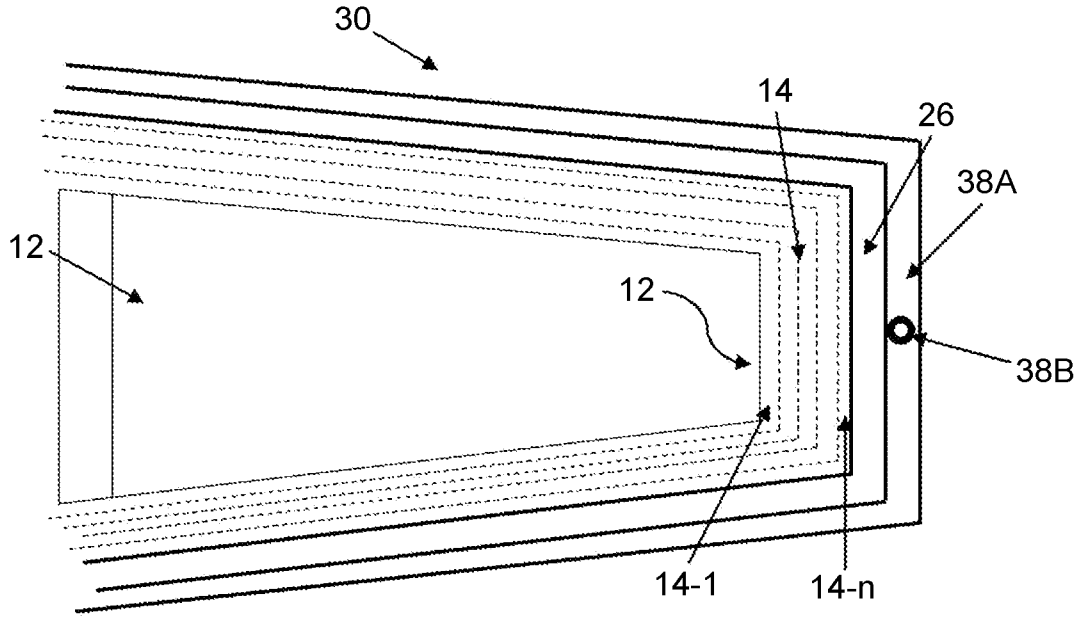

FIG. 1C

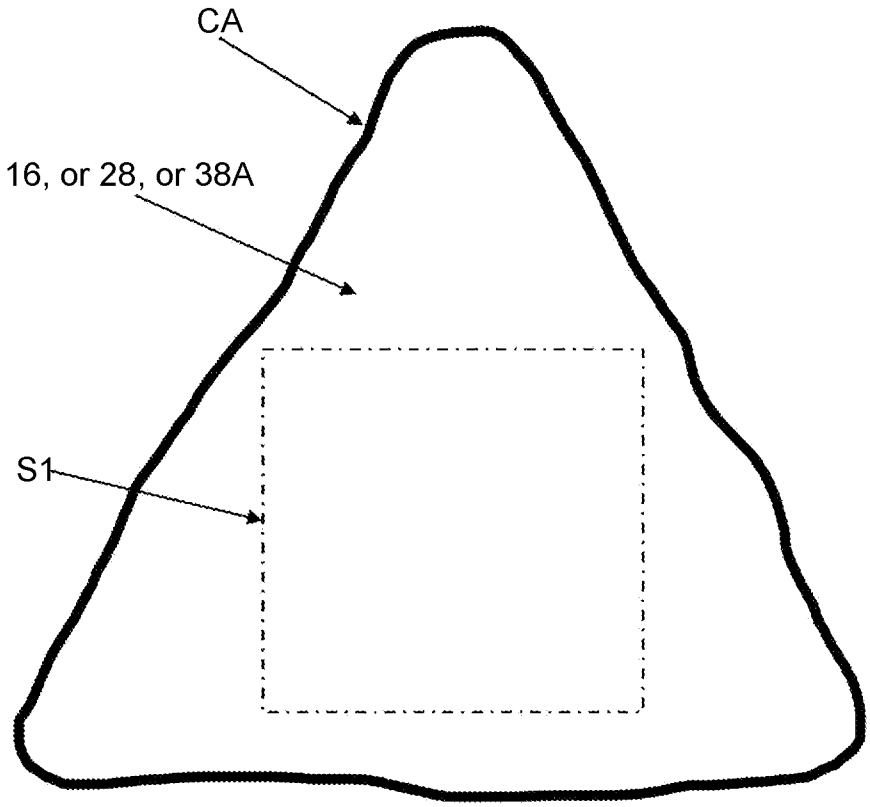

FIG. 2

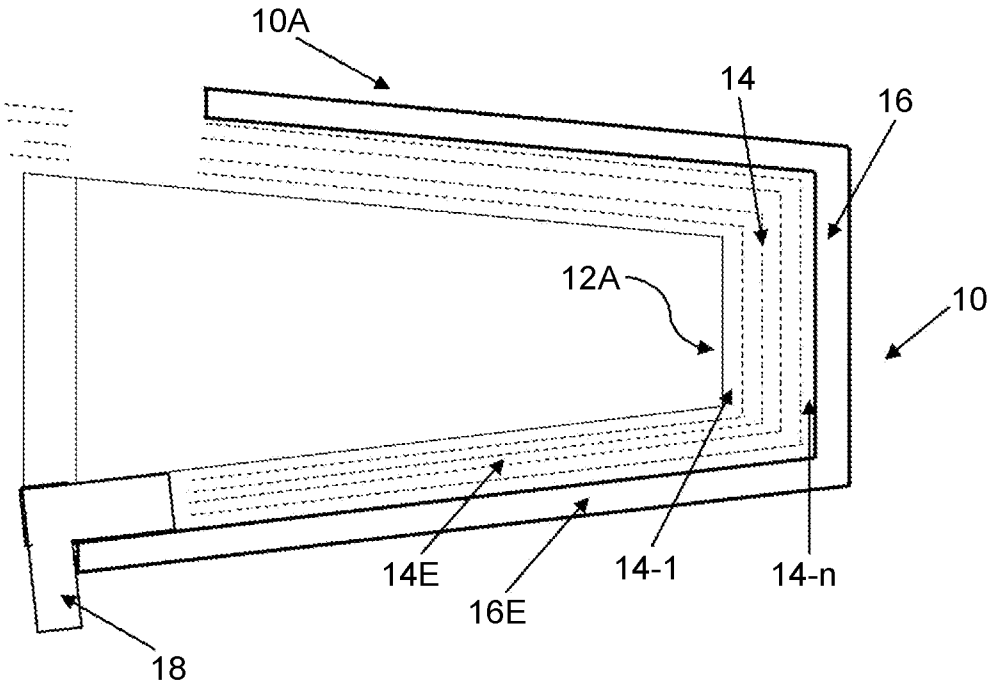

FIG. 3A

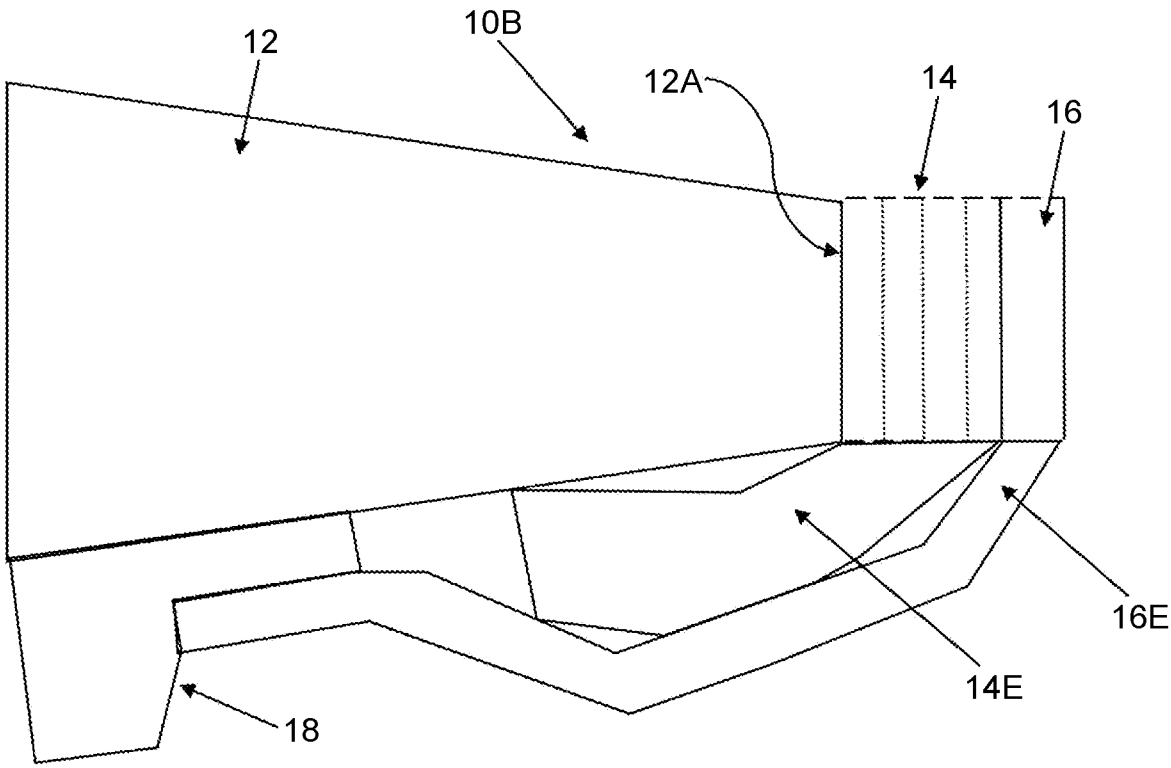

FIG. 3B

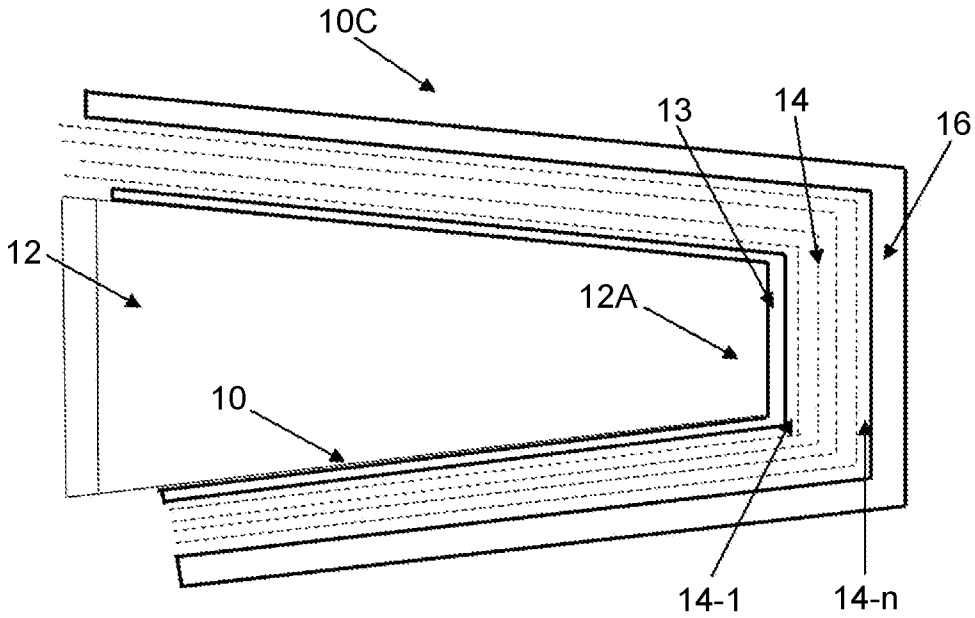

FIG. 4

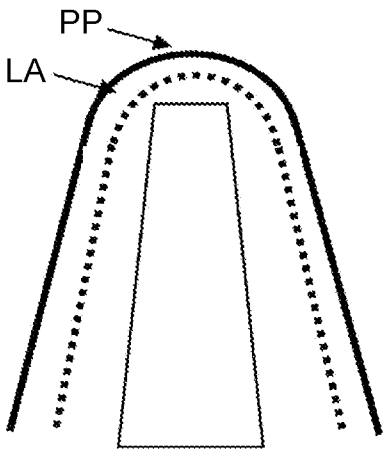

FIG. 5A

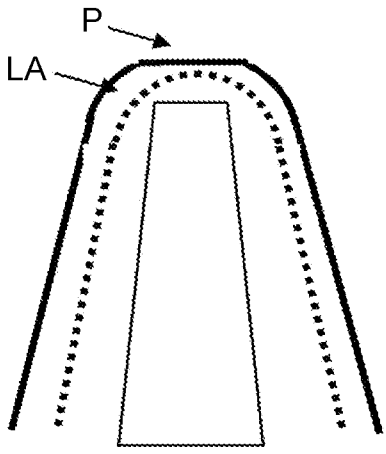

FIG. 5B

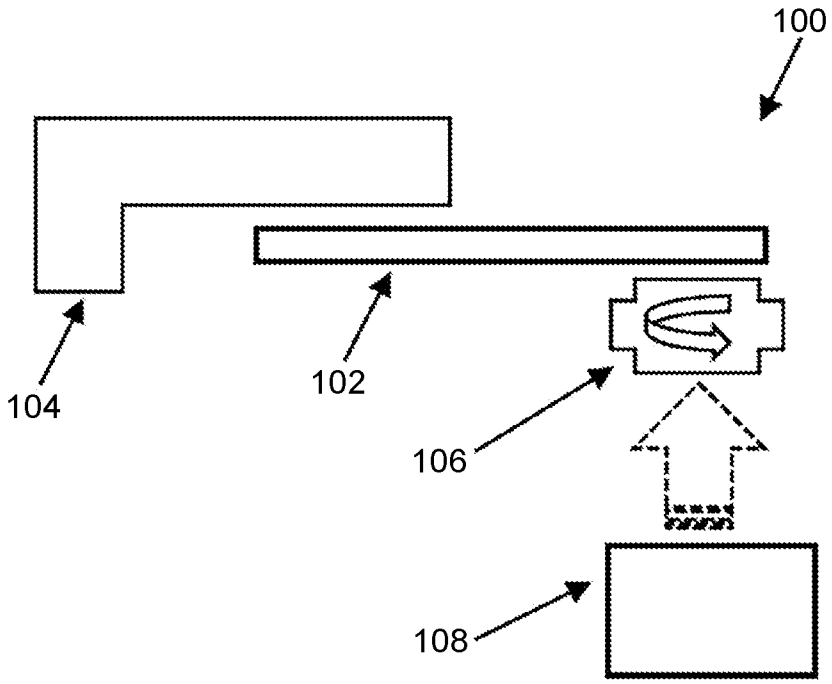

FIG. 6

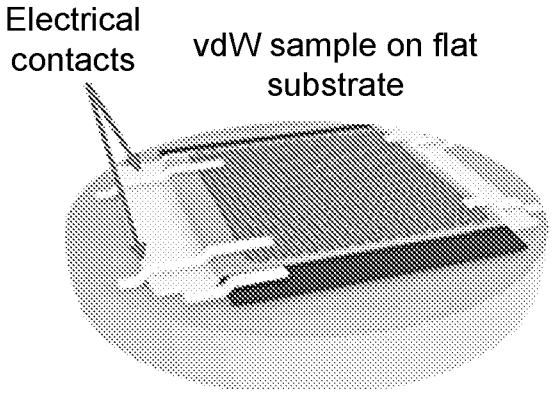

FIG. 7A

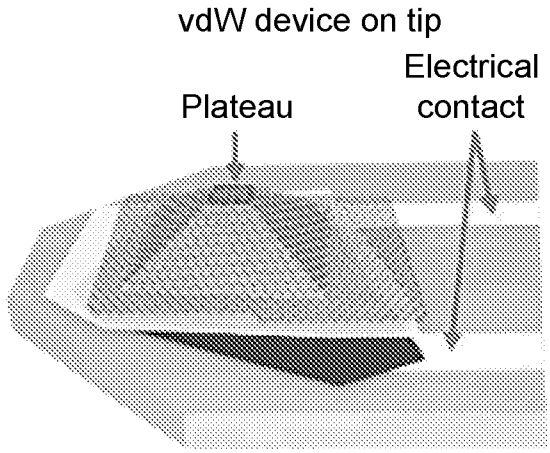

FIG. 7B

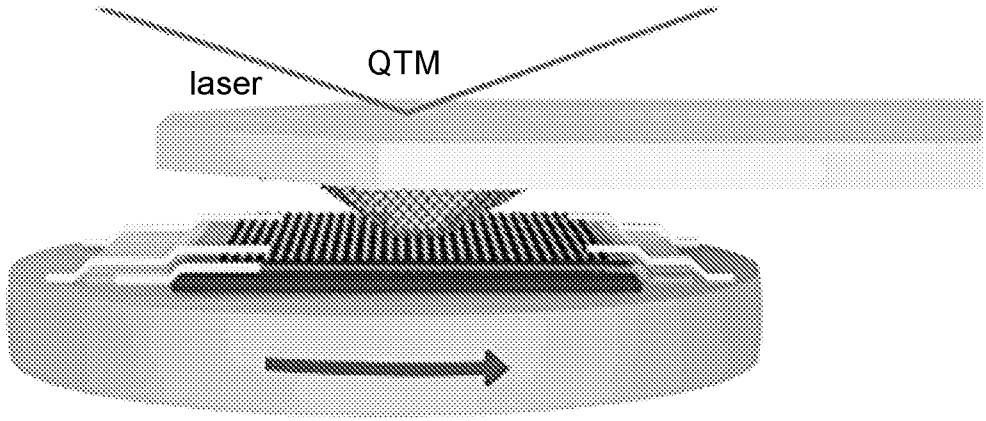

FIG. 7C

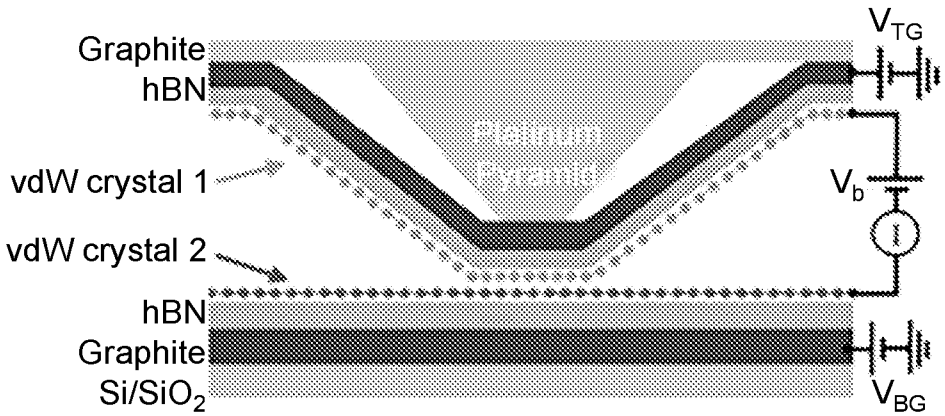

FIG. 7D

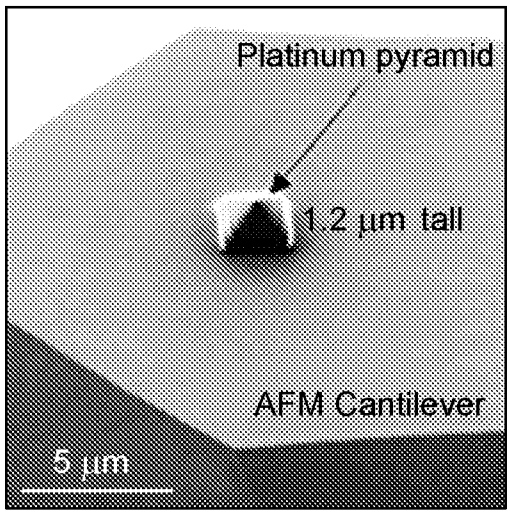

FIG. 7E

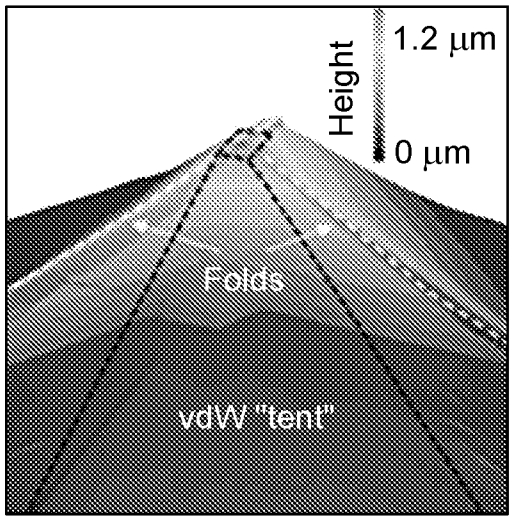

FIG. 7F

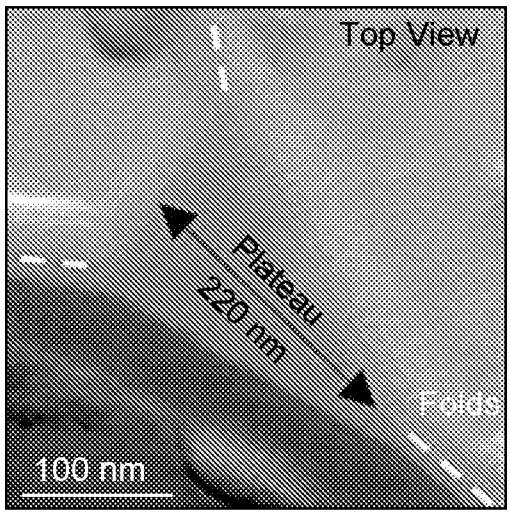

FIG. 7G

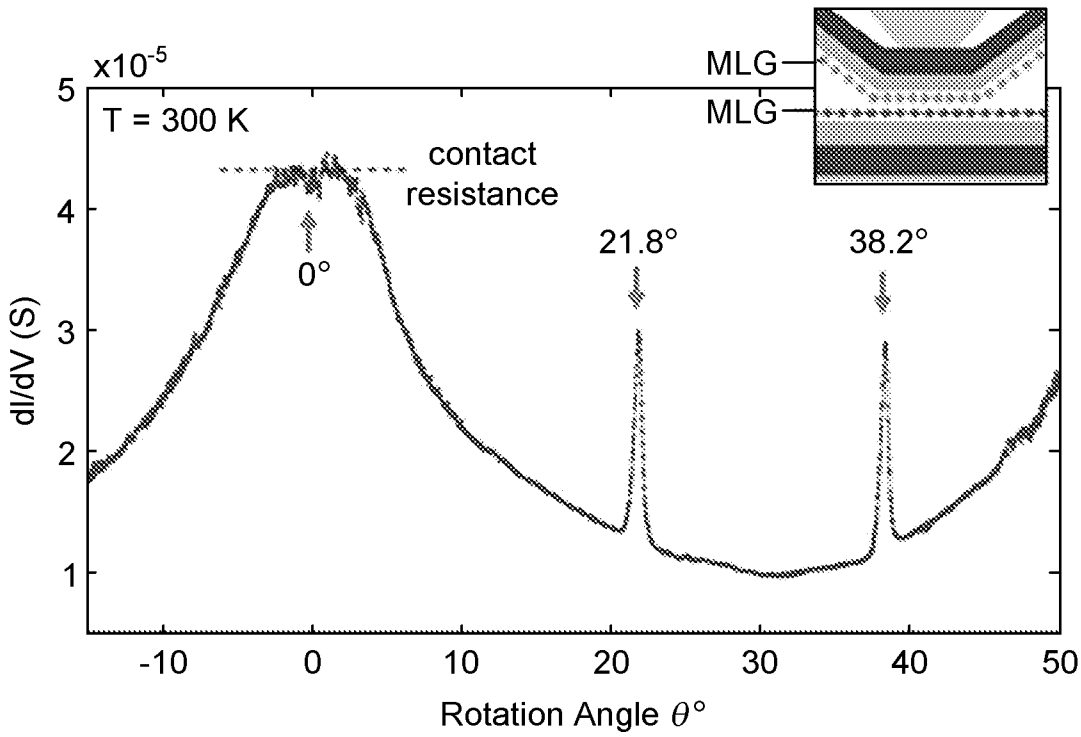

FIG. 7H

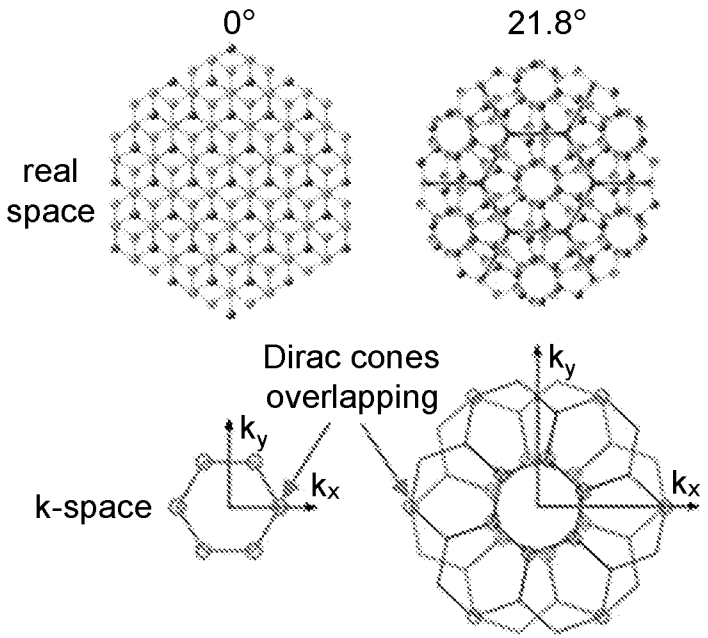

FIG. 7I

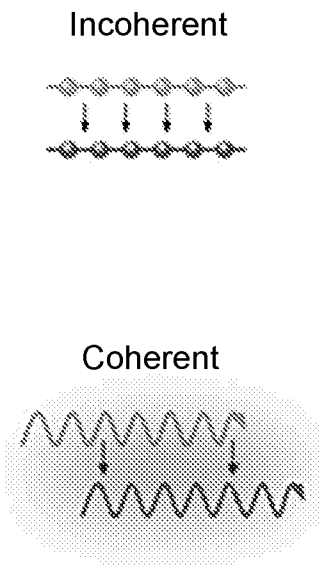

FIG. 7J

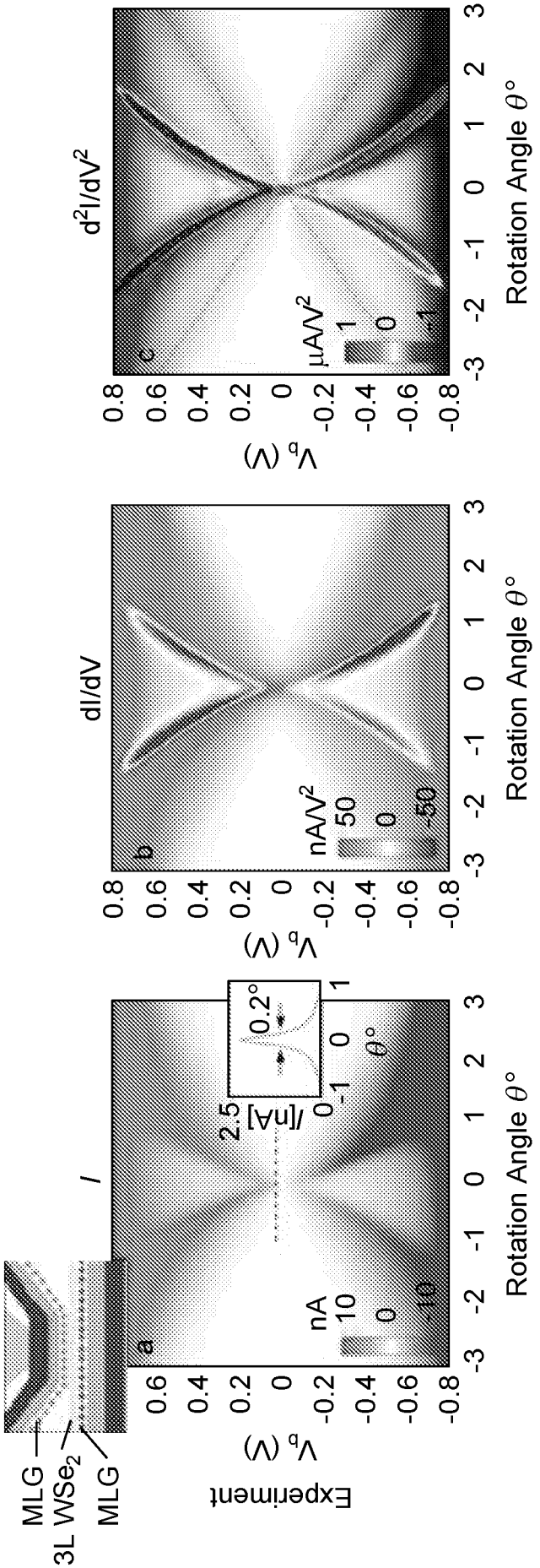

FIG. 8A

FIG. 8B

FIG. 8C

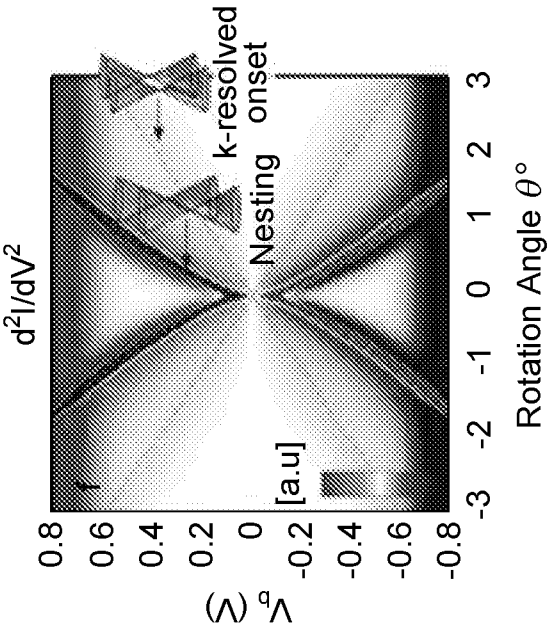

FIG. 8F

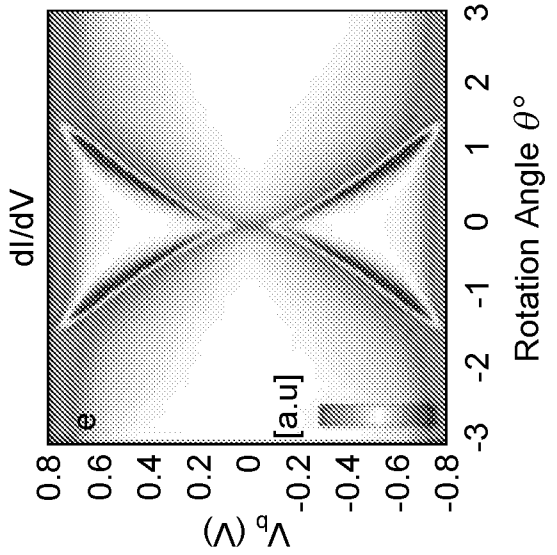

FIG. 8E

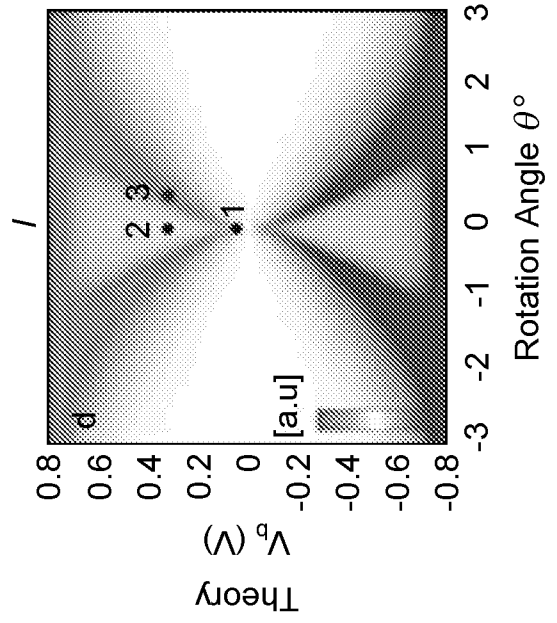

FIG. 8D

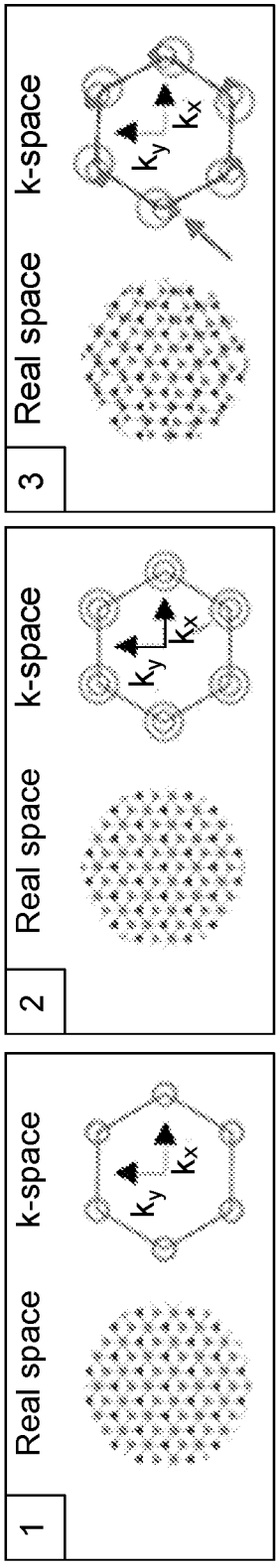
1
Real space
k-space
k_y
k_x
2
Real space
k-space
k_y
k_x
3
Real space
k-space
k_y
k_x

FIG. 8G

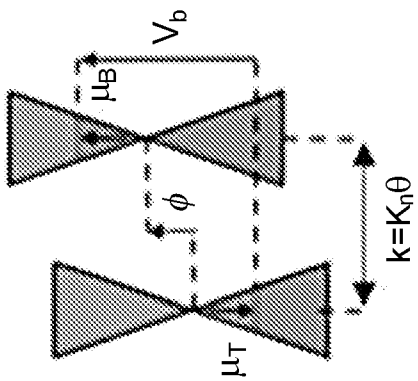
V_b
μ_B
ϕ
μ_T
$k=K_n\theta$

FIG. 8H

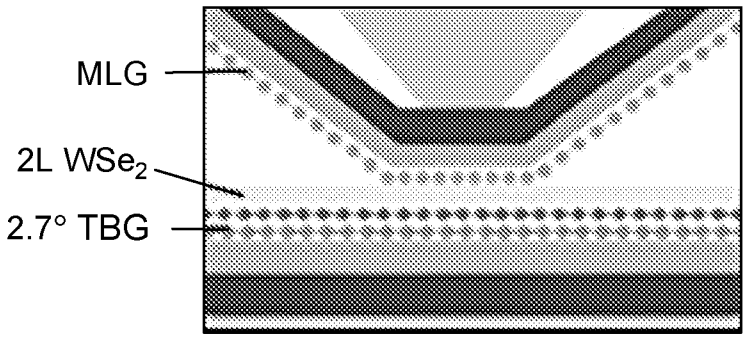

FIG. 9A

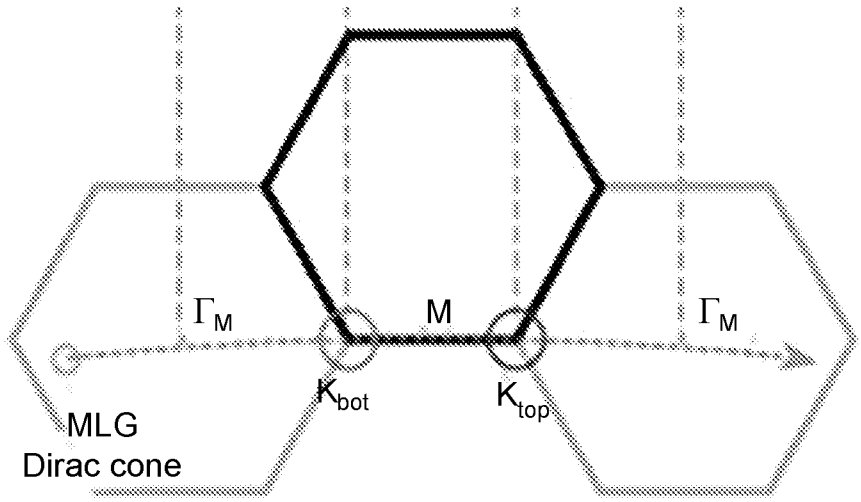

FIG. 9B

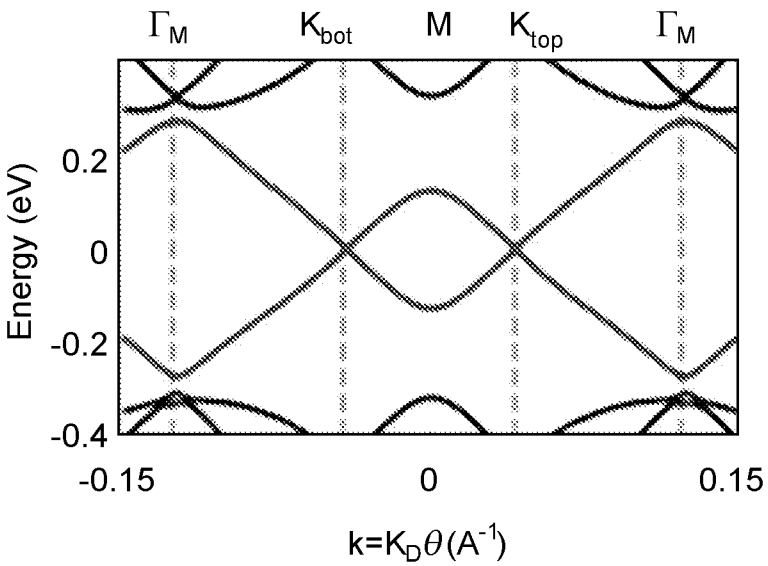

FIG. 9C

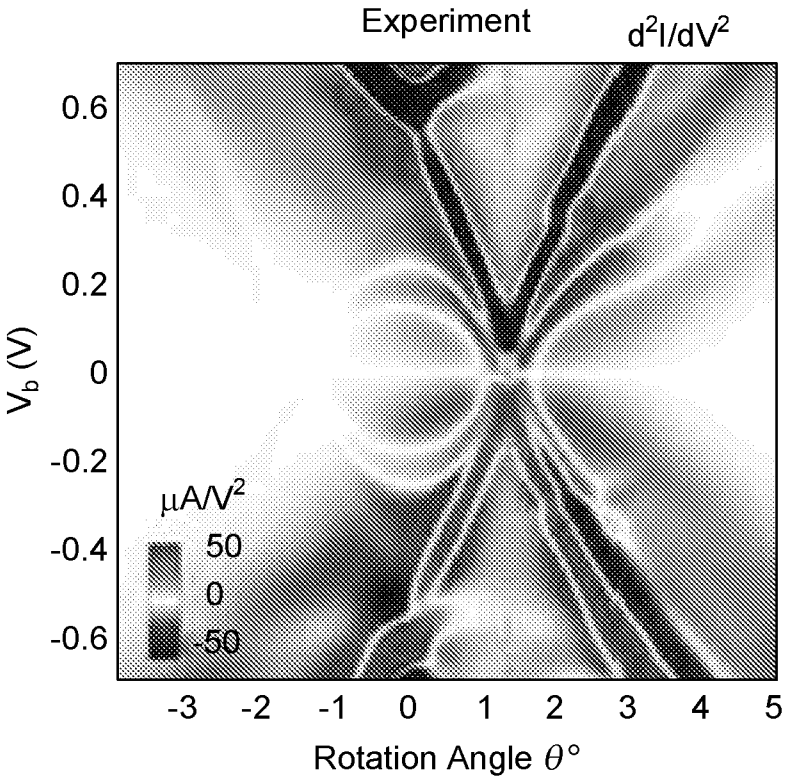
Experiment
d^2I/dV^2
0.6
0.4
0.2
0
-0.2
-0.4
-0.6
V_b (V)
μA/V²
50
0
-50
-3 -2 -1 0 1 2 3 4 5
Rotation Angle θ°

FIG. 9D

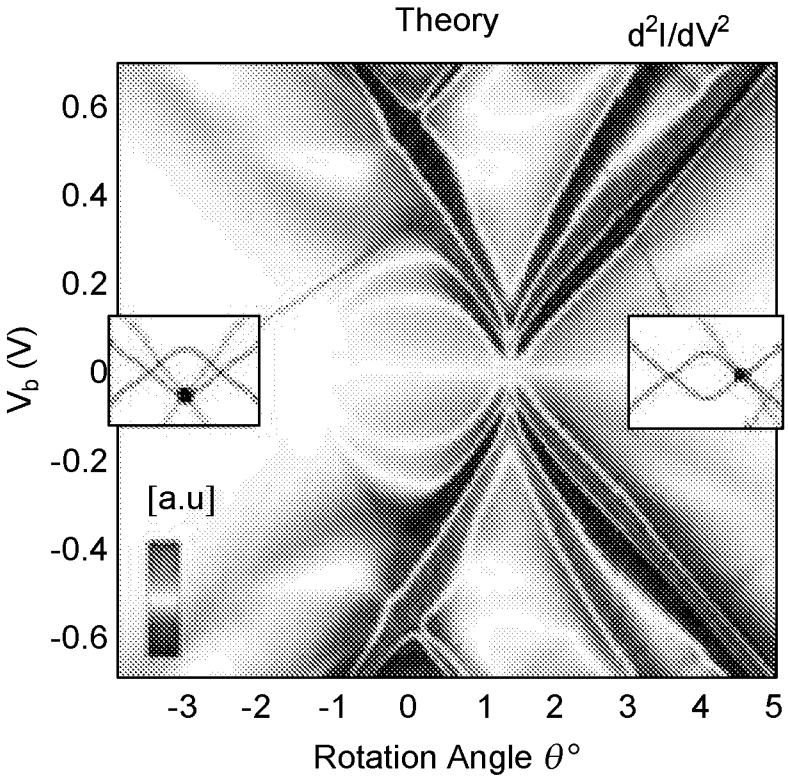
Theory
d^2I/dV^2
0.6
0.4
0.2
0
-0.2
-0.4
-0.6
V_b (V)
[a.u]
-3 -2 -1 0 1 2 3 4 5
Rotation Angle θ°

FIG. 9E

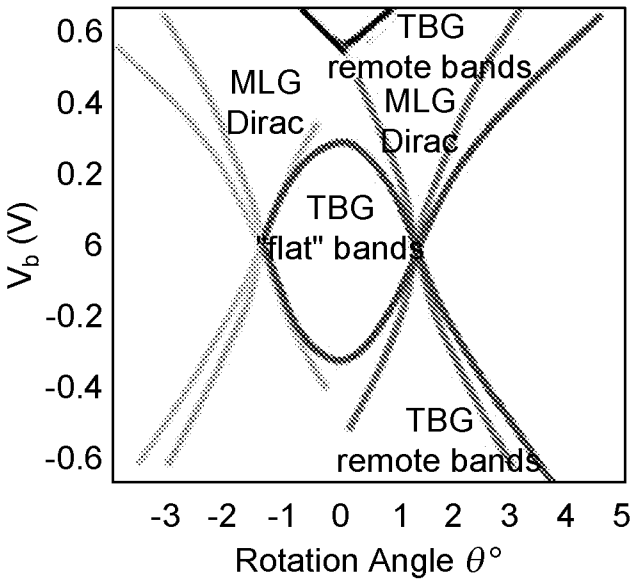

FIG. 9F

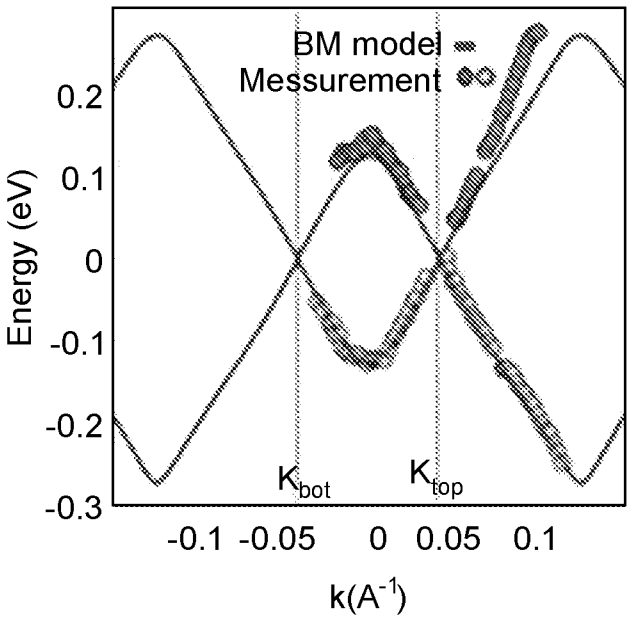

FIG. 9H

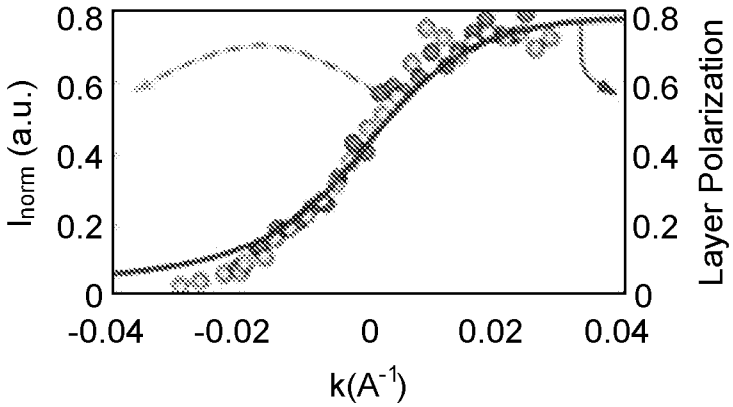

FIG. 9I

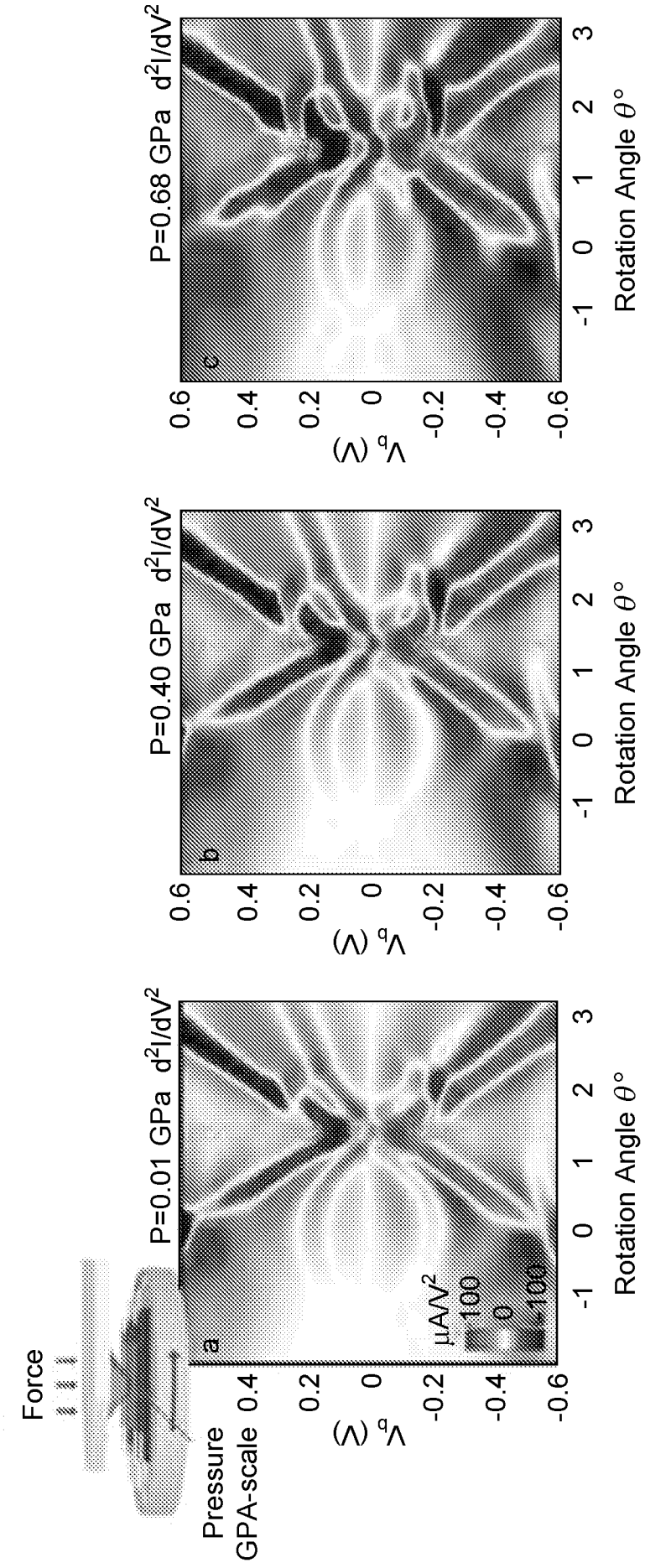

FIG. 10A

FIG. 10B

FIG. 10C

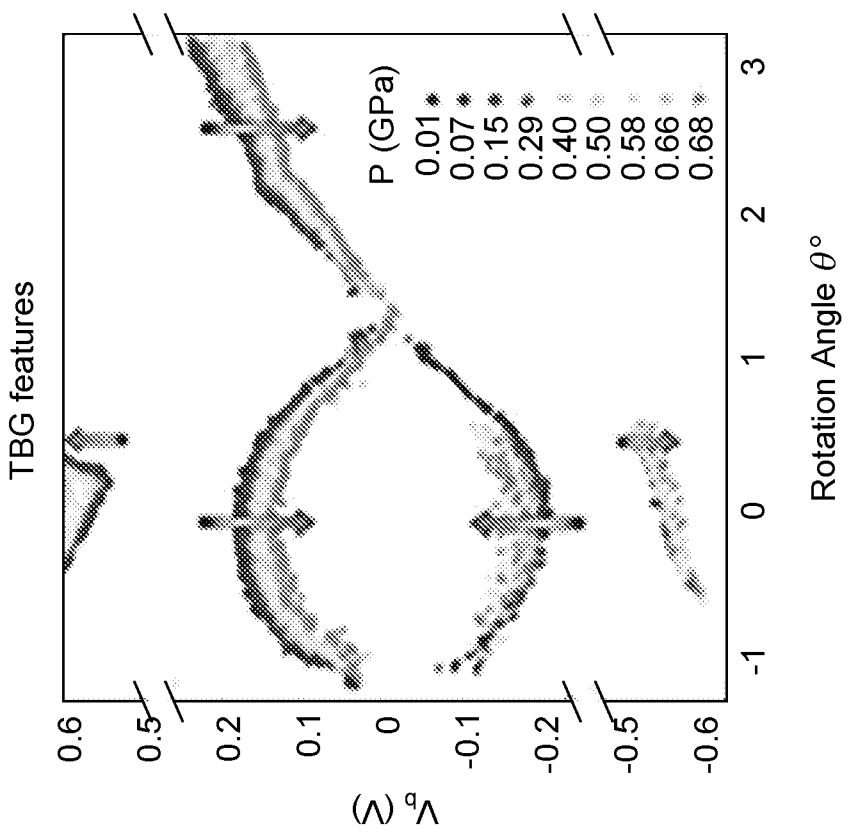

FIG. 10D

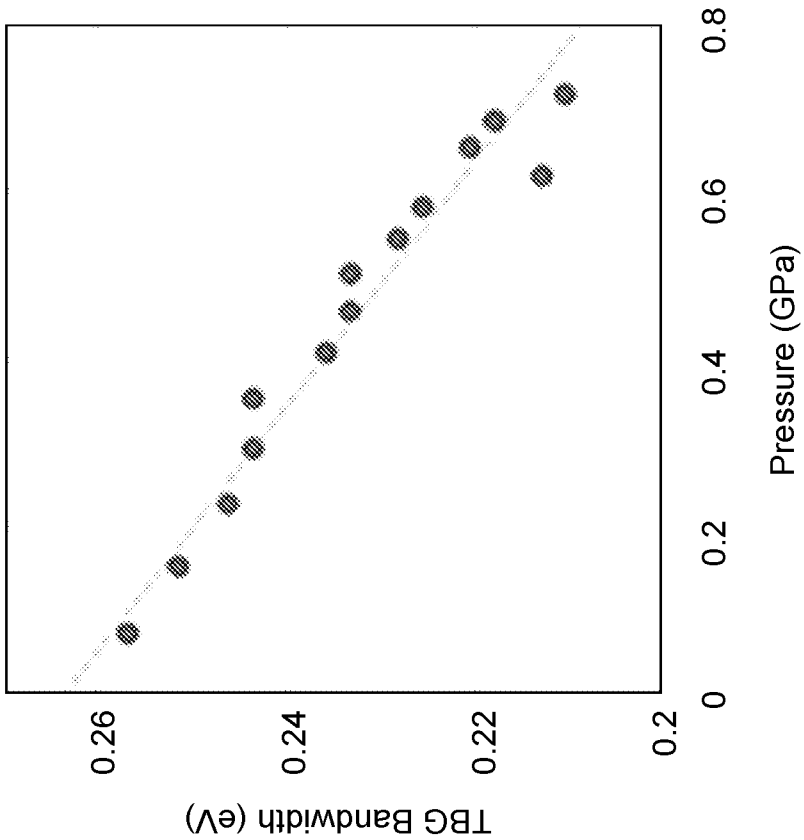

FIG. 10E

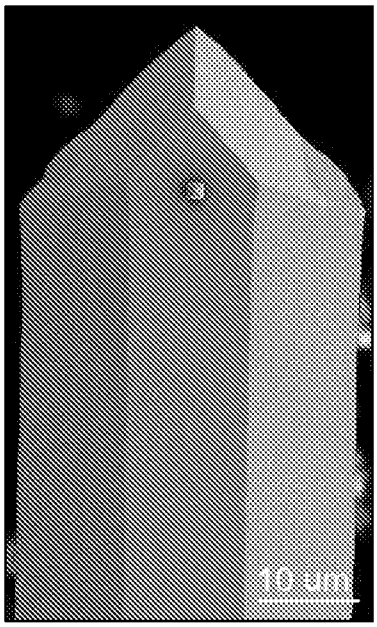

FIG. 11A

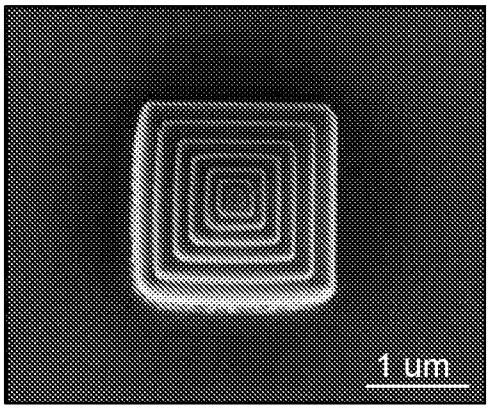

FIG. 11B

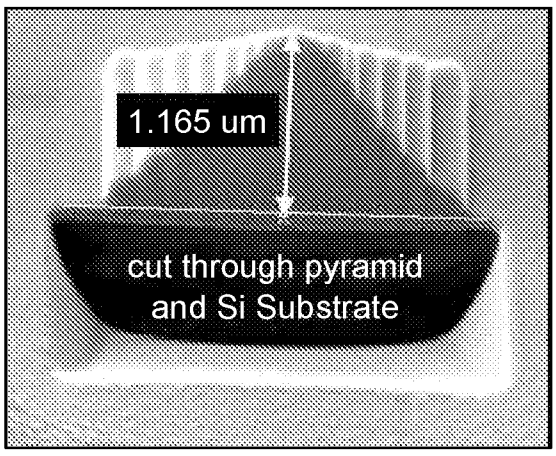

FIG. 11C

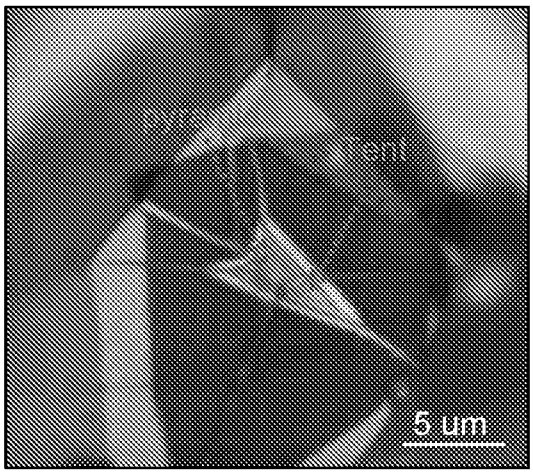

FIG. 11D

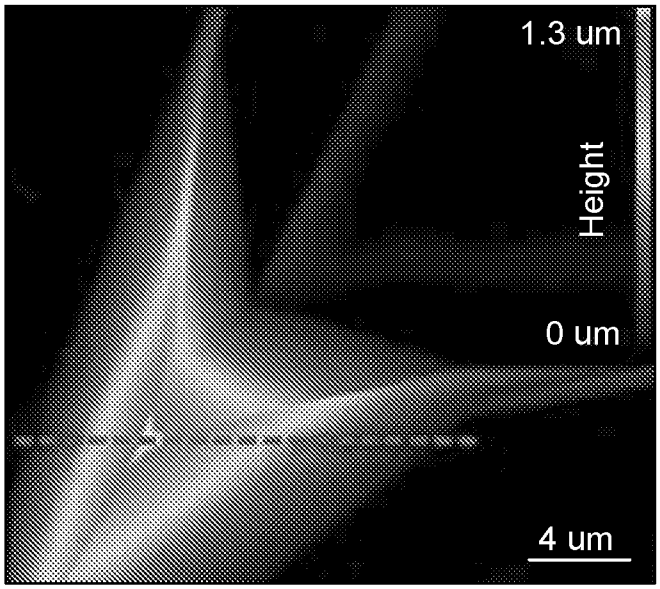

FIG. 11E

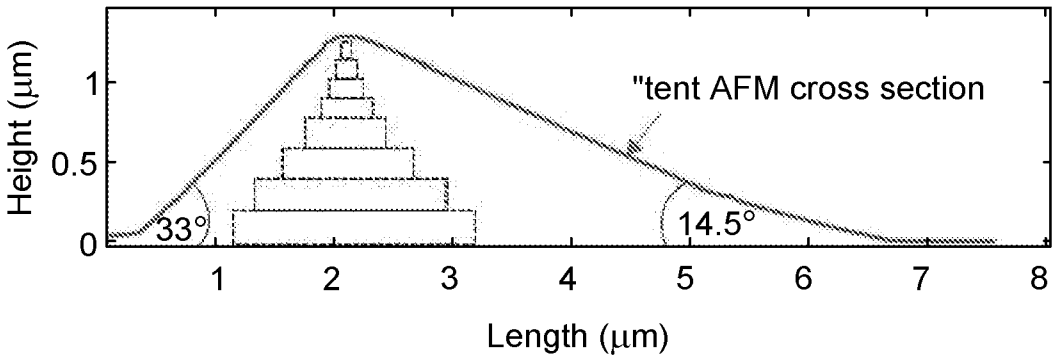

FIG. 11F

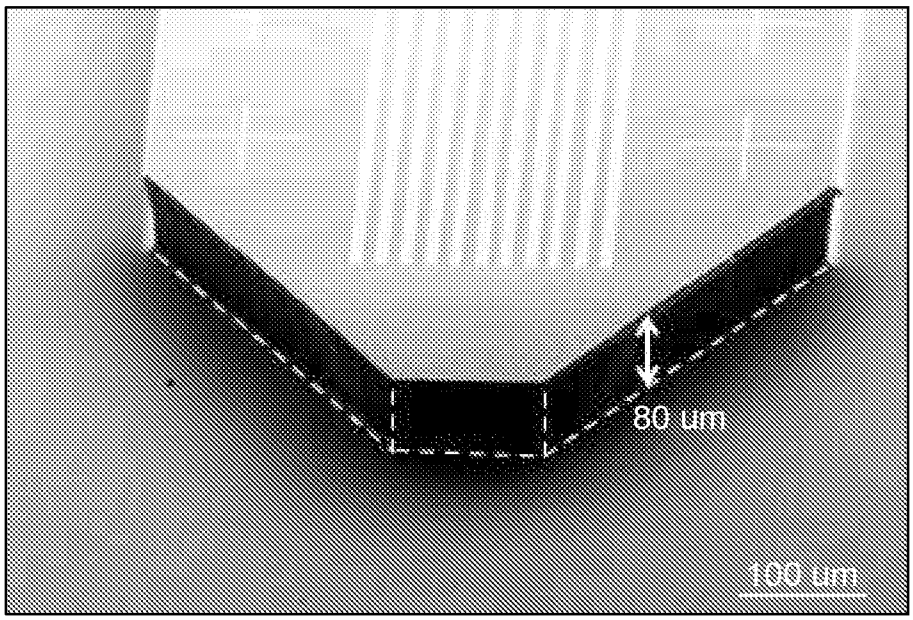

FIG. 12A

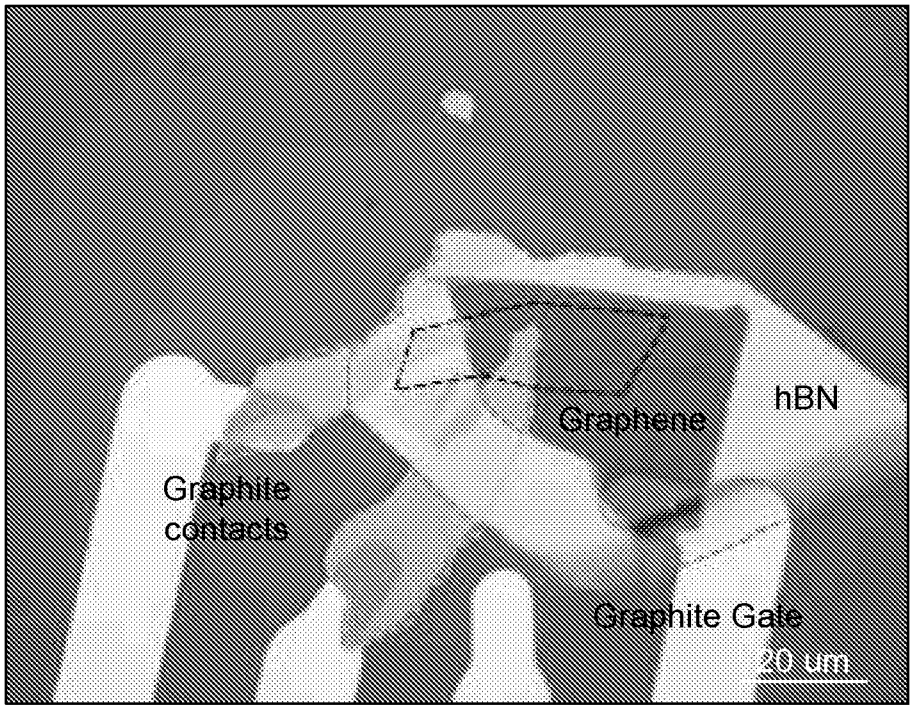

FIG. 12B

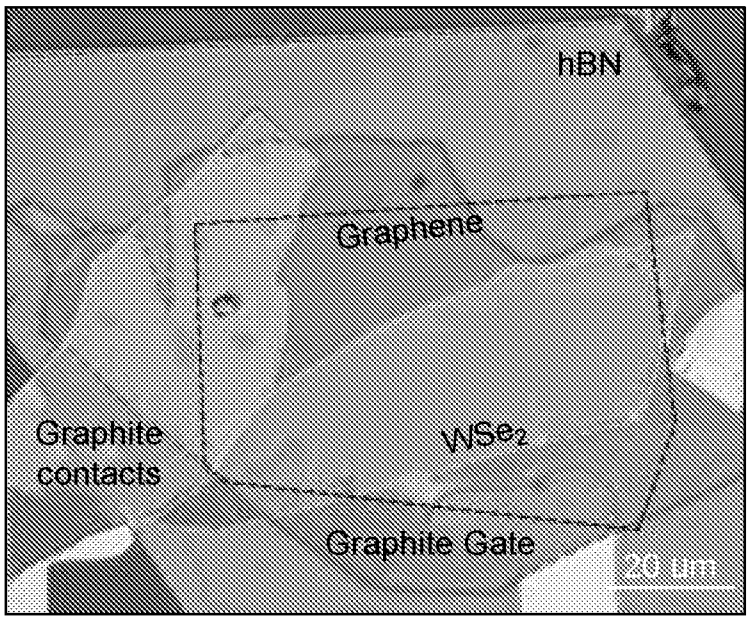

FIG. 12C

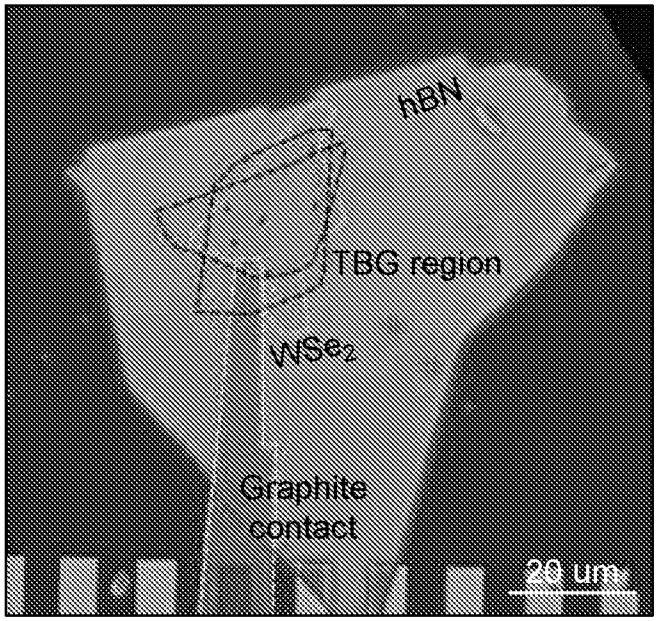

FIG. 12D

Integration into AFM

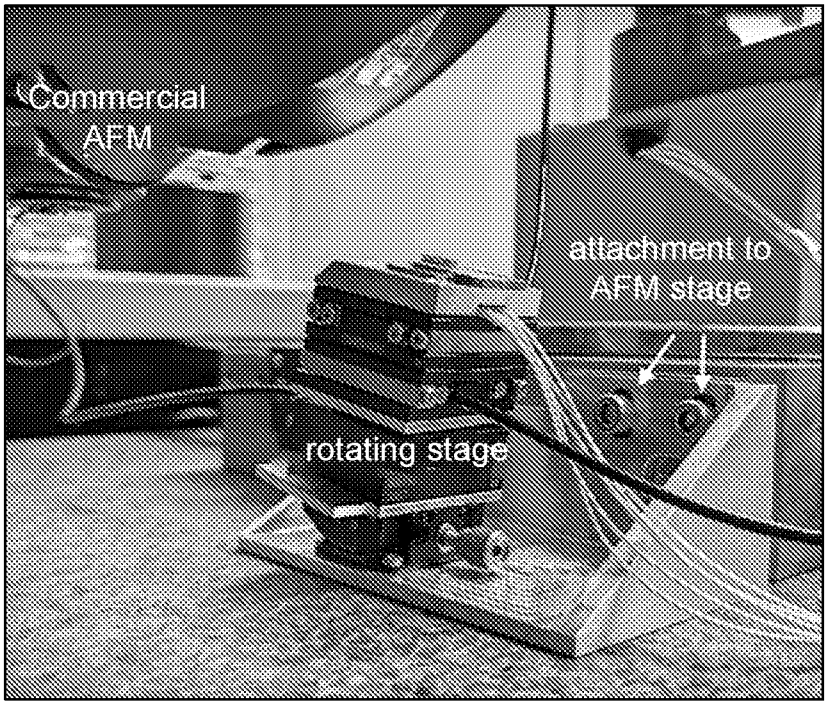

FIG. 13A

measurement

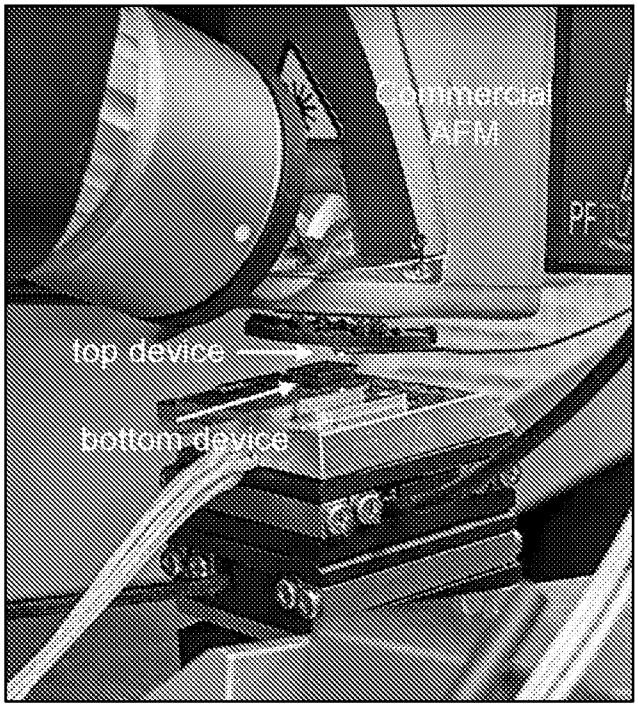

FIG. 13B

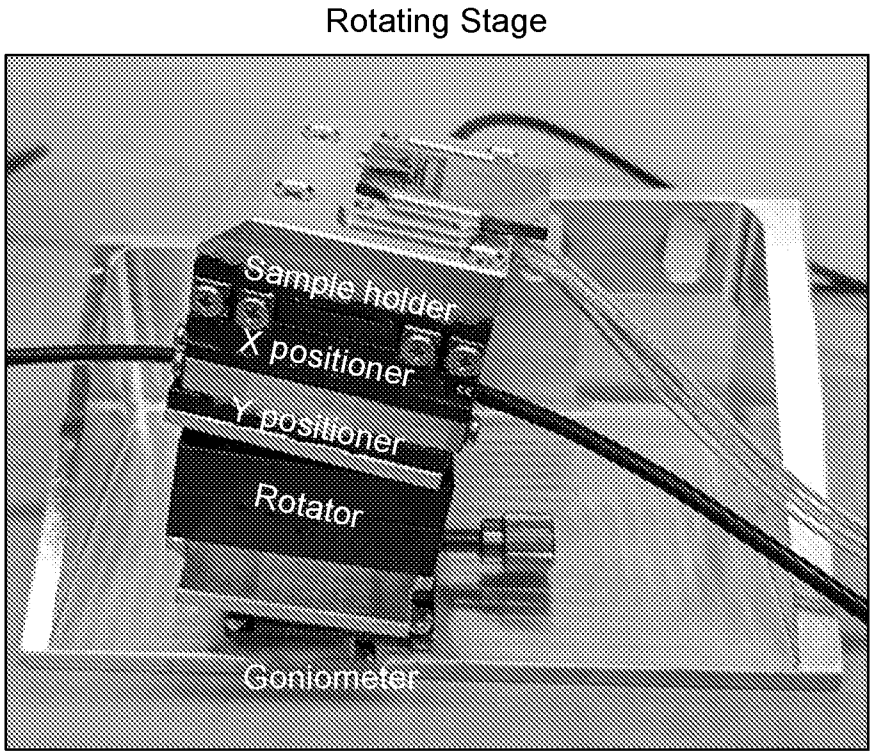

FIG. 13C

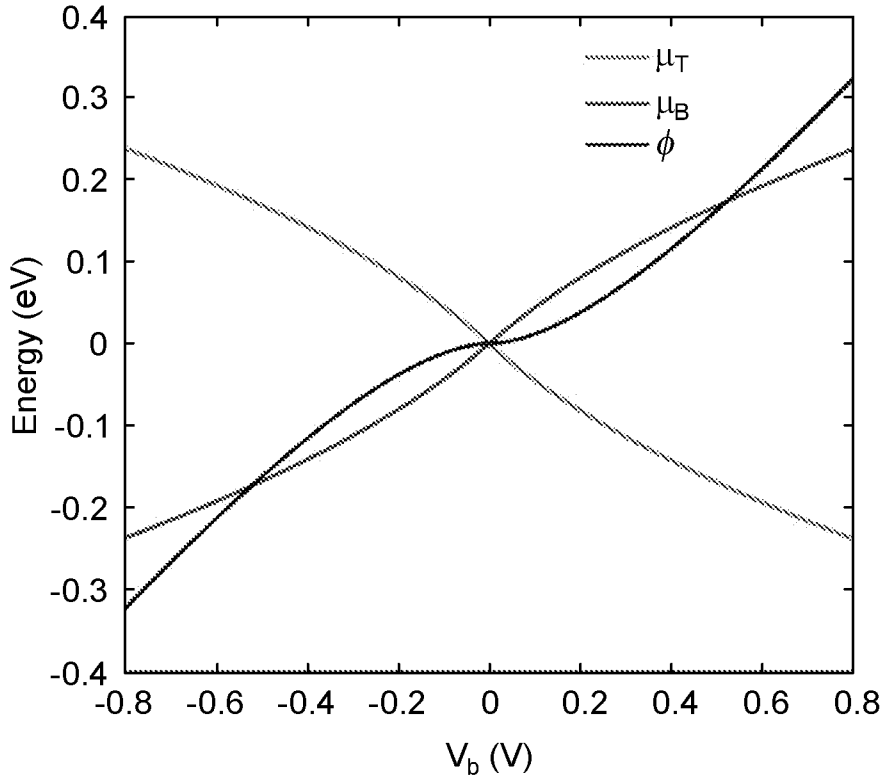

FIG. 14

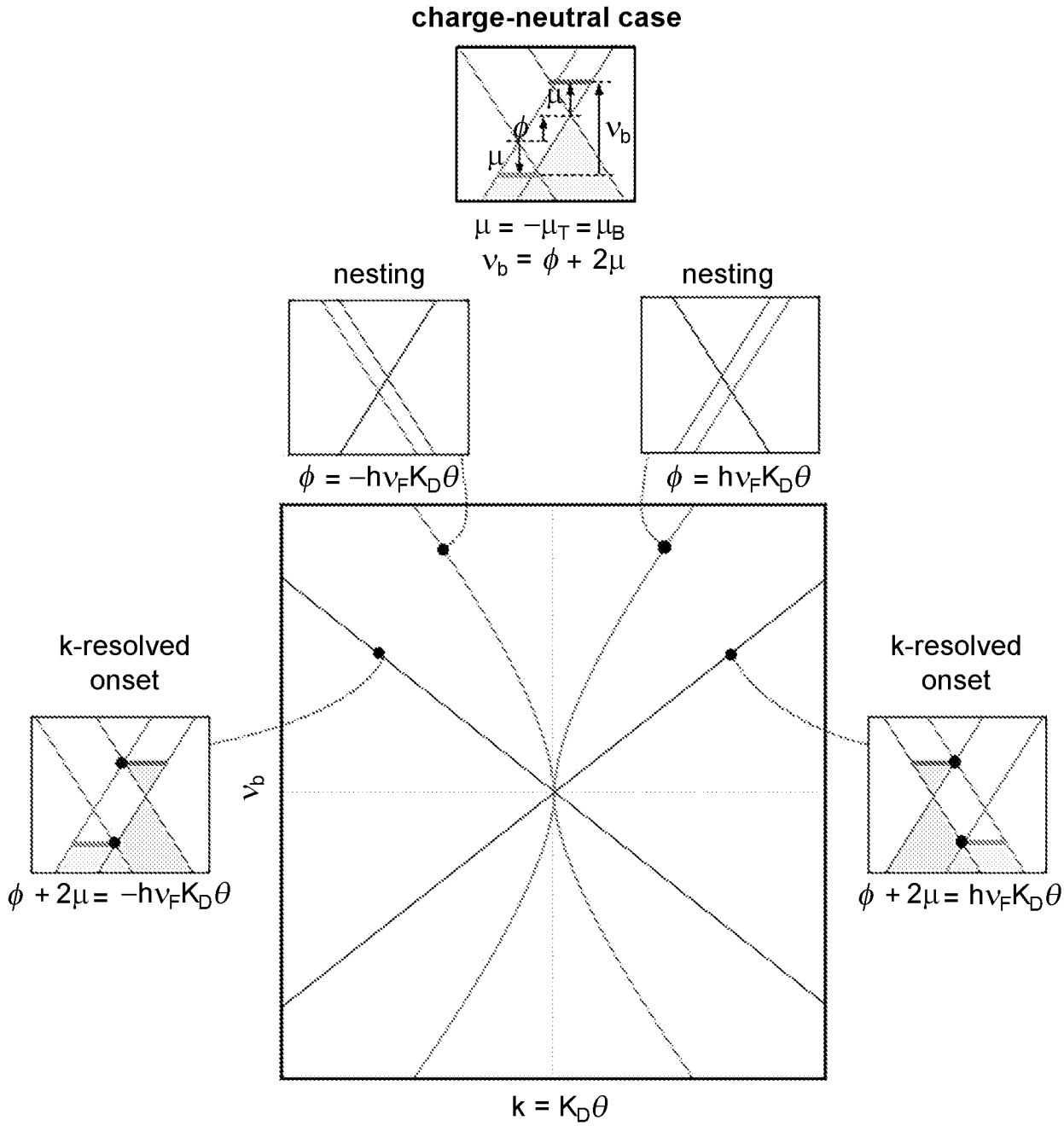
charge-neutral case
μ
ϕ
μ
ν_b
$\mu = -\mu_T = \mu_B$
$\nu_b = \phi + 2\mu$
nesting
nesting
$\phi = -h\nu_F K_D \theta$
$\phi = h\nu_F K_D \theta$
k-resolved onset
k-resolved onset
ν_b
$\phi + 2\mu = -h\nu_F K_D \theta$
$\phi + 2\mu = h\nu_F K_D \theta$
$k = K_D \theta$

FIG. 15

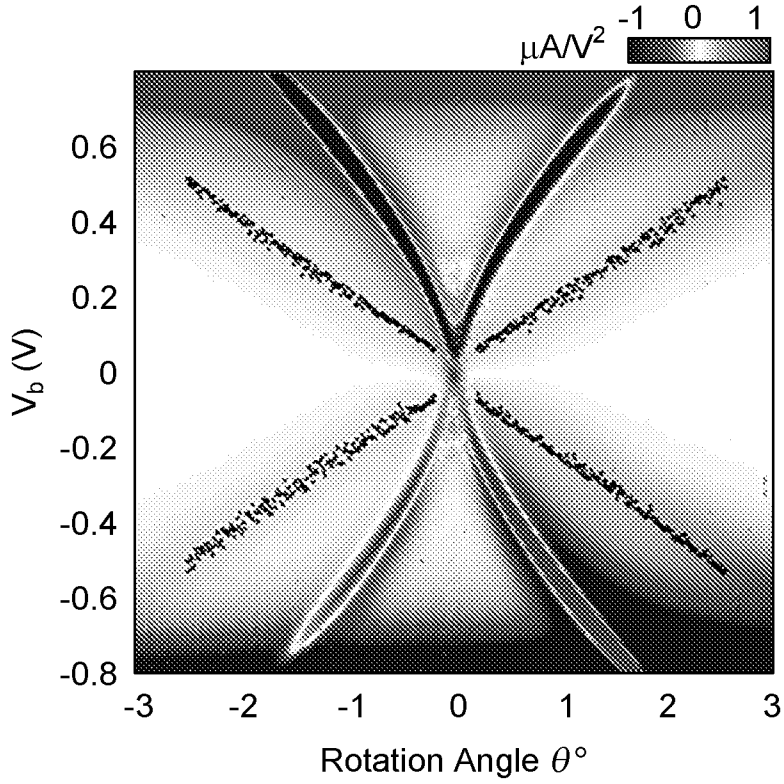

FIG. 16A

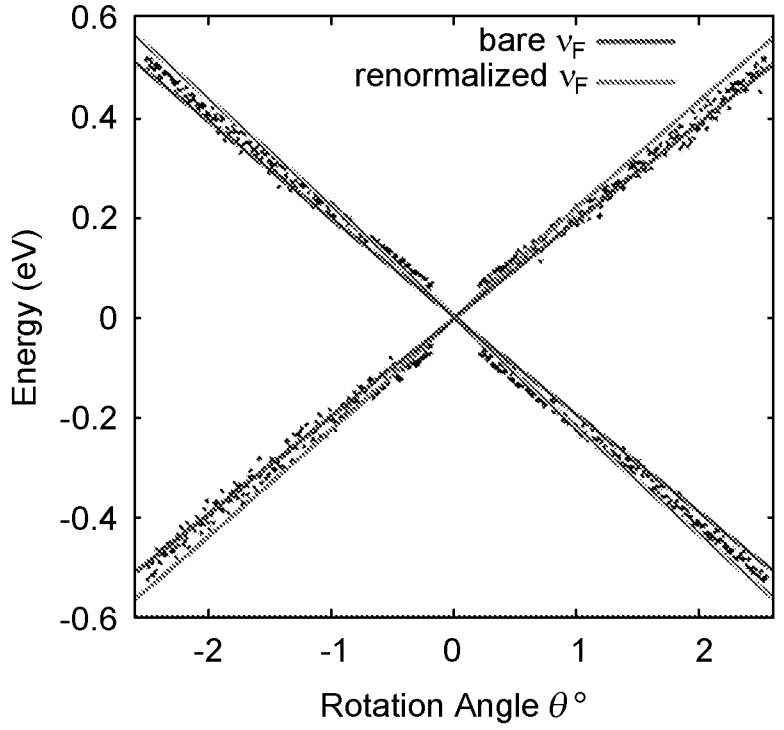

FIG. 16B

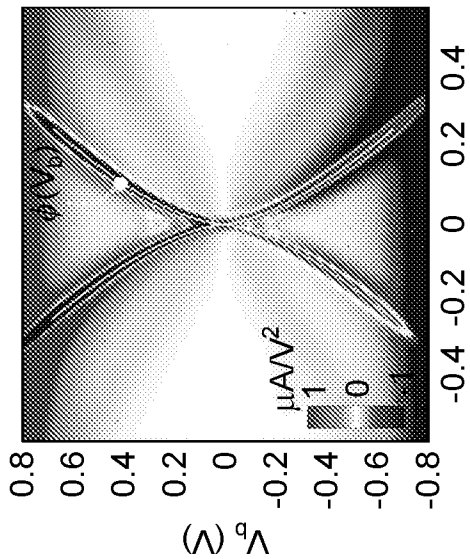

FIG. 17A

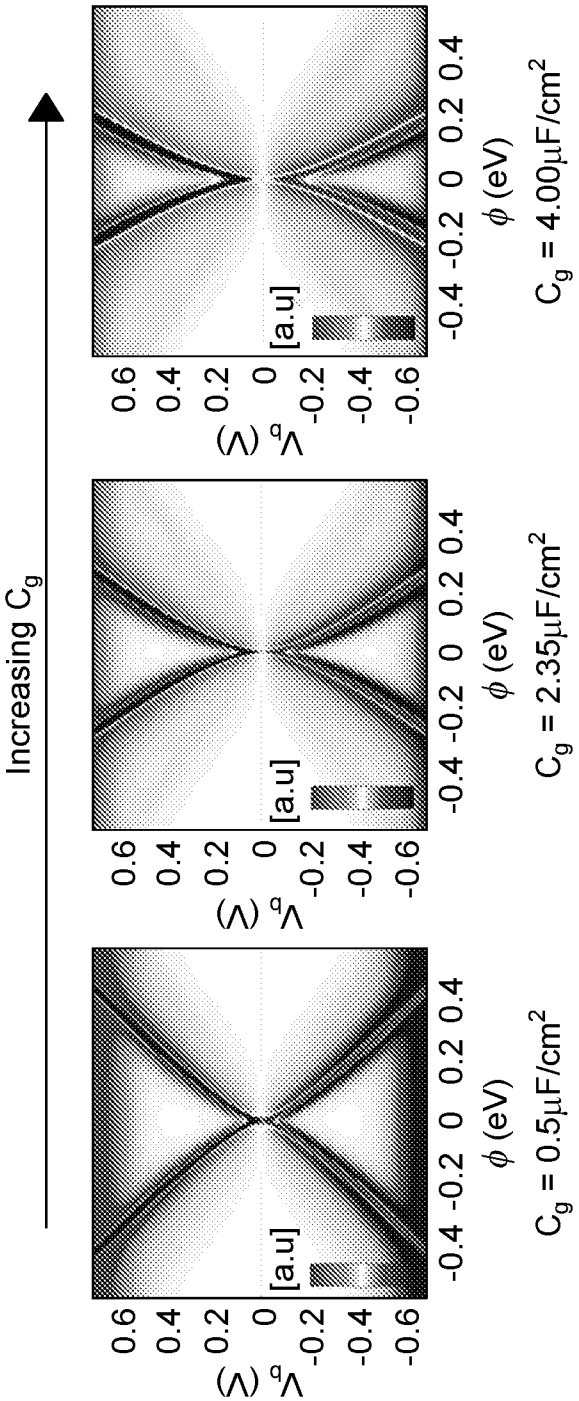

FIG. 17B

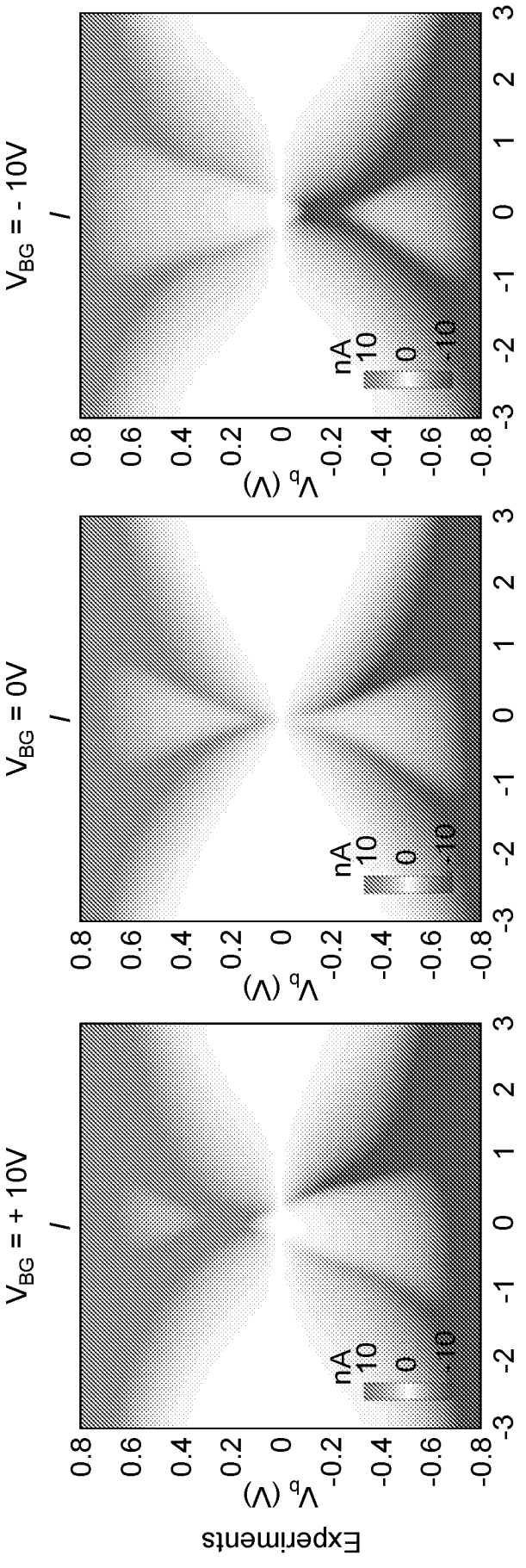

FIG. 18A

FIG. 18B

FIG. 18C

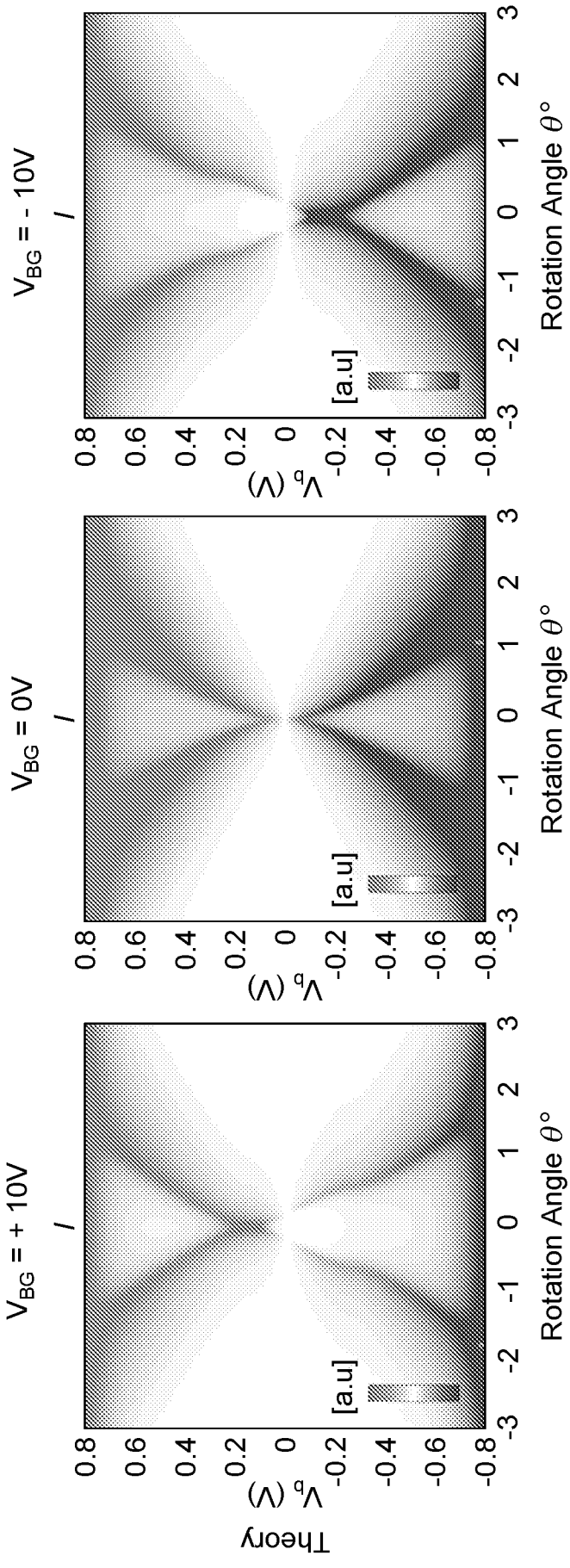

FIG. 18D

FIG. 18E

FIG. 18F

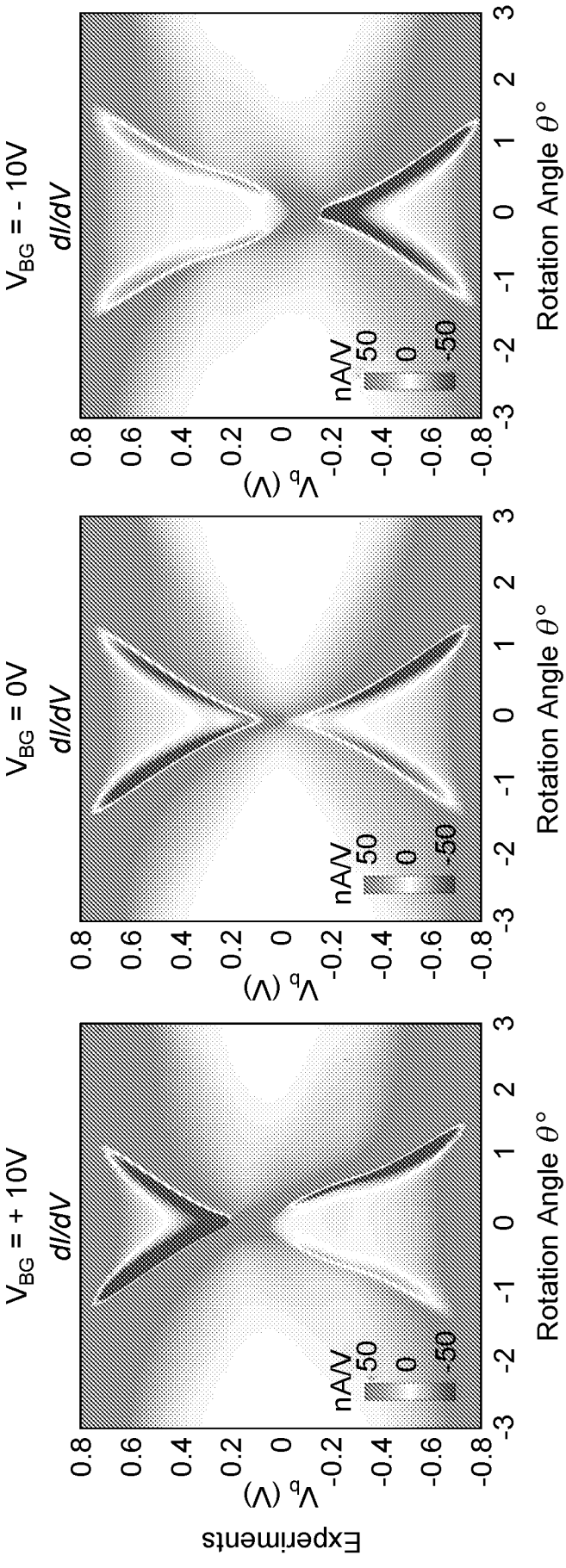

FIG. 19A

FIG. 19B

FIG. 19C

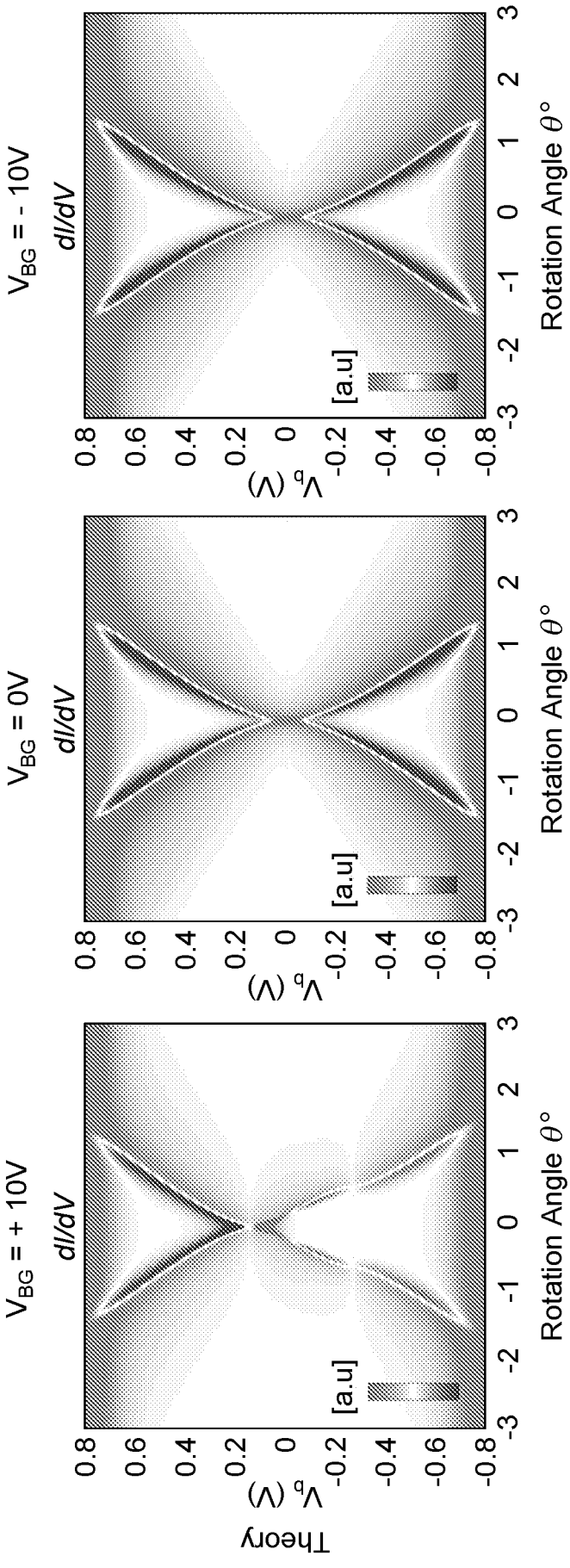

FIG. 19D

FIG. 19E

FIG. 19F

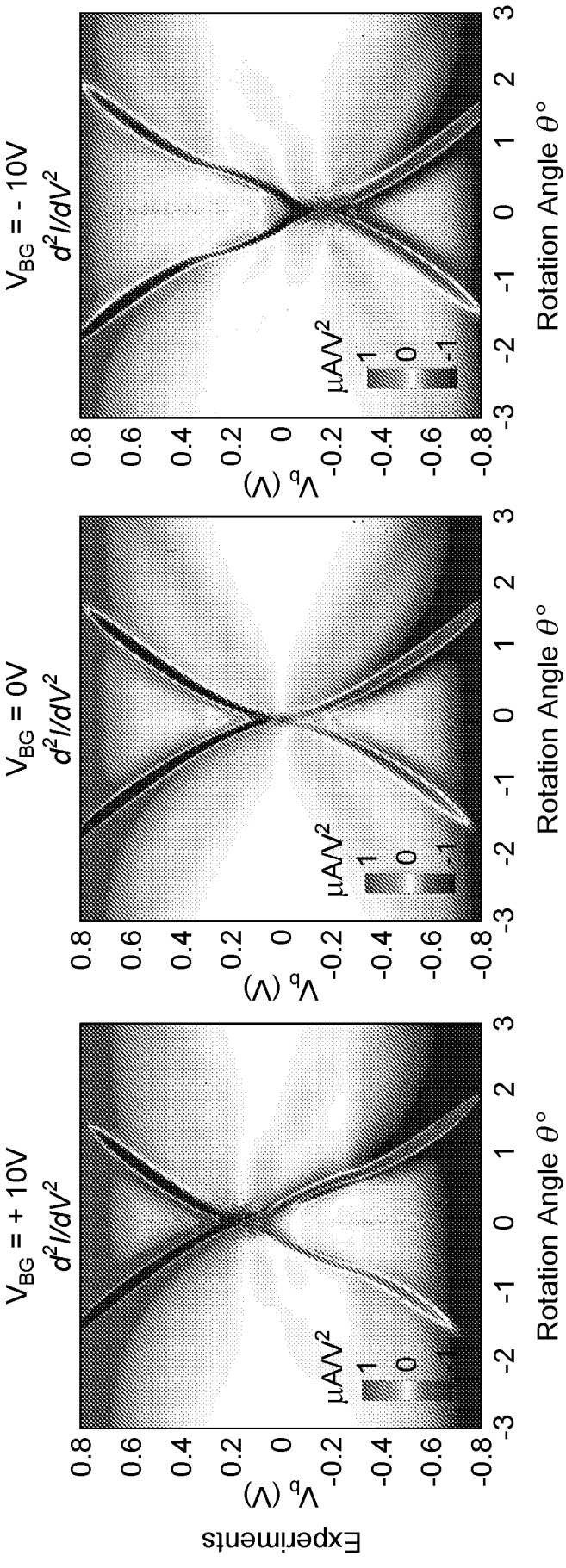

FIG. 20A

FIG. 20B

FIG. 20C

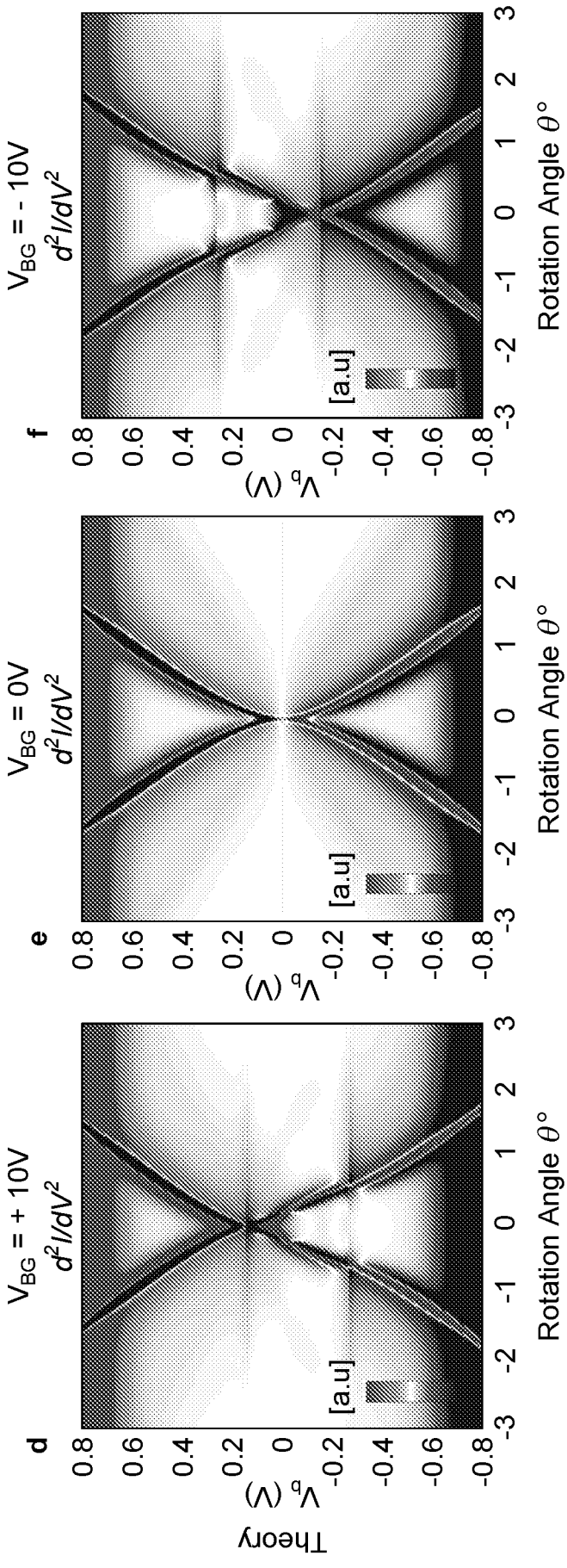

FIG. 20D

FIG. 20E

FIG. 20F

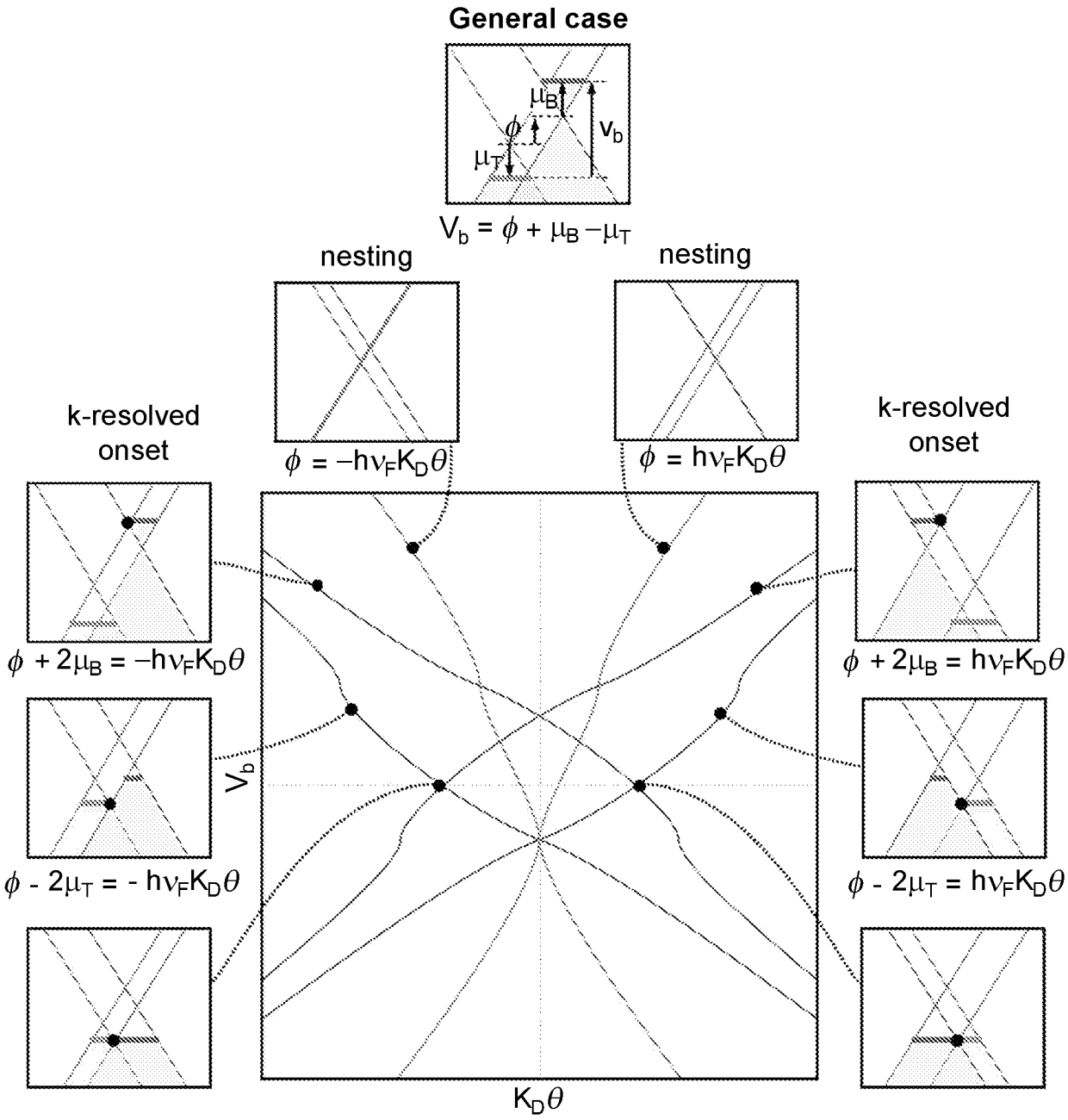
General case
μ_B
ϕ
v_b
μ_T
$V_b = \phi + \mu_B - \mu_T$
nesting
nesting
k-resolved onset
k-resolved onset
$\phi = -h\nu_F K_D \theta$
$\phi = h\nu_F K_D \theta$
$\phi + 2\mu_B = -h\nu_F K_D \theta$
$\phi + 2\mu_B = h\nu_F K_D \theta$
V_b
$\phi - 2\mu_T = - h\nu_F K_D \theta$
$\phi - 2\mu_T = h\nu_F K_D \theta$
$K_D \theta$

FIG. 21

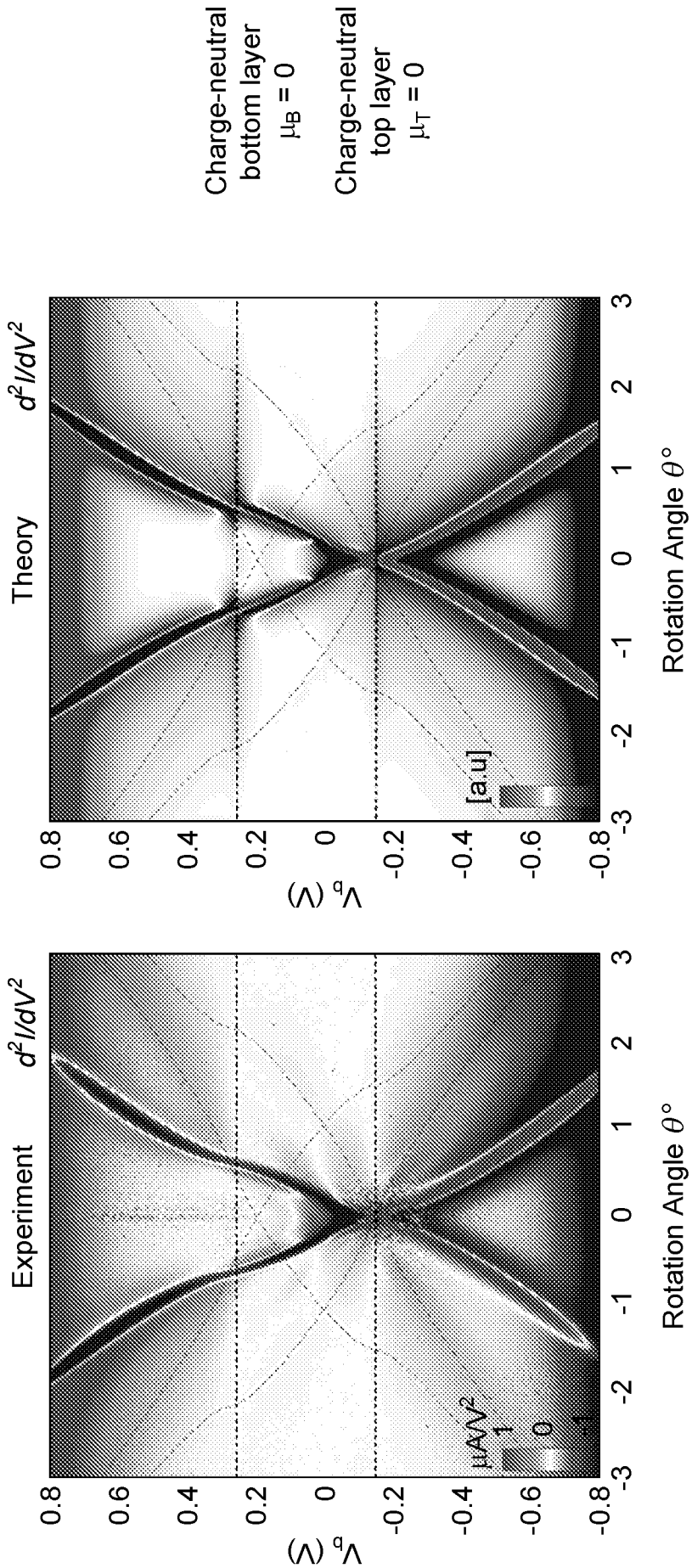

FIG. 22B

FIG. 22A

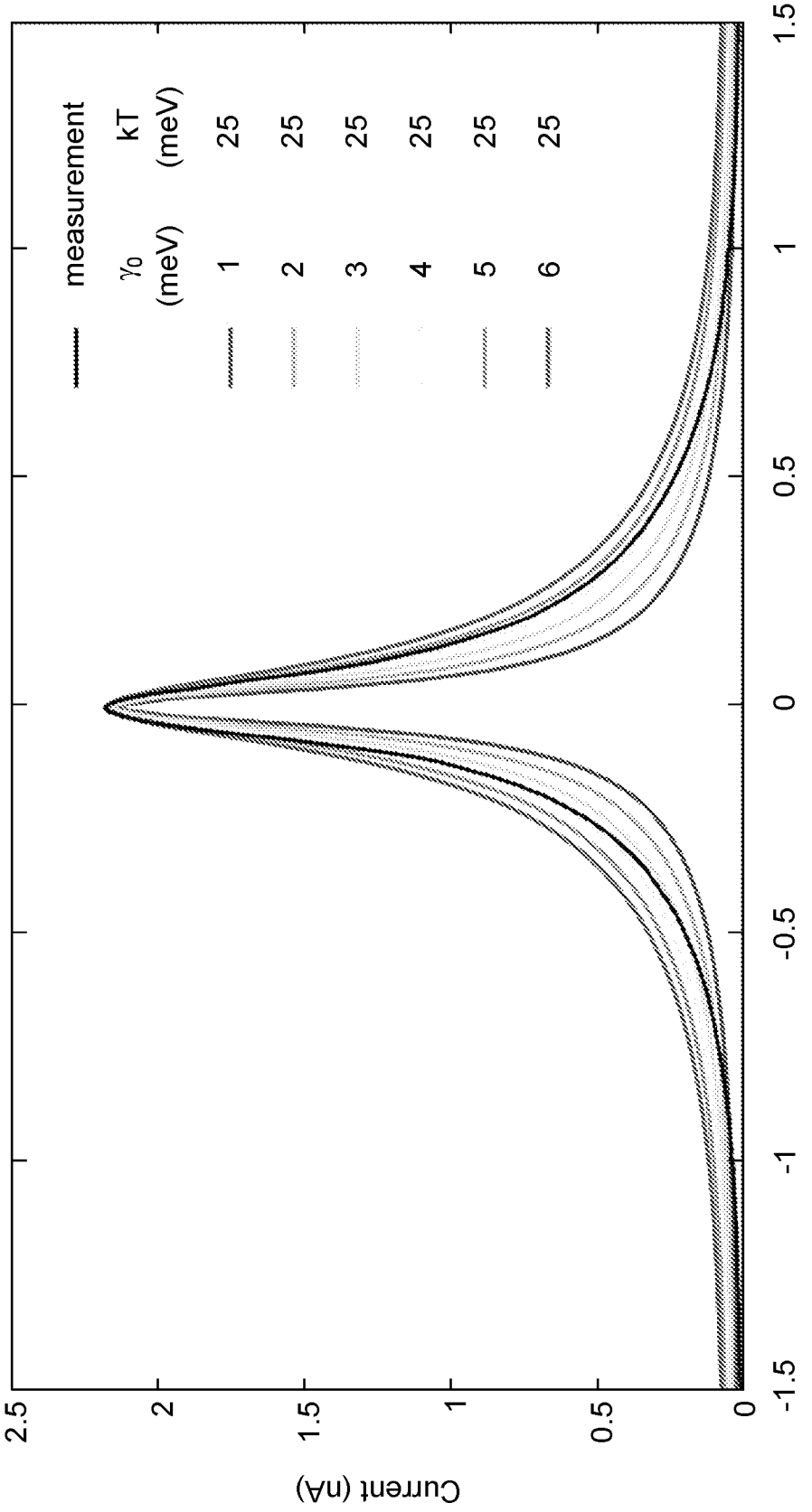
measurement
γ0 (meV)
kT (meV)
1 25
2 25
3 25
4 25
5 25
6 25
Current (nA)
2.5
2
1.5
1
0.5
0
-1.5
-1
-0.5
0
0.5
1
1.5
Rotation Angle θ°

FIG. 23

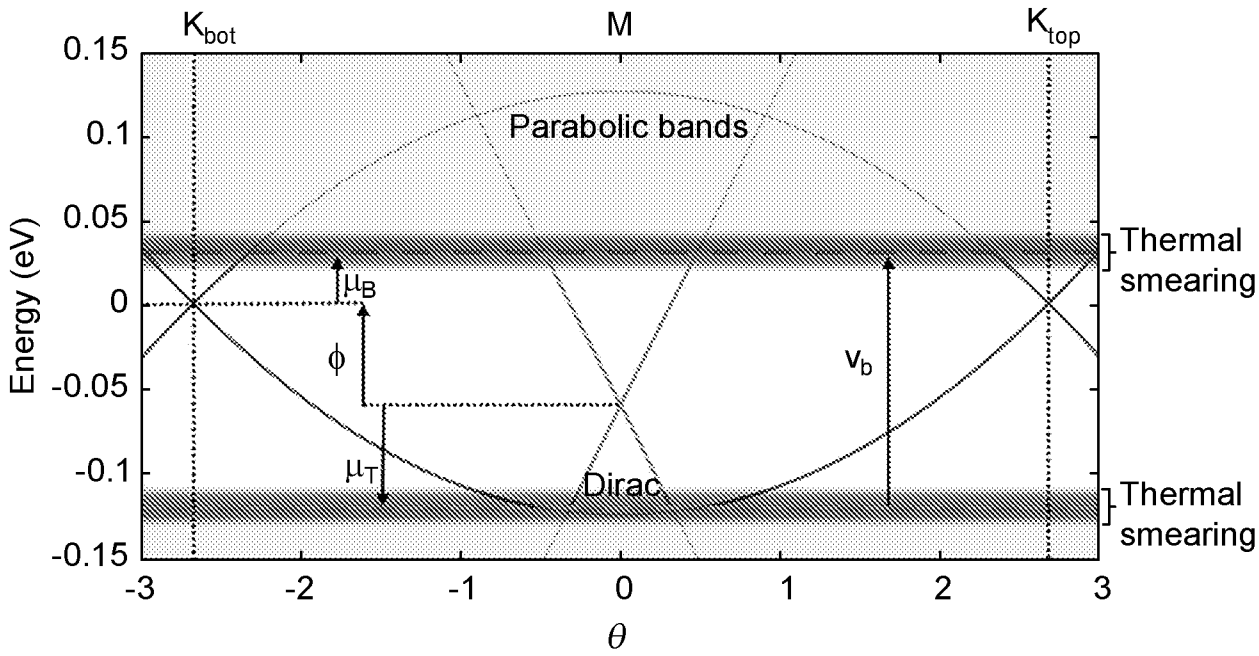

FIG. 24A

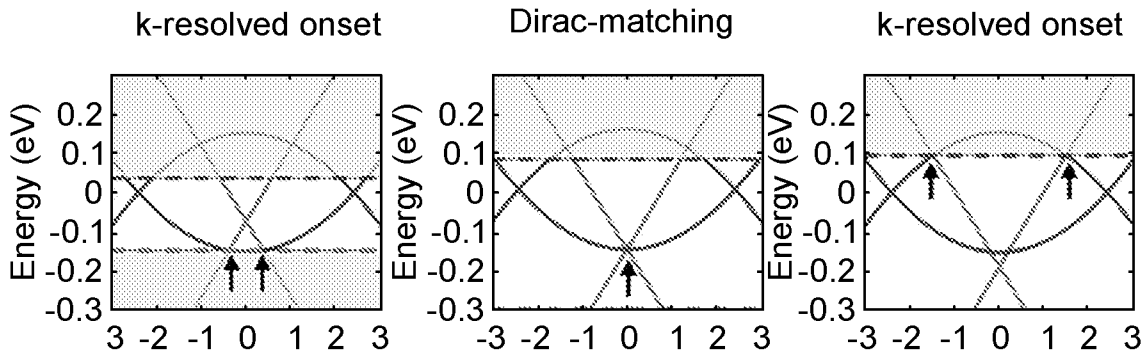

FIG. 24B

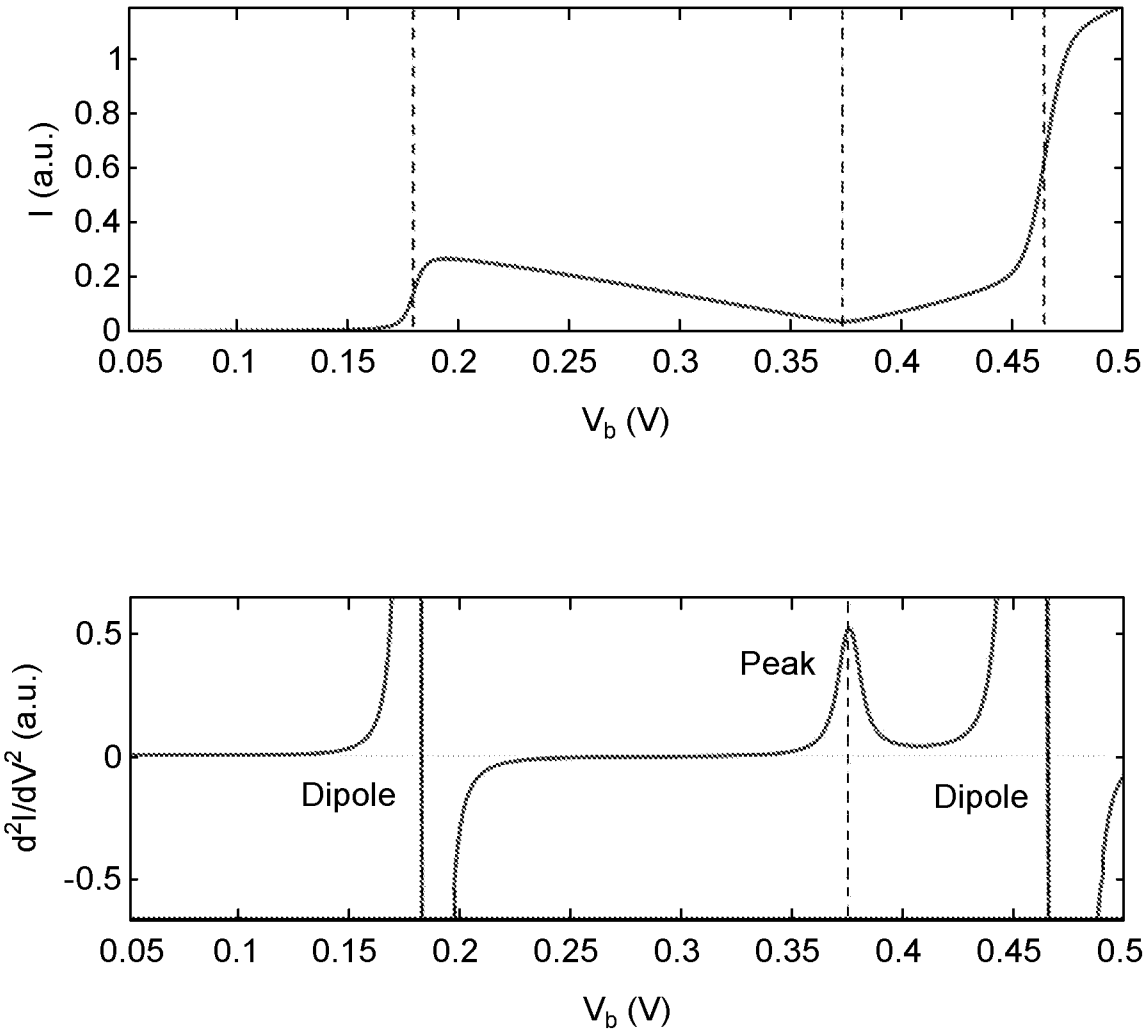
I (a.u.)
1
0.8
0.6
0.4
0.2
0
0.05
0.1
0.15
0.2
0.25
0.3
0.35
0.4
0.45
0.5
V_b (V)
d^2I/dV^2 (a.u.)
0.5
0
-0.5
Peak
Dipole
Dipole
0.05
0.1
0.15
0.2
0.25
0.3
0.35
0.4
0.45
0.5
V_b (V)

FIG. 24C

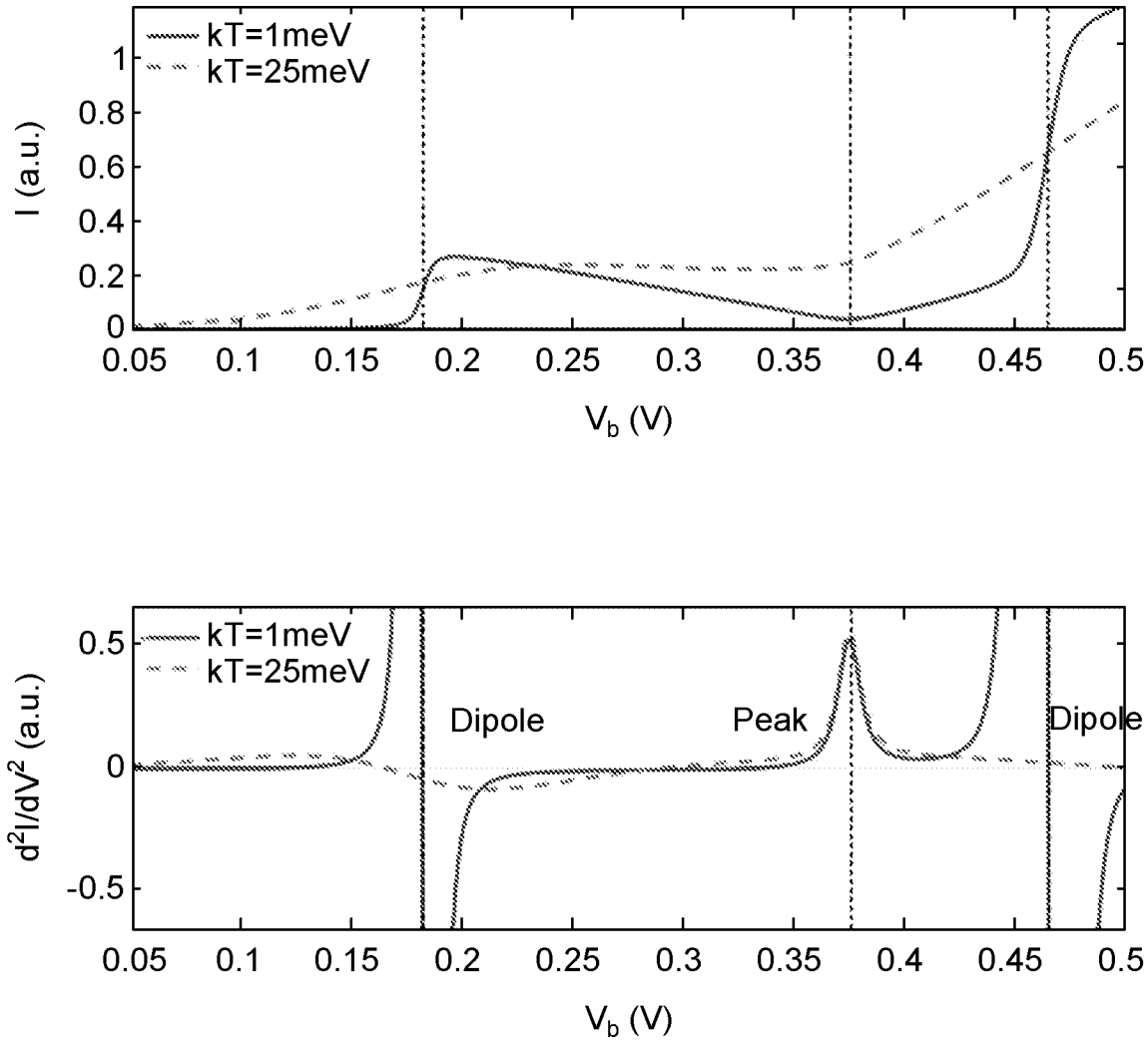
kT=1meV
kT=25meV
I (a.u.)
0
0.2
0.4
0.6
0.8
1
0.05
0.1
0.15
0.2
0.25
0.3
0.35
0.4
0.45
0.5
V_b (V)
kT=1meV
kT=25meV
Dipole
Peak
Dipole
d^2I/dV^2 (a.u.)
0.5
0
-0.5
0.05
0.1
0.15
0.2
0.25
0.3
0.35
0.4
0.45
0.5
V_b (V)

FIG. 25

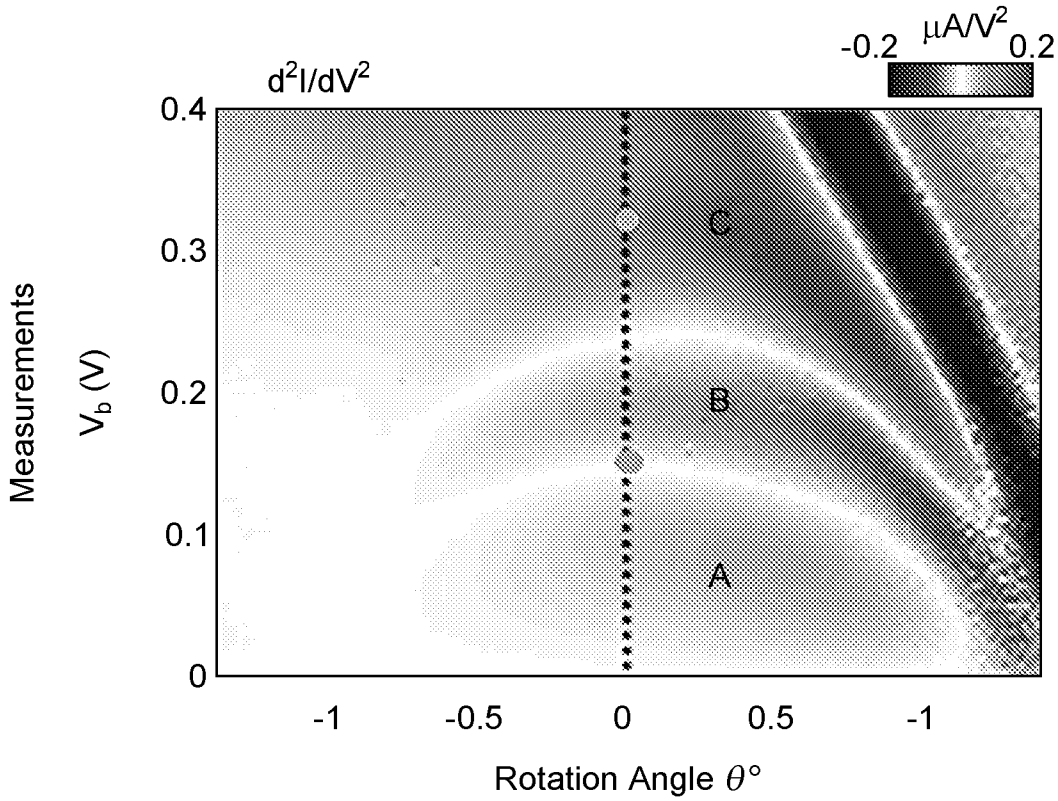

FIG. 26A

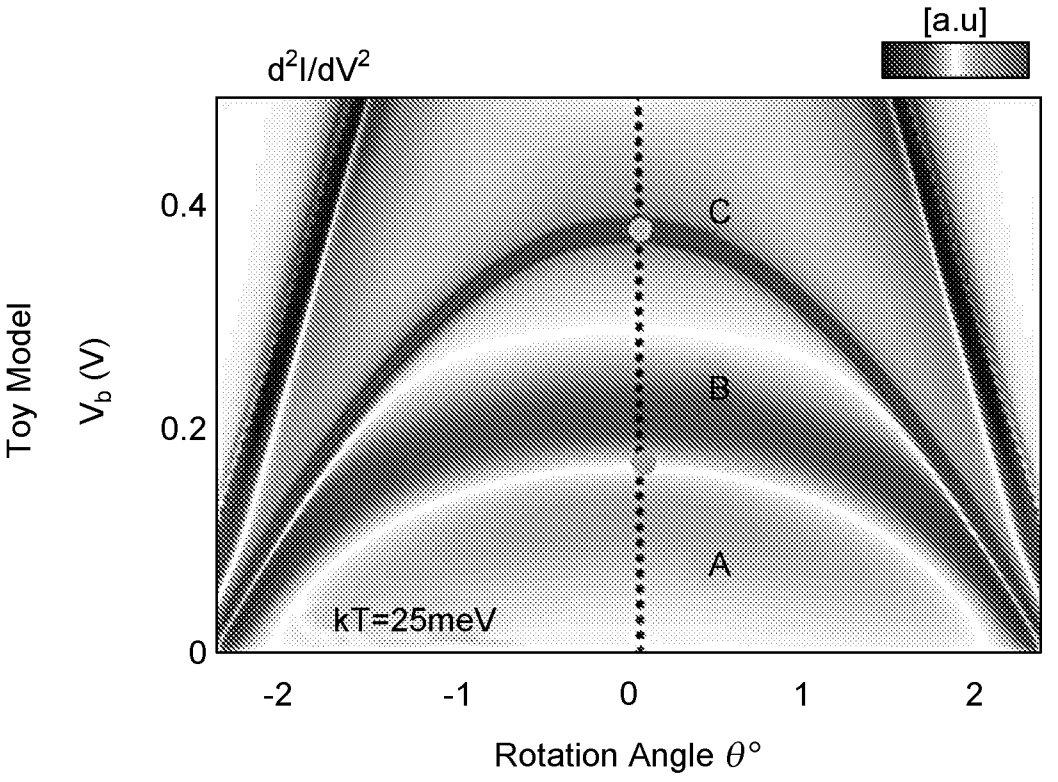

FIG. 26B

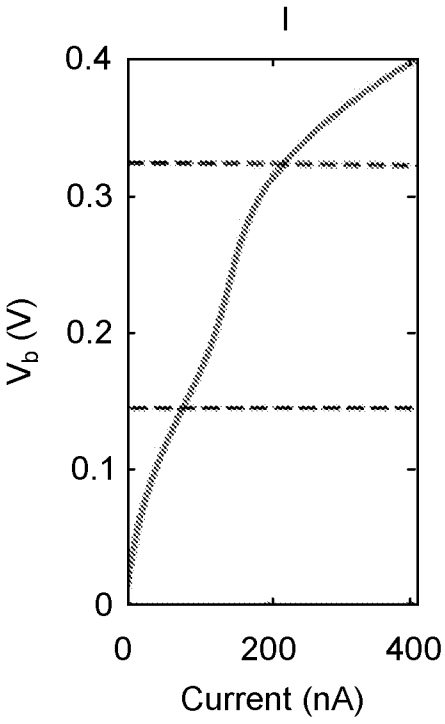

FIG. 26C

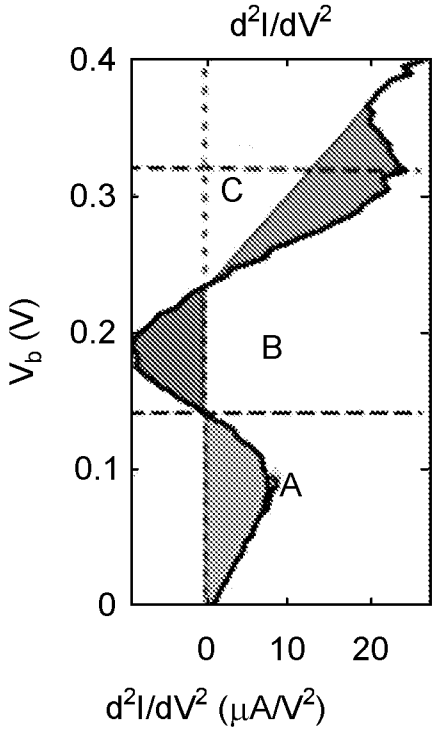

FIG. 26E

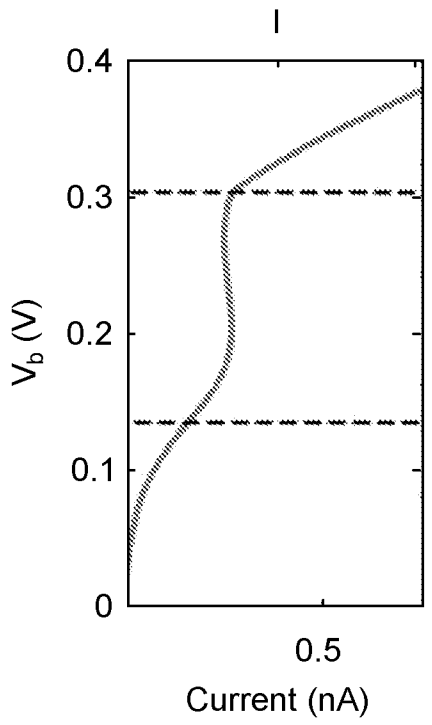

FIG. 26D

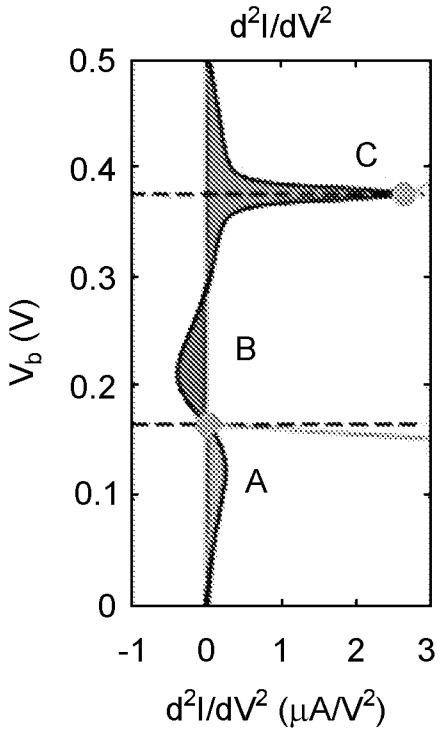

FIG. 26F

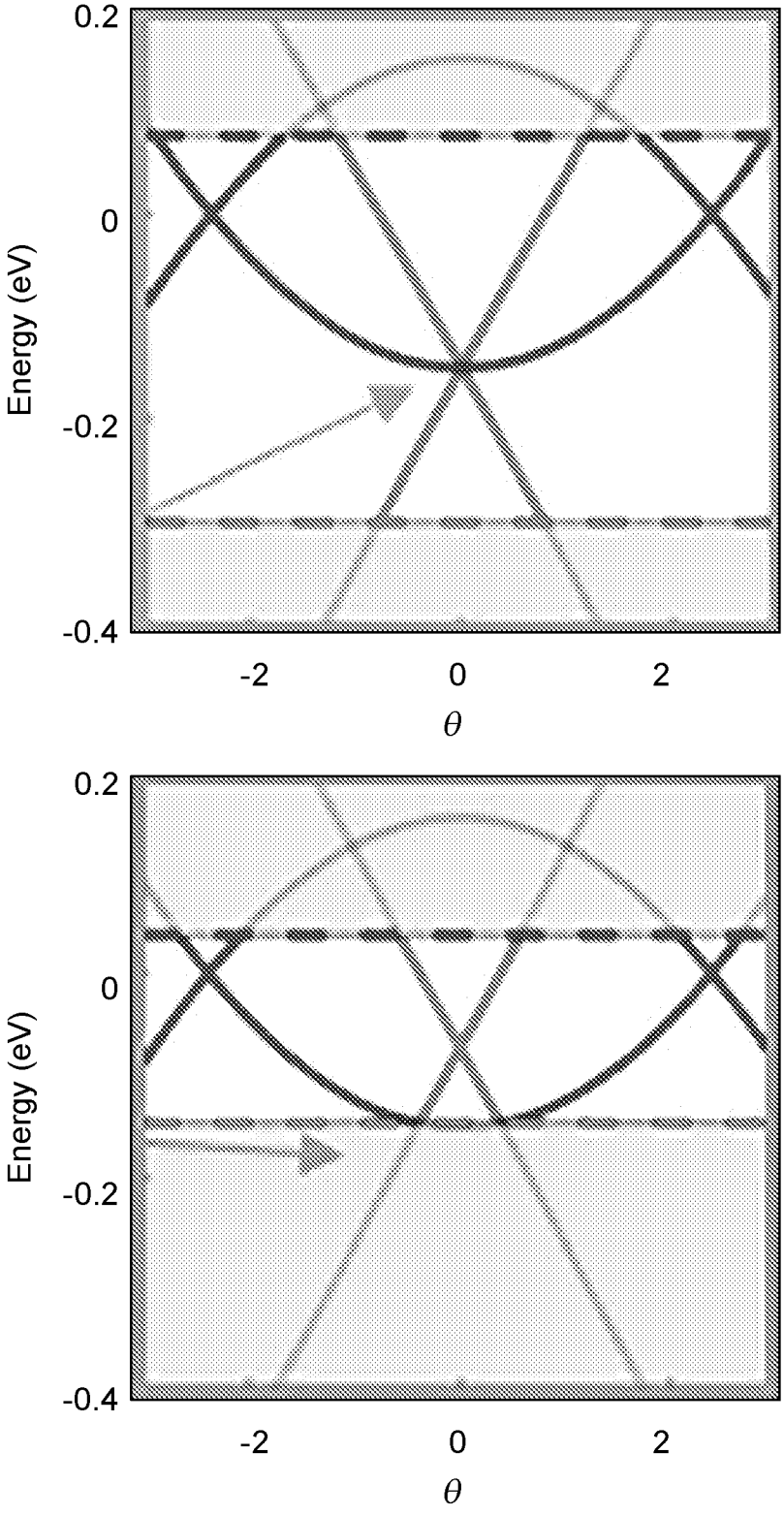

FIG. 26G

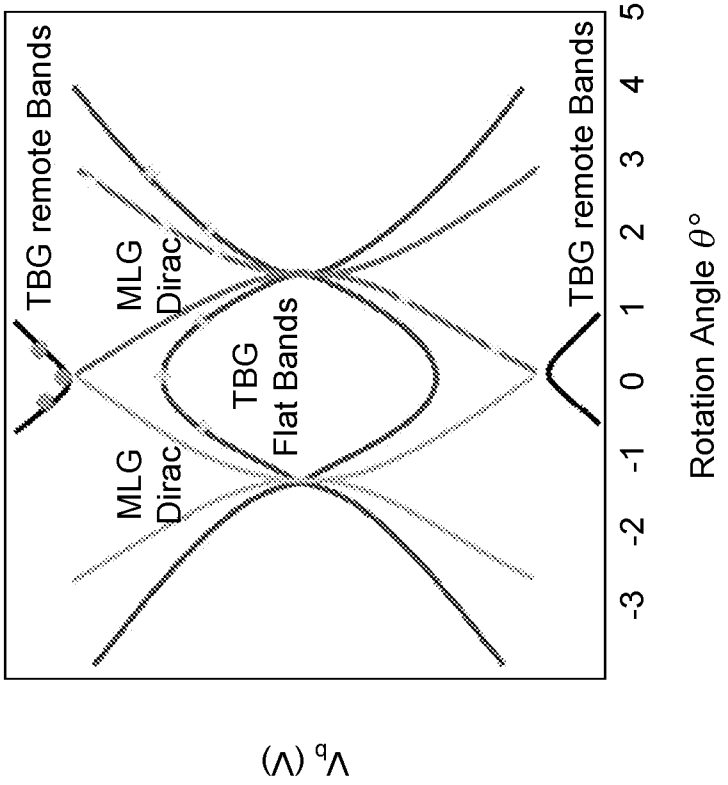

FIG. 27B

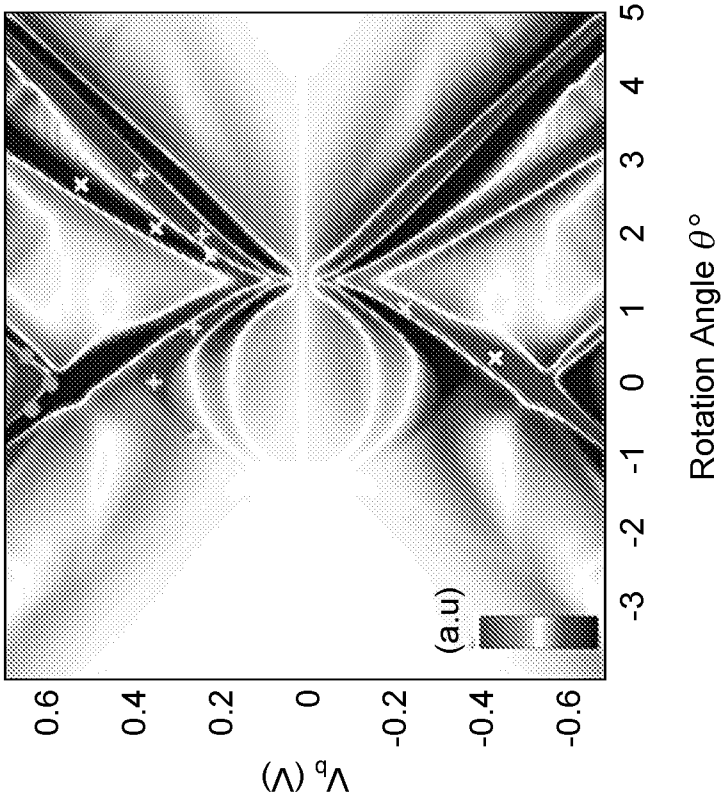

FIG. 27A

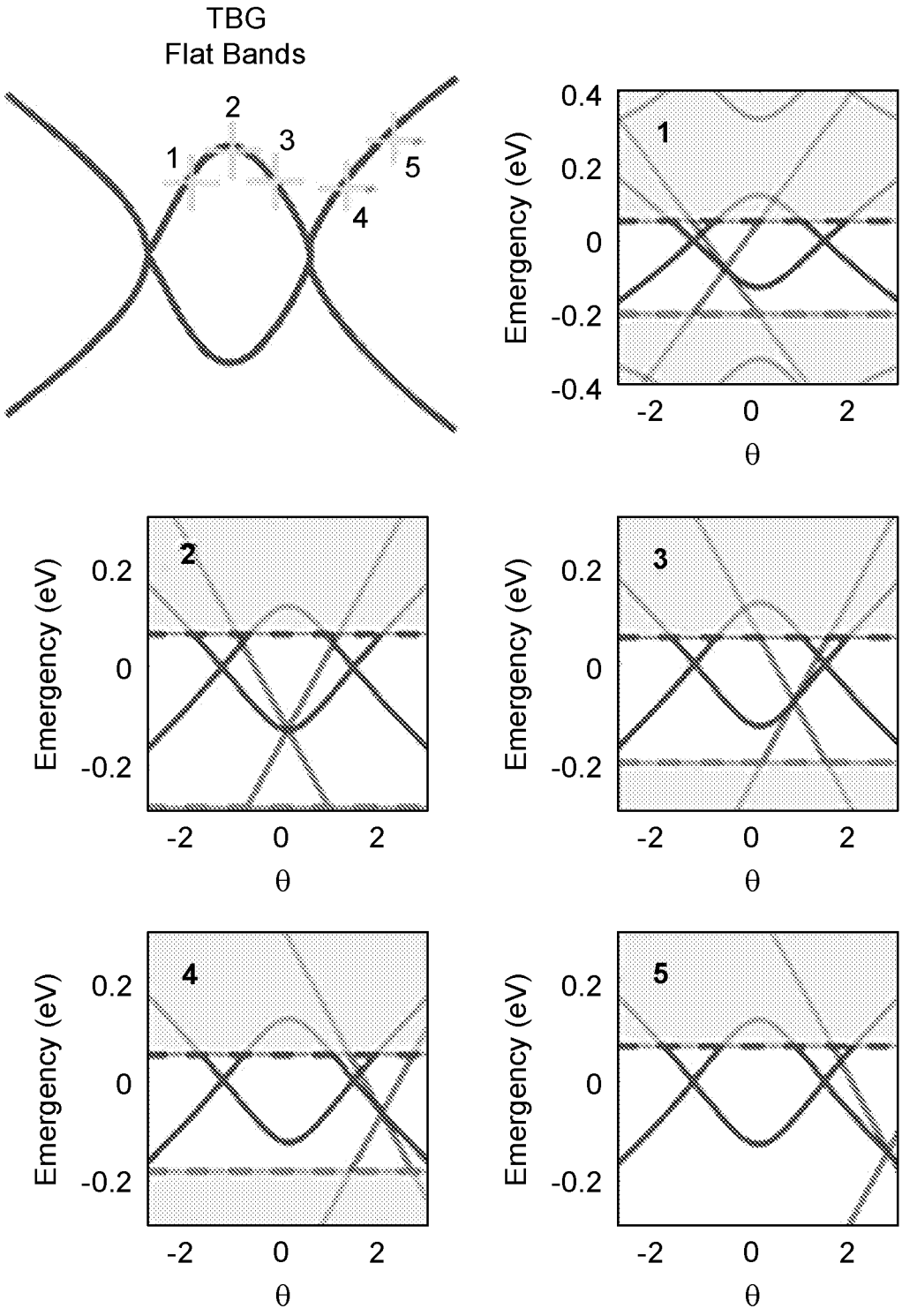

FIG. 27C

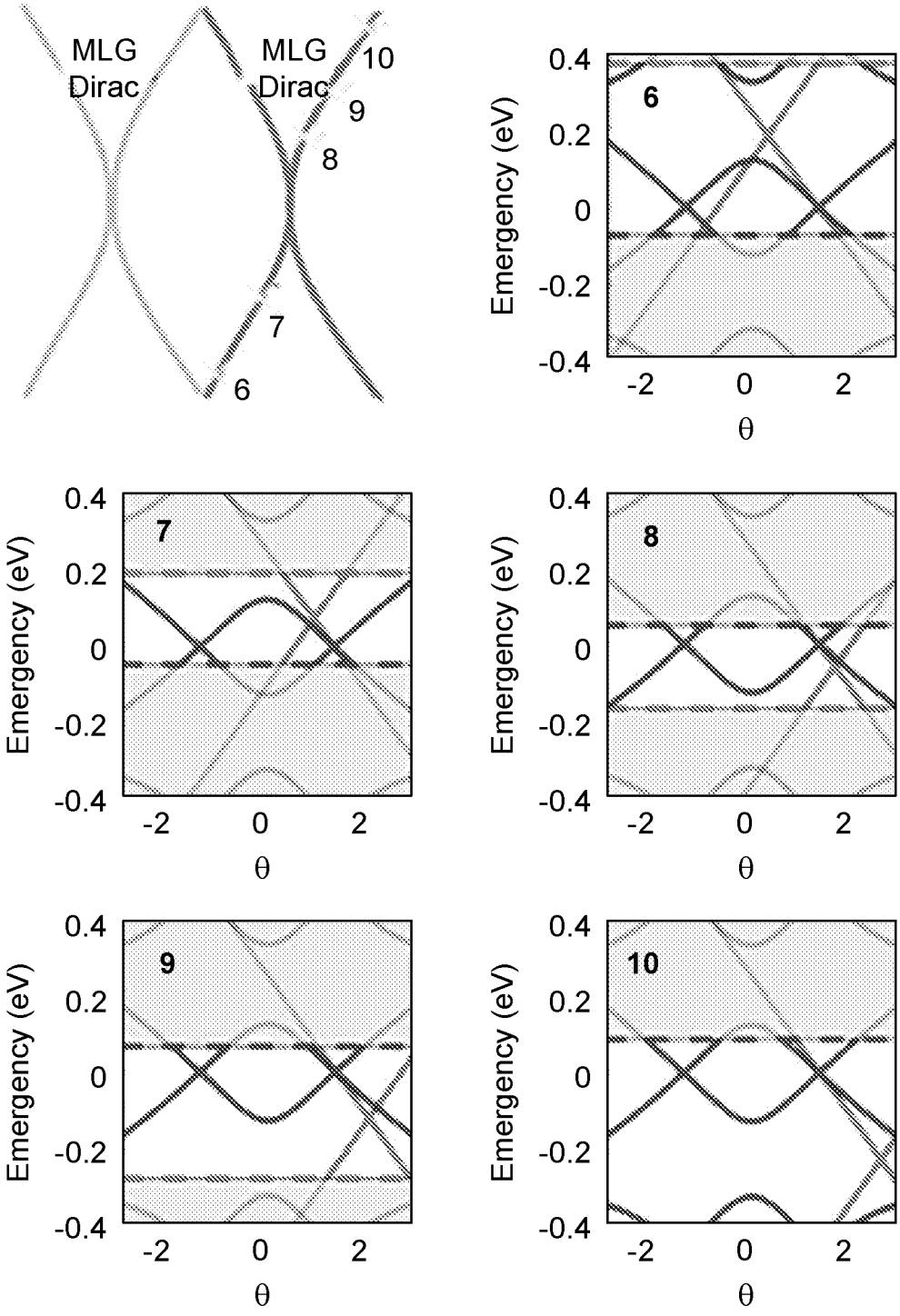
MLG
Dirac
MLG
Dirac
10
9
8
7
6
Emergency (eV)
0.4
0.2
0
-0.2
-0.4
-2
0
2
θ
6
7
8
9
10

FIG. 27D

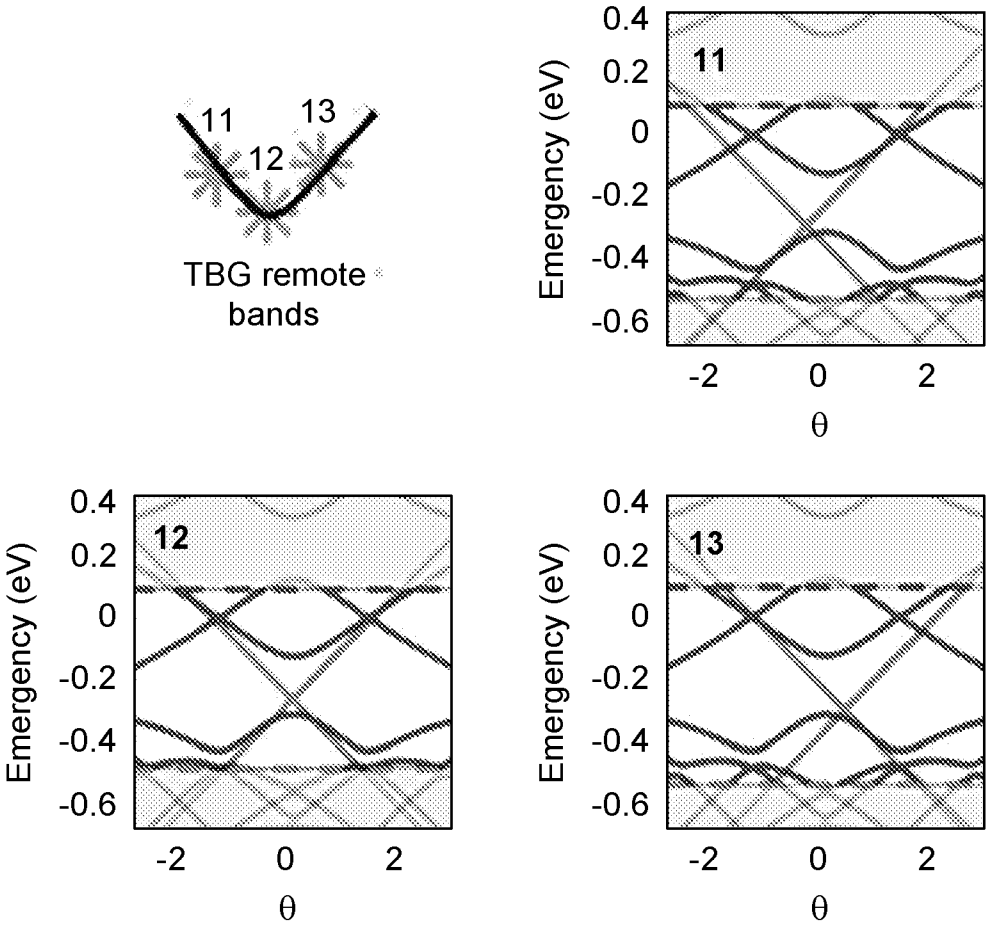
11
12
13
TBG remote bands
Emergency (eV)
0.4
0.2
0
-0.2
-0.4
-0.6
-2
0
2
θ
11
12
13

FIG. 27E

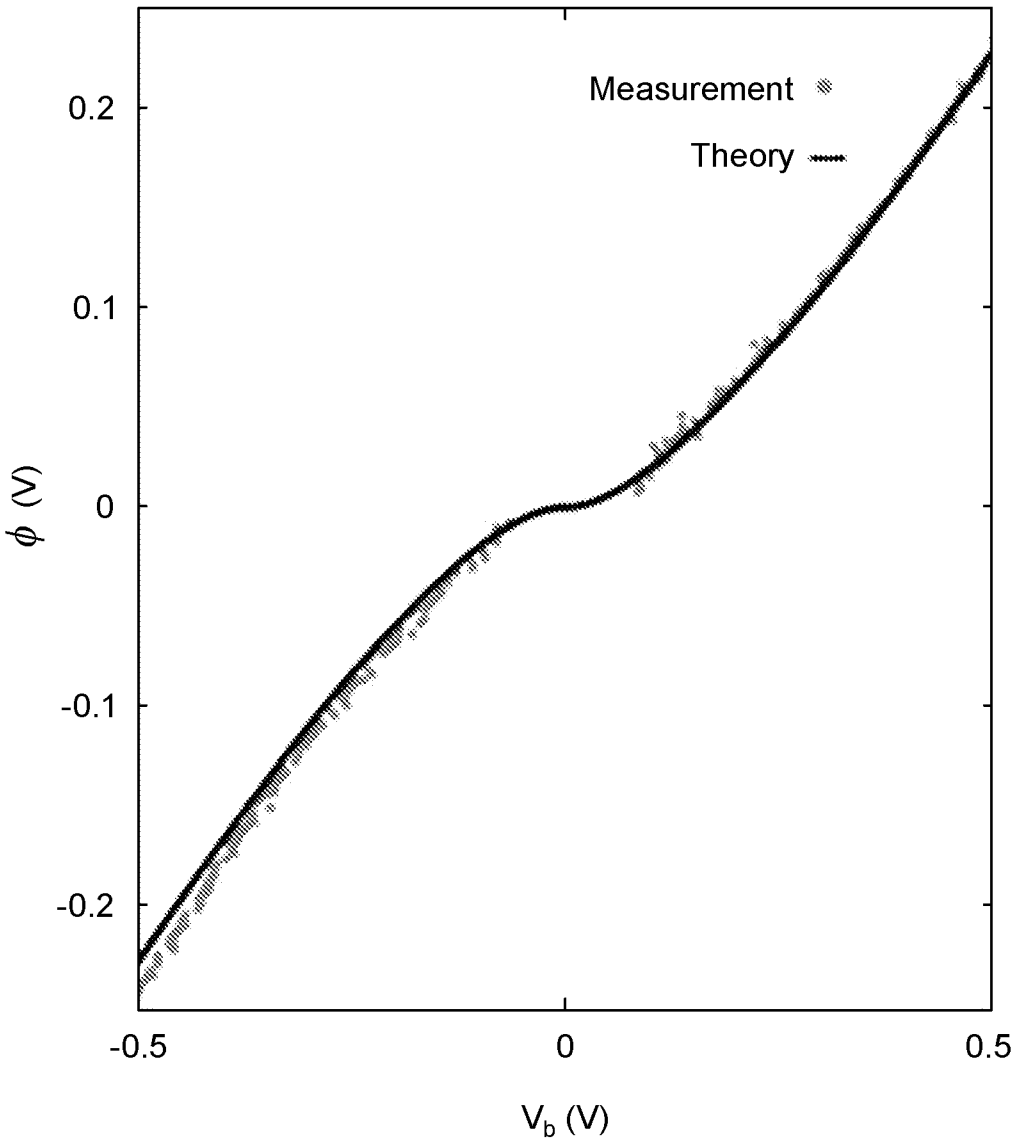

FIG. 28

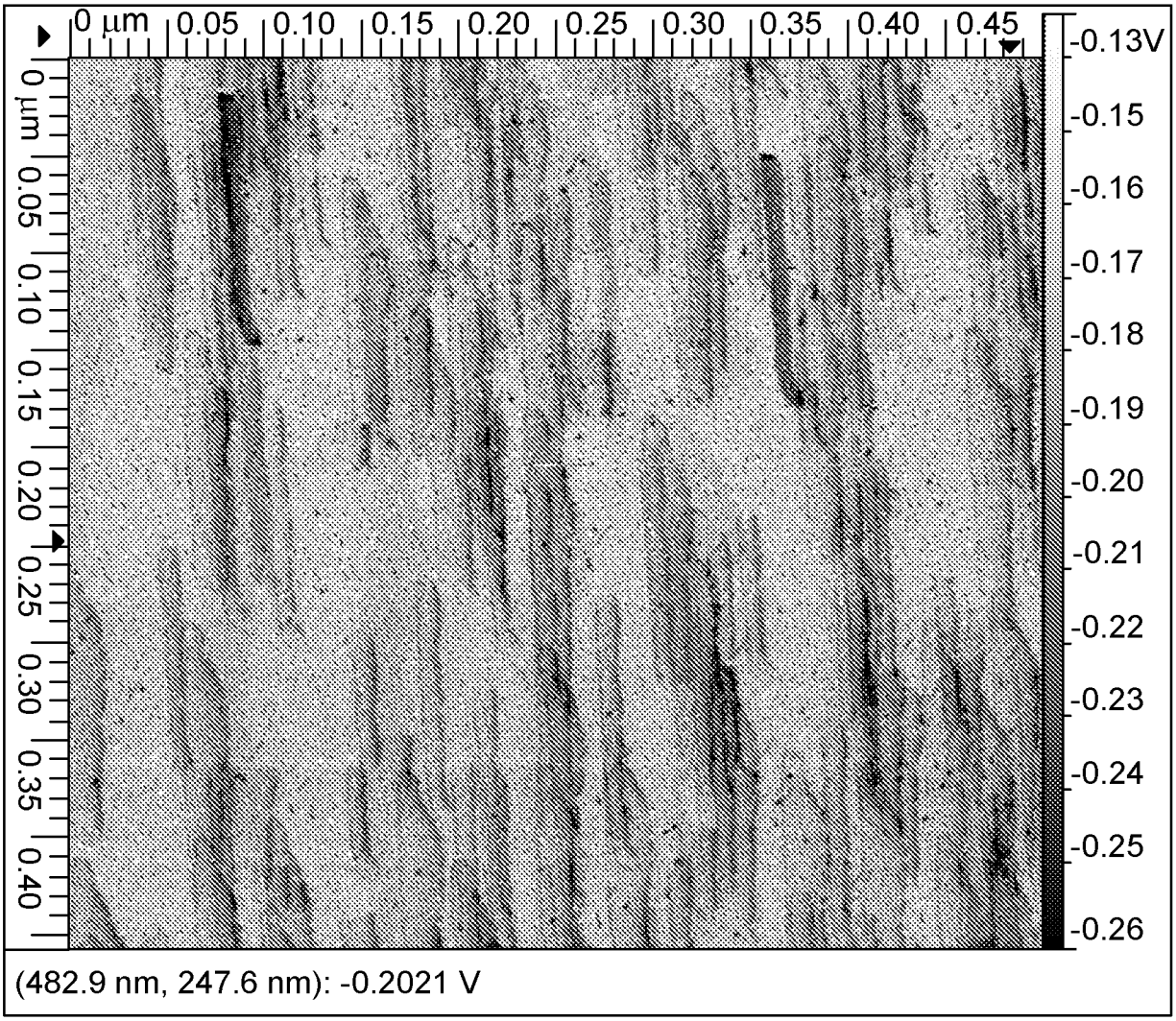
0 µm
0.05
0.10
0.15
0.20
0.25
0.30
0.35
0.40
0.45
-0.13V
-0.15
-0.16
-0.17
-0.18
-0.19
-0.20
-0.21
-0.22
-0.23
-0.24
-0.25
-0.26
(482.9 nm, 247.6 nm): -0.2021 V

FIG. 29

INTERNATIONAL SEARCH REPORT

International application No
PCT/IL2023/050201

A. CLASSIFICATION OF SUBJECT MATTER
INV. G01Q60/16 G01Q60/40 G01Q70/10 G01Q70/14
ADD.

According to International Patent Classification (IPC) or to both national classification and IPC

B. FIELDS SEARCHED

Minimum documentation searched (classification system followed by classification symbols)
G01Q

Documentation searched other than minimum documentation to the extent that such documents are included in the fields searched

Electronic data base consulted during the international search (name of data base and, where practicable, search terms used)
EPO-Internal, WPI Data

C. DOCUMENTS CONSIDERED TO BE RELEVANT

Category*	Citation of document, with indication, where appropriate, of the relevant passages	Relevant to claim No.
X	ALON INBAR ET AL: "The Quantum Twisting Microscope", ARXIV.ORG, CORNELL UNIVERSITY LIBRARY, 201 OLIN LIBRARY CORNELL UNIVERSITY ITHACA, NY 14853, 10 August 2022 (2022-08-10), XP091292301, figures 1,2,4 page 3, paragraph 2 - page 5, paragraph 2 page 9, paragraph 2 - page 10 ----- -/--	1-34

[x] Further documents are listed in the continuation of Box C. [ ] See patent family annex.

* Special categories of cited documents :

"A" document defining the general state of the art which is not considered to be of particular relevance

"E" earlier application or patent but published on or after the international filing date

"L" document which may throw doubts on priority claim(s) or which is cited to establish the publication date of another citation or other special reason (as specified)

"O" document referring to an oral disclosure, use, exhibition or other means

"P" document published prior to the international filing date but later than the priority date claimed

"T" later document published after the international filing date or priority date and not in conflict with the application but cited to understand the principle or theory underlying the invention

"X" document of particular relevance;; the claimed invention cannot be considered novel or cannot be considered to involve an inventive step when the document is taken alone

"Y" document of particular relevance;; the claimed invention cannot be considered to involve an inventive step when the document is combined with one or more other such documents, such combination being obvious to a person skilled in the art

"&" document member of the same patent family

Date of the actual completion of the international search	Date of mailing of the international search report
26 June 2023	10/07/2023

Name and mailing address of the ISA/	Authorized officer
European Patent Office, P.B. 5818 Patentlaan 2 NL - 2280 HV Rijswijk Tel. (+31-70) 340-2040, Fax: (+31-70) 340-3016	Polesello, Paolo

3

Form PCT/ISA/210 (second sheet) (April 2005)

C(Continuation). DOCUMENTS CONSIDERED TO BE RELEVANT

Category*	Citation of document, with indication, where appropriate, of the relevant passages	Relevant to claim No.
L	Anonymous: "Can you explain what is an arXiv publication? ¦ Editage Insights", , 13 February 2017 (2017-02-13), XP055978590, Retrieved from the Internet: URL:https://www.editage.com/insights/can-you-explain-what-is-an-arxiv-publication [retrieved on 2022-11-07] the whole document -----	